The Low-Resolution DRAO Survey of Polarized Emission at 1.4 GHz

Dissertation
zur
Erlangung des Doktorgrades (Dr. rer. nat.)
der
Mathematischen-Naturwissenschaftlichen Fakultät
der
Rheinischen Friedrich-Wilhelms-Universität Bonn

vorgelegt von
Maik Wolleben
aus
Hannover

Bonn, 2005

Angefertigt mit Genehmigung der Mathematisch-Naturwissenschaftlichen Fakultät
der Rheinischen Friedrich-Wilhelms Universität Bonn

1. Referent: Prof. Dr. U. Klein
2. Referent: Prof. Dr. R. Wielebinksi

Tag der Promotion:

Zusammenfassung

Der „Low-Resolution DRAO Survey of Polarized Emission" ist eine neue Polarisationsdurchmusterung des Nordsternhimmels bei einer Frequenz von 1.4 GHz. Die Beobachtungen wurden mit dem „26-m Teleskop" des Dominion Radio Astrophysical Observatory (DRAO) durchgeführt, eine Einzelantenne mit einem Durchmesser von 25.6 m und einer Winkelauflösung von 36′ bei dieser Frequenz. Um absolut geeichte Stokes U und Q Karten räumlich ausgedehnter Emissionsstrukturen zu erhalten, wurden die Daten, mit Hilfe der Leiden/Dwingeloo Polarisationsdurchmusterung, bereinigt von Bodenstrahlung. Mittels Driftscans wurde der Himmel im Bereich zwischen −27° und +90° Deklination beobachtet. Voll gesampelte Driftscans wurden in Schritten von 1° bis 5° in Deklination gemessen und ergeben eine Abdeckung des nördlichen Himmels von 21.7%.

Diese Doktorarbeit handelt von der Durchführung und Analyse der neuen DRAO-Polarisations-Durchmusterung. Eine kurze historische Einführung, sowie eine wissenschaftliche Begründung für die neue Durchmusterung wird gegeben. Darauf folgt eine detaillierte Beschreibung des Empfängers und der Entwicklung von Software, welche für die Durchführung der Beobachtungen notwendig war. Desweiteren werden Fehlerquellen, sowie die absolute Eichung der Daten diskutiert. Die Ergebnisse einer ersten Analyse werden präsentiert.

Diese Durchmusterung erweitert die Datenbank absolut geeichter Polarisationsbeobachtungen des Nordsternhimmels. Diese Daten sind unerlässlich für die Eichung von hochaufgelösten Polarisationsbeobachtungen der galaktischen Ebene, welche mit Synthese, sowie großen Einzelteleskopen durchgeführt werden, weil sie darin fehlende Informationen über ausgedehnte Strukturen liefern. Die Analyse faszinierender neuer Objekte, entdeckt in Polarisationsbeobachtungen der galaktischen Ebene, erfordert eine Absoluteichung der Daten. Die neue Durchmusterung des DRAO liefert Karten ausgedehnter Strukturen in Auflösung und Empfindlichkeit, welche den Anforderungen der hochaufgelösten Durchmusterungen enspricht.

Eine vorläufige Analyse der neuen DRAO-Durchmusterung enthüllt bisher unbekannte Komponenten polarisierter Emission, wie zum Beispiel depolarisierte Gebiete in Richtung von H ɪɪ-Regionen, anhand dessen die Entfernung zur „Fan"-Region, ein ausgedehntes und polarisiertes Gebiet, abgeleitet werden kann. Desweiteren wird eine Region mit niedriger Prozentpolarisation in Richtung des ersten galaktischen Quadranten analysiert, sowie „High-Latitude Polarized Emission" gefunden, welche als Synchrotronemission einer magnetischen Schale interpretiert wird. Die Verbesserung des Samplings im Vergleich zu früheren Polarisationsdurchmusterungen des nördlichen Himmels erlaubt detaillierte morphologische Studien der lokalen galaktischen Umgebung.

Abstract

The "Low-Resolution DRAO Survey of Polarized Emission" is a new polarization survey of the northern sky at a frequency of 1.4 GHz. The observations were carried out using the "26-m Radio Telescope" of the Dominion Radio Astrophysical Observatory (DRAO), a single-antenna with a diameter of 25.6 m and 36′ angular resolution at that frequency. The data are corrected for ground radiation, by tightening to the Leiden/Dwingeloo polarization survey, to obtain absolutely calibrated Stokes U and Q maps containing emission structures of large spatial extend. Survey observations were carried out by drift scanning the sky between $-27°$ and $+90°$ declination. The fully sampled drift scans, observed in steps of $1°$ to $5°$ in declination, result in a northern sky coverage of 21.7%.

This thesis deals with the realization and analysis of the new DRAO polarization survey. A brief historical introduction along with a scientific justification for the new survey is given. This is followed by a detailed description of receiver and software development necessary for carrying out the survey, as well as a discussion of error sources and absolute calibration of the data. The first results of an initial data analysis are presented.

This survey largely extends the data base of absolutely calibrated polarization observations of the northern sky. Those data bases are essential for the calibration of high-resolution polarization observations made with synthesis and large single-antenna telescopes covering the Galactic plane, because they provide missing information on large-scale structures. The analysis of intriguing new features revealed by the recent polarization observations of the Galactic plane requires an absolute calibration of polarization data. The new DRAO survey provides maps of large-scale emission with sampling and sensitivity suited for their calibration.

A preliminary analysis of the new survey reveals previously unknown components of polarized emission such as depolarized patches towards H II-regions that reveal distances to the "fan"-region. Furthermore, a patch of low percentage polarization towards the first quadrant of the Galaxy is analyzed. "High-Latitude Polarized Emission" is found and interpreted as synchrotron emission from a magnetic shell. The improvement in sampling compared to previous large-scale polarization surveys of the northern sky allows morphological studies of the local Galactic environment in great detail.

Contents

Foreword

The polarization of Galactic synchrotron emission is being measured since more than 40 years at frequencies from 100 MHz to 1 GHz and higher, involving different kinds of receivers and telescopes. With the availability of high-resolution polarization data obtained during the last decade, numerous new objects and features that can only be seen in polarization are detected. A new generation of polarization surveys made with large single-antenna and synthesis telescopes clearly opens a new window for the investigation of the magneto-ionic medium of our Galaxy.

For the study of diffuse Galactic emission the absolute calibration of polarimetric data by incorporation of large-scale emission (zero-spacings) is of vital importance. Zero-spacings are missing in observations made with synthesis and large single-antenna telescopes, because of insensitivity of interferometers to large-scale emission or confusion with ground and stray radiation in case of single-antenna telescopes. Hence, a new absolutely calibrated survey with sufficient high sensitivity is required to allow correction of actual high-resolution data. The realization and analysis of such a survey is described in the present thesis.

Starting with my first year for a doctorate at the Dominion Radio Astrophysical Observatory (DRAO) in Penticton, Canada, I found myself facing a 26-m telescope that had never been used for polarimetric observations before; with a receiver that was not intended for observations of linear polarization. Moreover, the backend device, a continuum polarimeter shipped from the Max-Planck Institut für Radioastronomie in Bonn (MPIfR), was waiting to be "plugged in". Since no experience using this telescope for polarization observations existed, this PhD project gave me the opportunity to gain insight into many different aspects of performing a polarization survey such as technical, observational, and calibration issues.

One year (May 2002 - May 2003) was dedicated for polarimetric work at the DRAO 26-m Telescope, including survey observations. Almost the first half of this year I spent making the "26-m" capable of measuring linear polarization. Prior to observing, two things had to be developed at the same time. The receiver required modifications to allow measurements of *linear* polarization and software needed to be written to control the backend devices, data acquisition, and recording. After making sure that hard- and software worked well, an observing scheme was developed and survey observations could start.

Back at the MPIfR, a data processing and reduction chain had to be set up to handle and calibrate the enormous amount of data collected during 7 months of observing. The results are absolutely calibrated Stokes U and Q maps of the northern sky. Although not fully sampled, these maps consist of 100 times more data points than provided by the Leiden/Dwingeloo polarization survey (observed between 1961 and 1966), while covering a larger area of the sky.

It was soon obvious that the new survey not only provides information about low spatial frequencies for the calibration of high-resolution data, but also yields new aspects of the polarized sky. Therefore, an analysis of the new data is presented and first results are discussed.

In the first part (Chapters 1 and 2) of this thesis, the scientific justification for the new polarization survey is discussed, and the meaning and importance of "absolute calibration" for studies of polarized emission are specified. Some historical aspects are also given. Furthermore, the reader is introduced to the basic formalism of wave polarization that is used in this thesis.

The second part (Chapters 3, 4, and 5) deals with all aspects of undertaking the survey observations, starting with a description of the receiver and necessary modifications, software that needed to be written, error sources, and the data processing and calibration. Survey observations were done by

drift scanning. Additional measurements were made for calibration purposes and the determination of ground radiation profiles. The path of the data from the receiver to the final polarization maps will be described.

In the third part (Chapters 6 and 7) a study of the new polarization data is presented. This starts with a description of the large-scale distribution of polarized emission. Known Galactic objects are identified as well as new features outlined. Polarized emission at high Galactic latitudes is interpreted as synchrotron emission from a magnetic shell. Depolarization of diffuse polarized emission, caused by H II-regions, is used to derive lower limits on the distance to the "fan"-region, a spatially extended, intense patch of highly polarized emission.

Finally, a conclusion and outlook are given in the last part (Chapter 8). The survey presented in this thesis has a sky coverage of 21.7% of the surveyed region. Meanwhile (by March 2005), a coverage of more than 43% has been achieved in the course of ongoing survey observations. These data will be made available via web interface as explained in the last Chapter.

List of acronyms frequently used:

Low-Resolution DRAO Survey of Polarized Emission	26-m Survey
Canadian Galactic Plane Survey	CGPS
Effelsberg Medium Latitude Survey	EMLS
High Latitude Polarized Emission	HLPE
Leiden-Dwingeloo Survey of Polarized Emission at 1.4 GHz	LDS

1 Polarization Surveys

This chapter gives a brief review of polarization surveys, a discussion of absolute calibration in polarimetry, and the justification for the new polarization survey. The first polarization surveys provided polarized brightness temperatures for large areas of the sky. But the data are only sparsely sampled, resulting in low angular resolution. In recent years, a new generation of polarization surveys covering the Galactic plane has been initiated and will provide fully sampled maps of high angular resolution. High-resolution surveys, however, lack large-scale structures (zero-spacings) necessary for an absolute calibration. This information must come from low-resolution surveys such as the new DRAO polarization survey presented in this thesis.

1.1 History of Polarization Surveys

In 1933, the first detection of radio emission of extraterrestrial origin was published by Karl Jansky (Jansky, 1933), but was not recognized by the astronomical community. A few years later, in 1940, Grote Reber (Reber, 1944) mapped the sky at 160 MHz. Various other surveys of total power emission at frequencies between $\sim$ 100 MHz and $\sim$ 400 MHz followed this work. Although the theory predicts this radio emission – later called non-thermal emission – to be linearly polarized, it was not before 1962 when two groups (Westerhout et al., 1962; Wielebinski et al., 1962) published the first definitive detection of the linear polarization of Galactic radio waves. Figure 1.1 shows one of the first polarimetric observations of the North-Polar Spur.

The non-thermal component of the radio emission of the Milky Way had been understood as synchrotron radiation from relativistic cosmic ray electrons interacting with the Galactic magnetic field (Kiepenheuer, 1950). Synchrotron radiation from an ensemble of relativistic electrons is linearly polarized (e.g. Westfold, 1959; Pacholczyk, 1970). The degree of linear polarization depends on the energy spectral index β of the relativistic electrons and is 72% for $\beta = -2.7$ (see Section 2.7). Much of
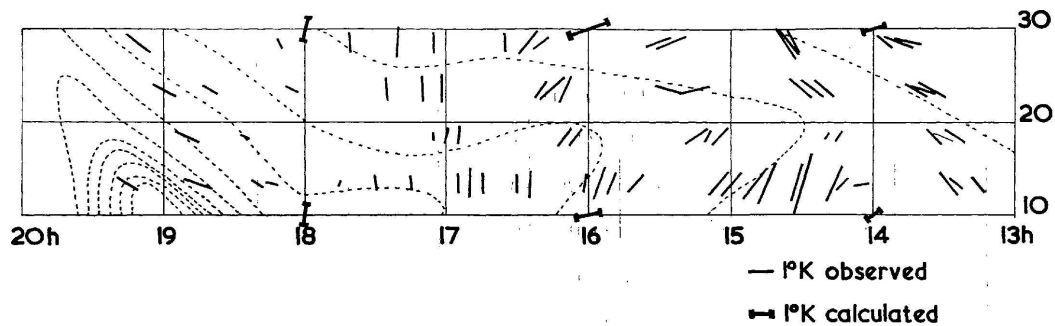

Figure 1.1: The Galactic polarization was discovered to be polarized. This map shows E-vectors of the first polarimetric measurements of the highly polarized North Polar Spur, made by Wielebinski et al. (Westerhout et al., 1962).
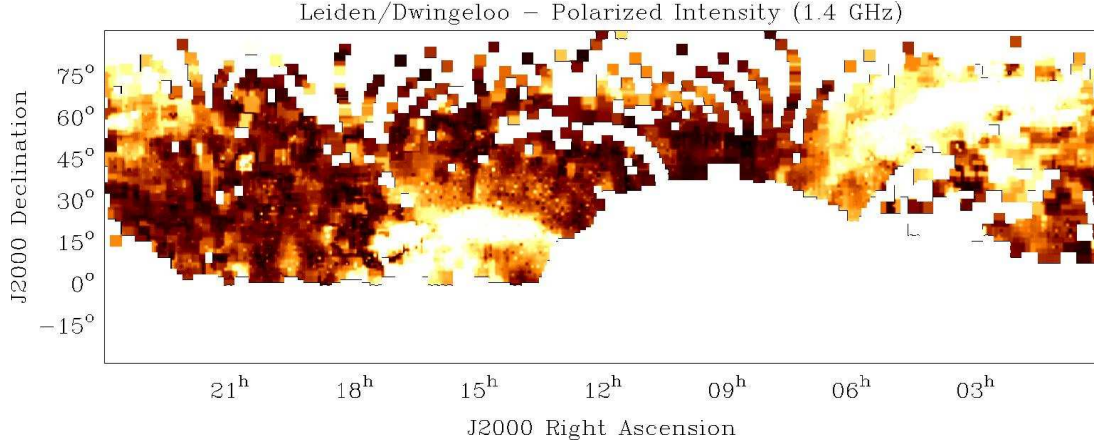
1

Figure 1.2: Map of polarized intensities showing data taken from the LDS at 1.4 GHz (Brouw & Spoelstra, 1976). The map boundaries correspond to the part of the sky observable from Penticton.

the relevant theory had been developed earlier and was known as "Magneto-Bremsstrahlung" (Schott, 1907).

At low frequencies, ionospheric Faraday rotation was found to significantly affect the data (Wielebinski et al., 1962). Hence, the frequency range of polarimetric observations was extended to higher frequencies, allowing the measurement of Galactic Faraday rotation. Large-scale surveys of linear polarization were made at 408 MHz by (Berkhuijsen & Brouw, 1963; Wielebinski & Shakeshaft, 1964; Muller et al., 1963; Mathewson et al., 1965). Polarization surveys at 610 MHz (Berkhuijsen et al., 1964; Brouw & Spoelstra, 1976; Mathewson et al., 1966) and 1407 MHz (Bingham, 1966) provide information about the large-scale distribution of linearly polarized Galactic radio emission. Additional surveys at 465 MHz, 820 MHz, and 1411 MHz were undertaken (Brouw & Spoelstra, 1976) and provide rotation measures for large areas of the northern sky, published by Spoelstra (1984).

The detection of polarization was the final proof that diffuse radio emission at these frequencies is produced mainly by the synchrotron process. As a consequence, the Galaxy must possess a general magnetic field. Especially at Galactic longitudes around 140° a good correlation of optical and radio polarization vectors was found. This provided strong arguments for the Davis-Greenstein mechanism, which, in turn, predicts optical polarization to be caused by dust grains aligned by a magnetic field. Therefore, the early polarization surveys were a starting point to understand the magnetic field of the Galaxy.

By a quantitative comparison of polarization of starlight and polarization of Galactic radio emission, Spoelstra (1984) concluded that the polarized emission detected in the Leiden-Dwingeloo surveys originates from distances within about 450 pc. Consequently, polarization surveys at this resolution show only locally emitted radiation. The concept of the "polarization horizon", an approach to model this distance, was later suggested by several authors (Duncan et al., 1997; Gaensler et al., 2001; Landecker et al., 2002).

So far, only the Leiden-Dwingeloo polarization survey has provided absolutely calibrated data for large areas of the northern sky at 1.4 GHz (Brouw & Spoelstra, 1976). But these data are only sparsely sampled (see Figure 1.2). As a consequence, many processing steps, e.g. convolution or smoothing, cannot be adequately applied to these data. Moreover, these observations contain errors and system noise that is large compared with present-day surveys. This limits their compatibility.

A short historical note: Different definitions of polarized brightness temperature were in use during

the first decades of radio polarimetry. A unified scheme based on Stokes parameters was proposed by Berkhuijsen (1975). To convert brightness temperatures stated in the various early surveys to the unified system, conversion factors ranging from 0.5 to 1.3 needed to be applied. Berkhuijsen noted that it is often difficult to determine these factors after so many years, because of the lack of observational details published.

Systematic polarization observations experienced a renaissance during the past several years. With the development of new receivers, surveys of the Galactic plane at higher radio frequencies (e.g.: Junkes et al., 1986, at 2.7 GHz; Duncan et al., 1997, at 2.3 GHz) were made and revealed surprising structures in polarization. Low-frequency polarimetric mapping with synthesis telescopes (e.g. Wieringa et al., 1993, at 350 MHz) confirms the presence of numerous structures and objects detectable only in polarization.

For the study of these objects and the magneto-ionic properties of the interstellar medium, polarization surveys with high sensitivity and resolution mainly covering the Galactic plane are currently being carried out. Observations for the Effelsberg Medium Latitude Survey ($|b| \leq 20°$, Uyanıker et al, 1998, 1999, Reich at al., 2004) at 1.4 GHz have just been finished. The International Galactic Plane Survey (IGPS, $|b| \lesssim 5°$), a major undertaking of mapping the Galactic plane with different telescopes at various wavelengths, provides polarization data at 1.4 GHz obtained with the DRAO synthesis telescope. In the southern hemisphere the Australia Telescope Compact Array is mapping the Galactic plane (SGPS, $|b| \leq 1°$, Dickey et al., 1999) also at 1.4 GHz.

Compared with the early polarization observations, sensitivity and resolution of the new surveys has improved due to utilization of large single-antenna and synthesis telescopes equipped with cooled receivers. But large-scale emission is missing in observations made with these telescopes, because of either insensitivity of interferometers to low spatial frequencies or the baseline setting procedure[1] in single-antenna mapping. Whenever required for the analysis, such data must be augmented with absolutely calibrated data to account for the missing flux and structures. These absolutely calibrated data can have low angular resolution because they only add spatially *extended* emission.

1.2 Absolute Calibration

Measuring absolute intensities of radio signals is difficult, because the radio signal from the source in the sky is received through the antenna and the receiving system which contribute noise and amplify it. Unless the antenna is of simple design so that its gain can be calculated to good precision, the exact gain of the system is unknown. Such simple antennas are horns, and total power observations are being calibrated by adjusting their flux density or temperature scale to the absolute intensities derived by measurements with horn antennas (e.g. Howell & Shakeshaft, 1966).

The polarized-brightness-temperature scales of the early polarization surveys are calibrated against a number of "standard" calibration points. The polarization degree and angle of these standard points were measured with receivers for which the gain in total power was known. In Figure 1.3 the polarized intensities of two such calibration points frequently used for the early surveys are plotted. It can be seen that, with different telescopes, different temperatures were obtained, partly because different definitions of polarized brightness temperature were used.

The receiving system introduces noise and noise is also received through the side lobes of the telescope. This noise is of the same kind as the signal from the radio source and can therefore not be distinguished. Whereas receivers are usually temperature controlled and stable enough to produce a

---

[1]Baseline setting means that a linear "baseline" (first order polynomial) is fitted through the start and end of each subscan and is subsequently subtracted. By this, the edges of maps are set to zero, which removes ground and spillover noise but also large-scale emission on scales equal or greater than the map size.
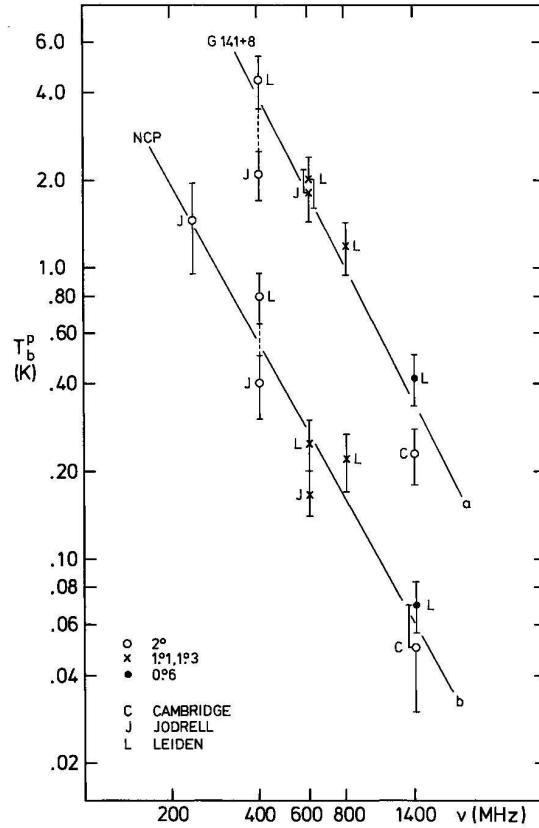
Figure 1.3: Diagram shows polarized brightness temperatures of two frequently used calibration points, derived with different telescopes at various frequencies (from Berkhuijsen, 1975).

relatively constant level of receiver noise, the amount of noise received through the far side lobes – mainly ground radiation – varies as the telescope is tracking a source. This leads to the problem of separating the sky from ground radiation.

If telescope movement is small and hence fluctuations of the ground radiation negligible within a subscan, ground radiation offsets are removed by baseline fitting to good approximation, as done frequently at the Effelsberg 100-m telescope. The obvious drawback of this method is the suppression of large-scale emission that exceeds the size of the map.

The level of ground radiation, however, can be large, because the side lobes extend to very large distances from the main beam and signals are received even from the back side of the telescope. Although suppression of side lobes is usually better than 30 dB, their integrated flux over 4π can be higher than the actual flux received from a source. Therefore the side lobes cannot be neglected in case of absolute measurements.

An absolute calibration of radio data consists of two principal steps. First, a scaling factor must be determined that converts the arbitrary intensity scale of the raw data into physical units. This factor can be found, for example, by mapping standard calibrators (compact sources of known flux) and referring the measured flux to the standard fluxes of these calibrators. Also possible is the injection of calibration signals into the receiver instead of mapping standard calibrators. Second, to measure *absolute* fluxes, the received signal must be separated into noise contributions from the receiver, ground, atmosphere,

and the actual sky signal. If ground radiation has been removed by baseline subtraction missing large-scale emission must be replaced.

Missing large-scale structures must also be replaced in observations made with aperture synthesis telescopes if absolute fluxes are required. Incomplete coverage of the visibility plane leads to missing information in the image plane. This is known as the missing-zero-spacing problem and means that a synthesis telescope is insensitive to emission structures larger than the angle corresponding to its shortest spacing.

Other than in total power maps, in which pixel values are scalar quantities, polarimetry deals with vectors. Each pixel in a polarimetric map is a vector that has a length *and* direction. The recovery of zero-spacings or missing large-scale structures in polarimetric observations always means to correct vectors. Therefore, missing spatial information can affect the data in a much more complicated way than in total power. Its effect on polarized intensity and angle as well as on rotation measures will be discussed now.

1.2.1 The Role of Large-Scale Structures in Polarization Images

Missing large-scale structures can have a significant impact on the morphological information contained in polarization images. The polarized intensity is defined by PI $= \sqrt{U^2 + Q^2}$. Hence, PI is always a positive quantity and, because it is calculated via Stokes U and Q squared, highly sensitive to offsets in U and Q due to large-scale emission. Correction of offsets can turn an object of high polarized intensity into one of seemingly depressed polarized emission relative to its surroundings, and vice versa. In the same way the polarization angle is affected. Moreover, depending on the large-scale structure that is missing, the position of structures can be shifted.

As an example, Figure 1.4 displays maps of polarized intensity, observed with three different types of telescopes: a large-diameter telescope, a small-diameter telescope, and a synthesis telescope. The field contains two distinct objects: the planetary nebula SH2-216 and the supernova remnant HB 9, as well as diffuse polarized emission. In the maps taken from the Canadian Galactic Plane Survey (Taylor et al., 2003) and the EMLS, both objects show enhanced polarized emission. The Low-Resolution DRAO-Survey of Polarized Emission, because of its relatively low resolution, shows only diffuse emission of large spatial extent. This diffuse emission is partly missing in the EMLS and CGPS maps.

After incorporation of zero-spacings the morphological information in the polarized intensity maps from the CGPS and EMLS changes. The planetary nebula becomes less prominent and its nature changes from an emission-type[2] object into an object with less polarized intensity relative to the diffuse emission. Parts of the supernova remnant turn from regions of enhanced polarized intensity into depressed emission. The appearance of the diffuse emission, as well as the position of some of the elongated, canal-like structures changes.

Another example demonstrates how offsets in Stokes U and Q create structures in polarized intensity and affect the polarization angle. In Fig. 1.5 the polarized intensity and position angle taken from a drift scan of the 26-m Survey are displayed. The scan goes through a highly polarized region with polarized intensities of up to 450 mK. The absolute polarization angles are close to $\varphi \approx 45°$ with only small variations of $\Delta\varphi \approx \pm10°$. If offsets in U and Q are removed, the polarization vectors are no longer absolutely calibrated. The polarized intensities are generally lower and show more fluctuations on smaller scales. The polarization angle fluctuates almost over the entire range from $-90°$ to $+90°$. At R.A. $= 89°$, the polarized intensity drops and an angle jump of almost $90°$ appears.

These examples illustrate the effect of missing spatial information on the interpretation of polarized intensities and polarization angles. Objects, which originally emit polarized radiation can appear as

---

[2]Expressions like "emission" and "absorption" must be used with care in polarization, because superposition of differently rotated polarization vectors can result in enhanced or depressed polarized intensity without physically generating or obstructing radiation.

26m–Survey   EMLS   CGPS

26m + EMLS   26m+EMLS+CGPS
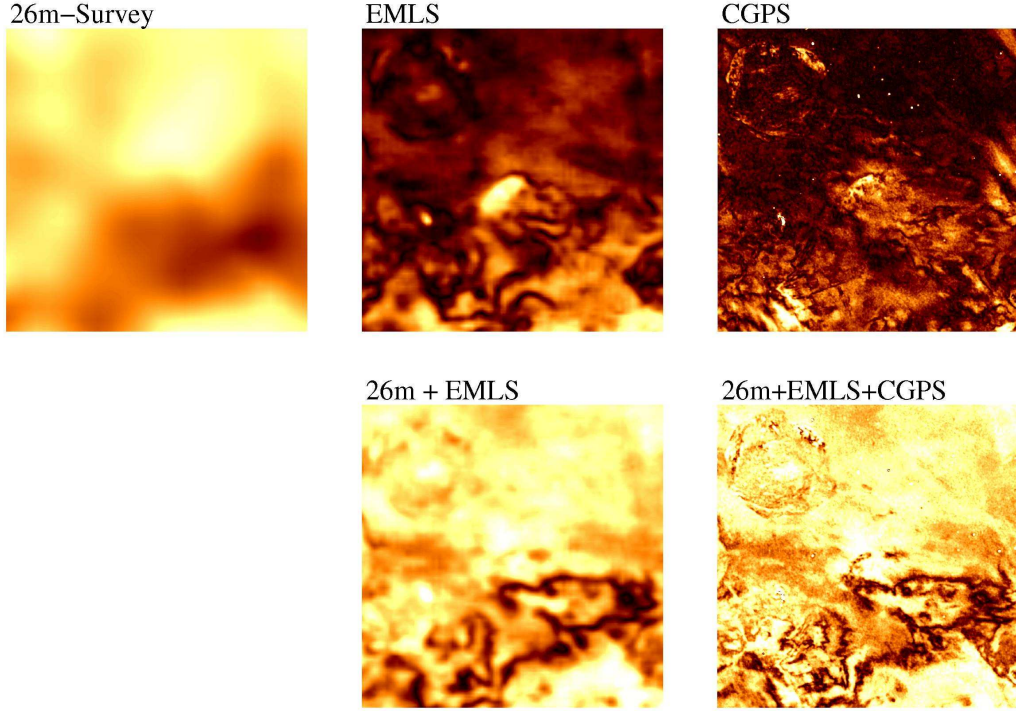
Figure 1.4: The effect of missing spatial information shown on a $7° \times 7°$ large field centred at $l = 158°$, $b = 1°$, observed with three different telescopes. In the top row from left to right: the 26-m Survey (single-antenna), the EMLS (single-antenna), and the CGPS (synthesis telescope). The bottom row shows the combinations of spatial information taken from the EMLS and 26-Survey, and from all three surveys. The images contain the supernova remnant HB 9 (upper left, $\sim 2°$ in size) and the planetary nebula SH2-216 (close to centre, $\sim 1°$ in size).

minima, whereas depolarizing Faraday screens[3] may be observed as enhancements in polarized intensity. The same holds for the angle that may show fluctuations without physical equivalent. In studies of diffuse polarized emission an absolute calibration is therefore mandatory; only in studies of distinct objects an absolute calibration may not be necessary.

1.2.2 The Role of Large-Scale Structures in Rotation Measures

The rotation measure (RM) describes the change of polarization angle as a function of frequency (see Section 2.8). Since the angle is very sensitive to the calibration, as seen in the previous section, how do missing offsets in Stokes U and Q affect RMs? The question will be discussed now whether the polarization angles must be absolutely calibrated or if *relative* angle variations at different frequencies already reveal true rotation measures. This question is of particular interest for RM-studies of diffuse polarized emission.

In the following two different cases will be discussed. The first case describes a Faraday rotating layer situated between a source of polarized emission – the background layer – and the observer (case-

---

[3]A Faraday screen may be an object or layer that causes Faraday rotation.

Figure 1.5: The effect of missing large-scale structures: The left panel shows the polarized intensity (PI) taken from a survey drift scan at 57°.5 declination with large-scale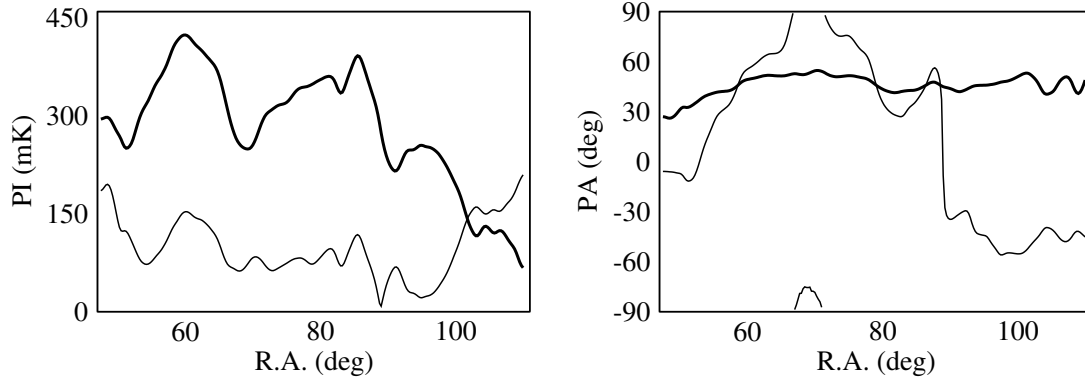 structures (thick line) and without (thin line). The right panel displays the same for the polarization angle (PA). For this example the large-scale structure is approximated by averaging of Stokes U and Q over the right ascension interval displayed.

1, Fig 1.6). This case can be applied to observed emission from distant, compact objects, which can be separated from foreground emission. The second case describes the diffuse Galactic emission in which Faraday rotated background is observed in superposition with unrotated foreground (case-2, Fig 1.6).

Throughout the discussion $\mathbf{B_{1,2}}$ denote background polarization vectors and $\mathbf{F_{1,2}}$ foreground vectors at frequencies ν_1 and ν_2. $\mathbf{B}$ and $\mathbf{F}$ are itself composed of vectors:

$$
\begin{aligned}
\mathbf{B_{1,2}} &= \underbrace{\mathbf{b_{1,2}}}_{\text{offset}} + \underbrace{\beta_{1,2}}_{\text{fluctuations}} \\
\mathbf{F_{1,2}} &= \underbrace{\mathbf{f_{1,2}}}_{\text{offset}} + \underbrace{\varepsilon_{1,2}}_{\text{fluctuations}} ,
\end{aligned}
\tag{1.1}
$$

for which $\mathbf{b}$ and $\mathbf{f}$ shall represent offsets (large-scale structure), and β and ε denote fluctuations (small-scale structure) in polarized emission. This distinction will allow the analysis of differences in absolutely calibrated vectors ($|\mathbf{b_{1,2}}| > 0$, $|\mathbf{f_{1,2}}| > 0$) and those with missing zero-spacings ($|\mathbf{b_{1,2}}| = 0$, $|\mathbf{f_{1,2}}| = 0$).

The observed angle φ_{FR} between the polarization vectors at frequencies ν_1 and ν_2 is

$$
\varphi_{\text{FR}} = \varphi_1 - \varphi_2 = c^2 \left(\frac{1}{\nu_1^2} - \frac{1}{\nu_2^2} \right) \text{RM}_{\text{obs}}
\tag{1.2}
$$

which, if the angle difference is measured, allows the calculation of RM_{obs}. For simplification, the x-components of the foreground and background vectors are assumed to be zero at frequency ν_1, which only means that the vectors are lined up along the y-axis at that frequency (see Figure 1.7). Hence, the position angle of the polarization vector observed at frequency ν_2 is proportional to the observed rotation measure: $\text{RM}_{\text{obs}} \propto \varphi_2$.

In the first case, the background vector $\mathbf{B}$ is Faraday rotated. The observed polarization vector at frequency ν_2 is the vector sum of Faraday rotated offset $\mathbf{b_1}$ and Faraday rotated small-scale structure β_1. Its x- and y-components are:

$$
\begin{aligned}
B_{2,x} &= b_{2,x} + \beta_{2,x} = (b_{1,x} + \beta_{1,x}) \cos\varphi_{\text{FR}} + (b_{1,y} + \beta_{1,y}) \sin\varphi_{\text{FR}} \\
B_{2,y} &= b_{2,y} + \beta_{2,y} = -(b_{1,x} + \beta_{1,x}) \sin\varphi_{\text{FR}} + (b_{1,y} + \beta_{1,y}) \cos\varphi_{\text{FR}}.
\end{aligned}
\tag{1.3}
$$

7

CASE 1

BACKGROUND

RM

OBSERVER

X

RM

BACKGROUND

FOREGROUND   OBSERVER

CASE 2

BACKGROUND
POLARIZED INTENSITY

mK

250

200

150

X

FOREGROUND
POLARIZED INTENSITY

X

RM_{obs} rad/m^2

10

5

0

-5

with offset
without offset

X
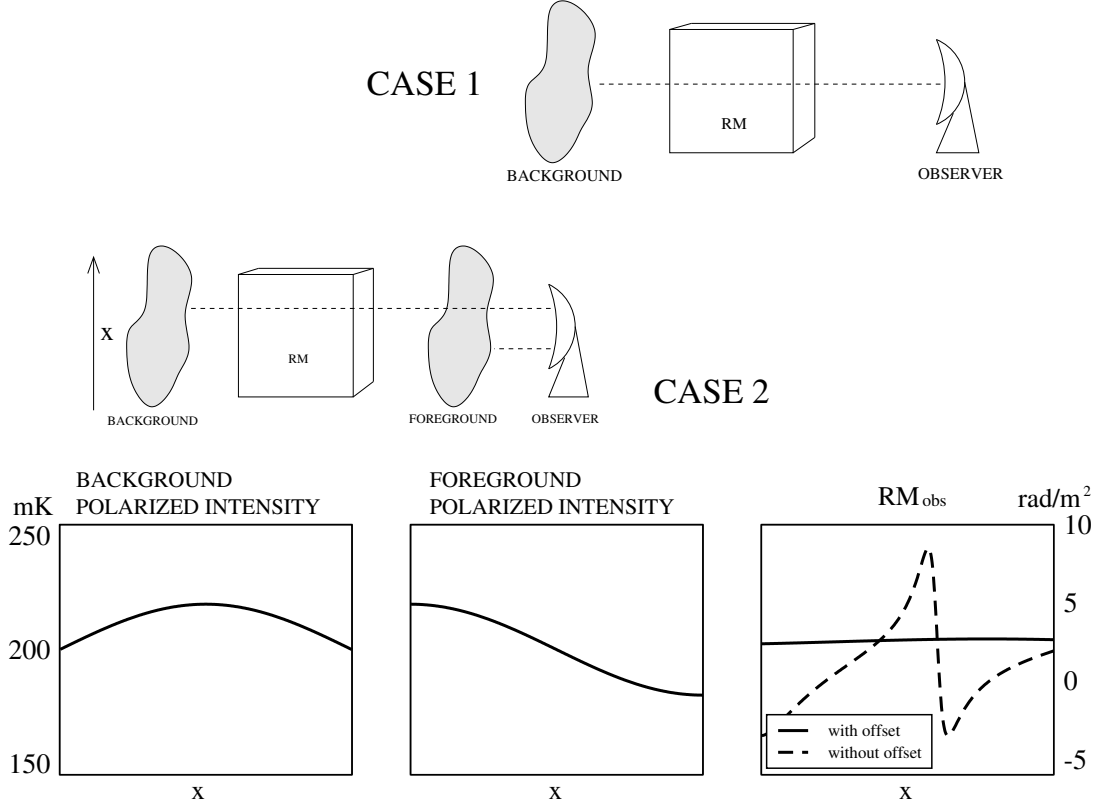
Figure 1.6: The two cases are illustrated: Case-1 with background emission and Faraday rotating layer and case-2 with foreground, background and Faraday rotating layer in between. For the second case, the graphs show the adopted distribution of polarized intensity for foreground and background layer as well as the resulting rotation measure simulated for observations with a telescope sensitive to the large-scale structure (with offsets) and one that is not sensitive to large-scale emission (without offset). This calculation assumes: two observing frequencies at 1400 and 1410 MHz, equal polarization angles of foreground and background with x-components of zero at both frequencies, and RM = 5 rad m^{-2}. Zero spacings (offsets) are removed by subtracting the average of Stokes U and Q before calculating the rotation measure.
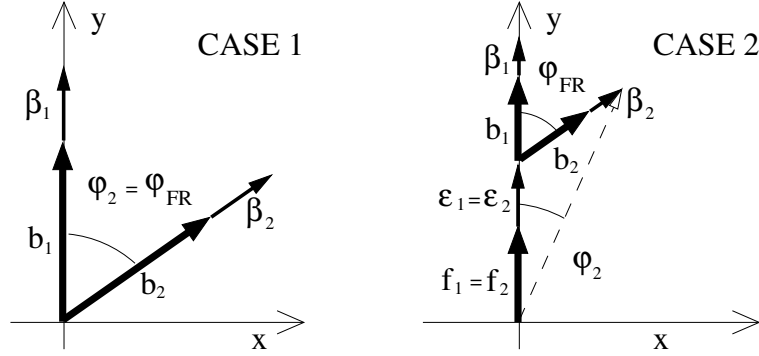
Figure 1.7: Vectors in the two cases: In case-1 only background emission exists. The vector $b_1 + \beta_1$ is rotated against $b_2 + \beta_2$ because of Faraday rotation. The observed angle φ_2 reveals the correct rotation measure ($\varphi_2 = \varphi_{FR}$). In case-2, the rotated background ($b_2 + \beta_2$) is superimposed on an unrotated foreground ($f_1 + \varepsilon_1$). The observed angle φ_2 gives a smaller rotation measure than in case-1 ($\varphi_2 \neq \varphi_{FR}$).

The polarization vector observed at ν_1 is assumed parallel to the y-axis so that $b_{1,x} = \beta_{1,x} = 0$. Therefore, the position angle of B_2 relative to the y-axis is proportional to the observed rotation measure. Its tangens is given by

$$\tan\varphi_2 = \frac{B_{2,x}}{B_{2,y}} = \frac{(b_{1,y} + \beta_{1,y})\sin\varphi_{FR}}{(b_{1,y} + \beta_{1,y})\cos\varphi_{FR}} = \tan\varphi_{FR} \quad \Rightarrow \quad \varphi_2 = \varphi_{FR}. \tag{1.4}$$

It follows that the angle difference between polarization vectors observed at frequency ν_1 and ν_2 reveal RM correctly whether derived from absolutely calibrated data or from data with missing zero-spacings.

In case-2, which includes foreground emission, the observed polarization vector at frequency ν_2 is the composition of unrotated foreground $\mathbf{F_1}$ and rotated background. According to Fig. 1.6:

$$\begin{aligned} F_{2,x} + B_{2,x} &= f_{1,x} + \varepsilon_{1,x} + (b_{1,x} + \beta_{1,x})\cos\varphi_{FR} &+& (b_{1,y} + \beta_{1,y})\sin\varphi_{FR} \\ F_{2,y} + B_{2,y} &= f_{1,y} + \varepsilon_{1,y} - (b_{1,x} + \beta_{1,x})\sin\varphi_{FR} &+& (b_{1,y} + \beta_{1,y})\cos\varphi_{FR}. \end{aligned} \tag{1.5}$$

Again, with the simplification that all x-components are zero at frequency ν_1, the tangens of the position angle of the polarization vector at frequency ν_2 is

$$\tan\varphi_2 = \frac{(b_{1,y} + \beta_{1,y})\sin\varphi_{FR}}{f_{1,y} + \varepsilon_{1,y} + (b_{1,y} + \beta_{1,y})\cos\varphi_{FR}}. \tag{1.6}$$

Here, φ_2 becomes a function of the foreground vectors:

$$\begin{aligned} \varphi_2 &= \arctan\left(\frac{2(b_{1,y}+\beta_{1,y})\tan\frac{\varphi_{FR}}{2}}{f_{1,y}+\varepsilon_{1,y}+b_{1,y}+\beta_{1,y}+f_{1,y}\tan^2\frac{\varphi_{FR}}{2}+\varepsilon_{1,y}\tan^2\frac{\varphi_{FR}}{2}-b_{1,y}\tan^2\frac{\varphi_{FR}}{2}-\beta_{1,y}\tan^2\frac{\varphi_{FR}}{2}}\right) \\ &\Rightarrow \quad \varphi_2 \neq \varphi_{FR} \quad |f_{1,y}| > 0, \end{aligned} \tag{1.7}$$

which, if the foreground ($f_{1,y}, \varepsilon_{1,y}$) is zero, becomes $\varphi_2 = \varphi_{FR}$ and case-2 transforms into case-1.

These results can be summarized as follows: Without foreground emission, absolute and relative polarization angles result in equal RM. But if polarized foreground emission is present, the RMs derived from data with missing offsets can largely differ from RMs calculated on the basis of absolutely calibrated data. In this case, RMs can be smaller or larger than the absolute rotation measures, depending

on the foreground polarization. As case-2 applies to the interstellar medium it is highly desirable to use absolutely calibrated data for rotation measure studies of the diffuse polarized emission.

1.3 Absolutely Calibrating Polarization Surveys

Different types of telescopes require different methods for the absolute calibration of polarization observations. With small-diameter telescopes (e.g. Dwingeloo 25-m, DRAO 26-m, etc.), at frequencies between $\sim$ 100 MHz and $\sim$ 10 GHz, it may not be possible to find polarized compact sources suitable for the calibration, because, if observed with a small telescope, the commonly used calibrators are too weak to be detectable against the diffuse polarized background. On the other hand, large-aperture telescopes (e.g. Effelsberg 100-m, synthesis arrays) have the resolution to map compact sources with high response, which allows accurate determination of the relative temperature or flux density scale, but usually do not preserve absolute fluxes.

This section describes how polarimetric data can be absolutely calibrated. Three types of absolute calibration are necessary in practise: 1. an *independent* absolute calibration of single-antenna observations, mostly applied to small-diameter telescopes (e.g. LDS); 2. an absolute calibration of single-antenna observations on the basis of low-resolution data (e.g. Effelsberg 100-m combined with Stockert 25-m); and 3. the adding of zero-spacings and offsets to synthesis data.

1.3.1 Independent Absolute Calibration

For independent measurements of absolute antenna temperatures the relative temperature scale must be determined, as well as the noise contributions from the receiver, ground, atmosphere and the source disentangled. As instances of the method, two polarization surveys are mentioned here:

- For the Leiden-Dwingeloo polarization survey at 820 MHz (Berkhuijsen, 1971) the relative temperature scale was obtained by comparing the recorded intensities with calibrated noise signals added to the sky signal during the observations. The equivalent temperature of the calibration signals was known, and loads in liquid nitrogen at a temperature of 78 K were used as reference. Data were corrected for ground radiation by subtracting an empirical stray radiation model.

- For the LDS reference points of known polarized intensity and angle were observed with rotating dipoles for the calibration of the system. During measurement the dipole was rotated by 360°, which causes the polarization vector to rotate twice in the U-Q plane, while the length of the vector, the polarized intensity, remains constant. The recorded outputs consisted of double sine curves from which Stokes U and Q could be derived. These sine curves were corrected for ground radiation on the basis of ground radiation profiles.

Much effort went into the calculation and measurement of ground radiation profiles for these surveys. At telescopes such as the Dwingeloo or DRAO 26-m, spillover and ground radiation dominates the signal and must be known precisely. The problem is the strong dependence on elevation and azimuth, which is the result of the telescopes's response pattern and the surrounding landscape. Time-variability makes correction for ground radiation more complicated. This is why precise calculation is difficult and ground radiation profiles are usually measured by making sweeps in elevation from horizon to zenith.

To correct for instrumental polarization, the response of the receiving system to unpolarized radiation – the response or antenna pattern – must be measured for all Stokes parameters. At small telescopes and frequencies around 1 GHz or less, often Cassiopeia-A and the Sun are the only sources that are strong enough to be used for the mapping of the response pattern. In many studies, the correction of main-beam instrumental polarization is sufficient. But even compact sources with lower intensities can increase instrumental polarization if observed through the side lobes.

1.3.2 Absolute Calibration on the Basis of Low-Resolution Data

Whereas the measurement of ground radiation is time consuming, available observing time at large-diameter telescopes (e.g. Effelsberg 100-m) is usually limited. Moreover, ground radiation is time-variable and the measured profiles may not be accurate enough; not a problem if enough observing time is available to either measure ground radiation profiles frequently or set up an observing scheme that allows software correction. Therefore, observations with large single-antenna telescopes can often not adequately be corrected for ground radiation, and large-scale structures must be recovered by comparison with low-resolution surveys.

Especially the Effelsberg 100-m telescope is located in a valley with surrounding hills, which introduces a strong dependence of the ground radiation on azimuth. Other large-diameter telescopes such as the Parkes telescope, the Green-Bank telescope or Jodrell Bank have flatter surroundings and should therefore show smaller azimuthal dependencies at low elevation.

1.3.3 Absolute Calibration of Synthesis Data

For observations obtained with aperture synthesis telescopes, various different approaches and data reduction packages can be used for the incorporation of zero-spacings. Some operate in the Fourier domain and merge single-antenna and synthesis data involving tapering of the Fourier plane (linear method), and some use both data sets for a joint deconvolution (non-linear method). Mosaicing can also help to recover short spacings.

In interferometric observations, ground radiation is "filtered out" by the cross-correlation, because each individual antenna of an array receives its own ground radiation and ground radiation signals of pairs of antennas are uncorrelated. Therefore, it is usually not necessary to correct for ground and spillover noise in continuum observations made with synthesis telescopes.

1.4 Scientific Justification for the 26-m Survey

For studies of diffuse polarized emission the data must be absolutely calibrated to contain low spatial frequencies correctly. So far, the only data base of absolutely calibrated polarization data usable for the absolute calibration of the recent 1.4 GHz polarization surveys is the LDS, consisting of measurements of individual, well calibrated pointings. But these data are undersampled. In many areas pointings are several degrees apart and often only a small number of data points can be used for calibration. Reich & Wielebinski (2000) therefore suggested new low-resolution observations that should exceed the LDS but include its absolute calibration. Their publication provides the groundwork for the 26-m Survey.

Recent polarization observations (Gray et al., 1998, 1999; Uyaniker et al., 1999; Duncan et al., 1998) reveal small-scale structures and objects detectable only by their Faraday effects on polarized emission. The study of these objects opens a new window for the investigation of the magneto-ionic medium of the Galaxy. Unexpected results such as Faraday screens associated with molecular clouds (Wolleben & Reich, 2004), canal-like depressions in the polarized intensity (Haverkorn et al., 2004b), or bubbles and superbubbles revealed by their Faraday rotation (Kothes et al., 2004b) can only be investigated in their Galactic context if large-scale polarized emission is included in the analysis. The 26-m Survey provides this large-scale structure with reasonable resolution.

Studies of the rotation measure of the diffuse polarized emission, by establishing structure functions, reveal the typical scale of fluctuations in the magneto-ionic medium (Haverkorn et al., 2004a). As shown in Section 1.2.2, RM-studies should be based on absolutely calibrated data otherwise the results are unphysical. Although the 26-m Survey provides only a single observing frequency, it could still be used for a tentative calibration of the frequency bands used for some of these studies.

Currently, so called foreground templates for the separation of Galactic emission from the cosmic microwave background (CMB) are constructed by using the highly undersampled LDS (e.g. Bernardi et al., 2004). At 1.4 GHz the 26-m Survey provides 100 times more data points and can thus serve as a much better sampled data base for the derivation of CMB templates.

Spectral line polarimetry is a novel technique that allows detection of absorption lines in polarized emission due to neutral hydrogen. This technique was proofed by Dickey (1997) toward diffuse polarized emission and later applied by Kothes et al. (2004a) to supernova remnants. Both studies used synthesis telescopes. Once this technique is applicable to single-antenna telescopes, the 26-m Survey will allow selection of targets and calibration of spectra, necessary for the interpretation of the spectra.

A fully sampled polarization survey of the southern sky with similar resolution and sensitivity will soon become available (Testori et al., 2004). As there are no absolutely calibrated data available for the southern sky, this survey will be absolutely calibrated by adjusting baselines on the southern celestial pole and the overlap region with the 26-m Survey. The combination of both surveys will result in the first all-sky polarization map at 1.4 GHz.

1.4.1 Scope of the Project

An independent calibration as applied to the early polarization surveys (Section 1.3) requires exact knowledge of telescope parameters as well as an investigation of ground and stray radiation. Although the telescope parameters of the DRAO 26-m Telescope have been determined for total power (Higgs & Tapping, 2000), its properties regarding polarimetric observations were unknown prior to this project. Hence, an independent absolute calibration could not be considered within the telescope time allocated for this project and therefore a joint calibration scheme, which is between an independent absolute calibration and a calibration on the basis of low-resolution data, is applied:

- The LDS provides absolutely calibrated reference points at declinations $\geq 0°$.

- While surveying the sky, a large fraction of the reference points from the LDS is observed by drift scanning.

- The reference points are used for the determination of system parameters such as instrumental polarization, response ellipse and tentative brightness temperature scale. Reference points with polarized brightness temperatures around zero define zero-levels in Stokes U and Q.

- The main-beam brightness temperature scale is refined by comparison with data taken from the EMLS.

The aim is to rely on the LDS only for the calibration of the system parameters and the definition of zero-levels in Stokes U and Q. No *spatial* information from the LDS is used for the absolute calibration of the 26-m Survey. The reference points are rather used as standard calibrators with known flux in U and Q.

The 26-m Telescope availability and hence the timeline of the observing part of the project was 1 year with a net observing time of 7 months. Since observations are restricted to night-time only ($\sim$ 12 h), the maximum sky coverage achievable in that time is 22.4% for declinations between $-27°$ and $+90°$.

2 Wave Polarization in Radio Astronomy

This chapter gives a brief summary of the basic formalism used in this thesis. For a more general introduction into the concepts and their application to radio astronomy the reader is referred to the books of Born & Wolf (1965), Kraus (1966), and Tinbergen (1996).

2.1 Monochromatic Waves

Throughout the thesis, δ refers to phases of electric field vectors and φ to their polarization angle. E denotes an electric field and V the voltage of this field.

The electric field of a harmonic, monochromatic plane wave at fixed location in space can be described by electric field components in the x- and y-directions:

$$
\begin{aligned}
E_x(t) &= A_1 \, e^{i\omega t} \\
E_y(t) &= A_2 \, e^{i\omega t},
\end{aligned}
\tag{2.1}
$$

which are two linearly polarized waves with orthogonal polarization directions and the circular frequency ω. The complex amplitudes A_1, A_2 are $A_1 = a_1 \, e^{i\delta_1}$, $A_2 = a_2 \, e^{i\delta_2}$, with the real amplitudes a_1, a_2 and phases δ_1, δ_2. The absolute phases of A_1 and A_2 are not important, only the relative phase $\delta = \delta_2 - \delta_1$ matters so that:

$$
\begin{aligned}
A_1 &= a_1 \\
A_2 &= a_2 \, e^{i\delta}.
\end{aligned}
\tag{2.2}
$$

The electric field vector of *arbitrary* polarization then reads:

$$
\mathbf{E}(t) = \underbrace{\begin{pmatrix} A_1 \\ A_2 \end{pmatrix}}_{\text{Jones vector}} e^{i\omega t} = \left(a_1 \mathbf{e}_x + a_2 \mathbf{e}_y e^{i\delta} \right) e^{i\omega t}
\tag{2.3}
$$

in which $\mathbf{e}_x$ and $\mathbf{e}_y$ are unit vectors of a Cartesian coordinate system.

The electric field vector $\mathbf{E}(t)$ is a complex number. It is understood that this is the *analytic* representation of a plane harmonic wave. To obtain a *physically* meaningful quantity, for instance the voltage $V(t)$ within the radio receiver, one has to take the real part of Equation 2.3:

$$
V(t) = \mathcal{Re} \left[\left(A_x \mathbf{e}_x + A_y \mathbf{e}_y \right) e^{i\omega t} \right].
\tag{2.4}
$$

In general, the imaginary part of the analytic signal does not physically exist. Also, whenever nonlinear operations are applied to the electric field vector such as squaring, etc., the real parts must be taken first and the operation is applied to these alone. This, however, is not necessary if the time average of a quadratic expression is required.

Linear Polarization Components

Two special states of polarization are of particular importance: linear and circular. These are special cases of elliptically polarized waves which are the general form of polarization.

(a) Linear Polarization

If the relative phase difference δ of the two components can be described by:

$$\delta = m\pi \quad (m = 0, \pm 1, \pm 2, \dots), \tag{2.5}$$

then, at $t = 0$, equation 2.3 becomes:

$$\mathbf{E} = a_1 \mathbf{e}_x + a_2 \mathbf{e}_y (-1)^m. \tag{2.6}$$

The polarization or position angle φ of the electric field vector is defined by:

$$\tan \varphi = \frac{E_y}{E_x} = (-1)^m \frac{a_2}{a_1}. \tag{2.7}$$

With the amplitudes a_1 and a_2 expressed by the amplitude a_0 of the initial wave and the polarization angle φ:

$$\begin{aligned} a_1 &= a_0 \cos \varphi \\ a_2 &= a_0 \sin \varphi, \end{aligned} \tag{2.8}$$

the polarization state of a *linearly* polarized wave is completely described by a_0 and φ in terms of two *linear* polarization components.

(b) Circular Polarization

A wave is circularly polarized if $a_0 = a_1 = a_2$ and

$$\delta = \frac{m\pi}{2} \quad (m = \pm 1, \pm 3, \pm 5, \dots). \tag{2.9}$$

At $t = 0$, equation 2.3 becomes:

$$\mathbf{E} = a_0 \left(\mathbf{e}_x + \mathbf{e}_y i^m \right), \tag{2.10}$$

which is denoted right-handed circularly polarized if:

$$\frac{E_y}{E_x} = i, \tag{2.11}$$

or left-handed circularly polarized if:

$$\frac{E_y}{E_x} = -i. \tag{2.12}$$

This describes a *circularly* polarized wave in terms of two *linear* polarization components. A circularly polarized wave does not have a polarization angle.

Circular Polarization Components

An initially linear polarized wave ($\delta = 0$) cannot only be expressed in terms of linear polarization components as done in equation 2.6, but also in terms of circular components. It depends on the design

of the feed which basis is provided. The electric field vectors for the left and right handed components are:

$$
\begin{aligned}
E_r &= \tfrac{1}{2}\left(a_1 + ia_2\right) e^{i\omega t} &= \tfrac{1}{2}\left(a_1 e^{i\omega t} + a_2 e^{i(\omega t + \pi/2)}\right) \\
E_l &= \tfrac{1}{2}\left(a_1 - ia_2\right) e^{i\omega t} &= \tfrac{1}{2}\left(a_1 e^{i\omega t} + a_2 e^{i(\omega t - \pi/2)}\right).
\end{aligned}
\tag{2.13}
$$

The unit vectors of circular polarization components are:

$$
\begin{aligned}
\mathbf{e}_r &= \tfrac{1}{\sqrt{2}}(\mathbf{e}_x + i\mathbf{e}_y) \\
\mathbf{e}_l &= \tfrac{1}{\sqrt{2}}(\mathbf{e}_x - i\mathbf{e}_y).
\end{aligned}
\tag{2.14}
$$

The amplitudes of E_r and E_l of an initially linearly polarized wave can be shown to be equal to $a_0/2$, the amplitude of the initial wave, independent of its polarization angle φ:

$$
|A_r| = |A_l| = \left(A_r A_r^\star\right)^{\frac{1}{2}} = \frac{1}{2}\left(a_1^2 + a_2^2\right)^{\frac{1}{2}} = \frac{a_0}{2},
\tag{2.15}
$$

here the star indicates complex conjugate.

The phase difference between E_r and E_l can be calculated by taking the voltages:

$$
\begin{aligned}
V_r(t) = \tfrac{1}{2}\left(E_r + E_r^\star\right) &= \tfrac{1}{4}\left[a_1\left(e^{i\omega t} + e^{-i\omega t}\right) + ia_2\left(e^{i\omega t} - e^{-i\omega t}\right)\right] \\
&= \tfrac{1}{2}\left(a_1 \cos \omega t - a_2 \sin \omega t\right) \Rightarrow \delta_r = -\arctan\left(\tfrac{a_2}{a_1}\right) \\
V_l(t) = \tfrac{1}{2}\left(E_l + E_l^\star\right) &= \tfrac{1}{4}\left[a_1\left(e^{i\omega t} + e^{-i\omega t}\right) - ia_2\left(e^{i\omega t} - e^{-i\omega t}\right)\right] \\
&= \tfrac{1}{2}\left(a_1 \cos \omega t + a_2 \sin \omega t\right) \Rightarrow \delta_l = \arctan\left(\tfrac{a_2}{a_1}\right).
\end{aligned}
\tag{2.16}
$$

The relative phase difference thus is:

$$
\Delta\delta = \delta_l - \delta_r = 2\arctan\left(\frac{a_2}{a_1}\right) = 2\varphi,
\tag{2.17}
$$

which is an important result. By expressing a linearly polarized wave in terms of two circular components, the polarization angle of the initial wave is transformed into a phase difference between the circular components, whereas the amplitudes of the circular components are proportional to the amplitude of the initial wave.

2.2 Stokes Parameters

Three independent parameters are needed to describe the polarization state of the initial vector wave. In case of linear polarization components these are the amplitudes a_x, a_y and the relative phase δ. If circular polarization components are used, the initial wave is described by the amplitudes a_r, a_l and the relative phase δ. A practical way of expressing these parameters is by the use of the so-called Stokes parameters. The following relation exists – by definition – between Stokes parameters and the amplitude and phase of the polarization components:

$$
\begin{aligned}
I &= a_x^2 + a_y^2 &= a_r^2 + a_l^2 \\
Q &= a_x^2 - a_y^2 &= 2\,a_r a_l \cos \delta \\
U &= 2\,a_x a_y \cos \delta &= 2\,a_r a_l \sin \delta \\
V &= 2\,a_x a_y \sin \delta &= a_r^2 - a_l^2.
\end{aligned}
\tag{2.18}
$$

2.3 Partial Polarization

A single electromagnetic wave is fully polarized. In nature, however, electromagnetic radiation is produced by a large ensemble of radiators, producing incoherent waves. Incoherent radiation may still show statistical correlation between the polarization components. This can be interpreted as partial polarization to a certain degree. It can be shown that waves emitted by astronomical sources are quasi-monochromatic and that Stokes parameters are then given by time averages:

$$
\begin{aligned}
I &= \langle a_x^2 \rangle + \langle a_y^2 \rangle &= \langle a_r^2 \rangle + \langle a_l^2 \rangle \\
Q &= \langle a_x^2 \rangle - \langle a_y^2 \rangle &= 2 \langle a_r a_l \cos\delta \rangle \\
U &= 2 \langle a_x a_y \cos\delta \rangle &= 2 \langle a_r a_l \sin\delta \rangle \\
V &= 2 \langle a_x a_y \sin\delta \rangle &= \langle a_r^2 \rangle - \langle a_l^2 \rangle .
\end{aligned}
\tag{2.19}
$$

2.4 Polarization Measurements

An analog polarimeter does not measure the amplitudes and phase differences of the polarization components directly, it rather detects time averaged products of the two components such as the following product of the *x*- and *y*-components:

$$
\left\langle V_x V_y \right\rangle = \lim_{T' \to \infty} \frac{1}{4T'} \int_{-T'}^{T'} \left(E_x + E_x^\star \right) \left(E_y + E_y^\star \right) \, dt.
\tag{2.20}
$$

With

$$
\frac{1}{2T'} \int_{-T'}^{T'} e^{2i\omega t} \, dt = \frac{T}{4\pi T'} \sin 2\omega T' \approx 0
\tag{2.21}
$$

for $T' \gg T$ the time-averaged product becomes:

$$
\left\langle V_x V_y \right\rangle \propto A_x A_y^\star + A_x^\star A_y = a_x a_y \cos\delta
\tag{2.22}
$$

and hence a measure for Stokes U. Using the analytic representation, this equation can be written as:

$$
\left\langle V_x V_y \right\rangle = \mathcal{R}e \left(E_x E_y^\star \right) = a_x a_y \cos\delta.
\tag{2.23}
$$

Time averaging the other possible products gives other Stokes parameters, which leads to the following variant of the definition of Stokes parameters:

$$
\begin{aligned}
I &= \left\langle E_x E_x^\star \right\rangle + \left\langle E_y E_y^\star \right\rangle &= \left\langle E_r E_r^\star \right\rangle + \left\langle E_l E_l^\star \right\rangle \\
Q &= \left\langle E_x E_x^\star \right\rangle - \left\langle E_y E_y^\star \right\rangle &= 2 \mathcal{R}e \left(E_r E_l^\star \right) \\
U &= 2 \mathcal{R}e \left(E_x E_y^\star \right) &= 2 \mathcal{I}m \left(E_r E_l^\star \right) \\
V &= 2 \mathcal{I}m \left(E_x E_y^\star \right) &= \left\langle E_r E_r^\star \right\rangle - \left\langle E_l E_l^\star \right\rangle .
\end{aligned}
\tag{2.24}
$$

2.5 The Jones Matrix

The system components of the receiver modify the polarization state of the received radiation. A well designed polarimetric receiver provides linear or circular polarization components. The electronic system, however, may introduce relative gain and phase differences between these two components. These imperfections are most generally described by matrices. The design goal of receivers is to keep imperfections small so that only first-order approximations are required. The complex Jones matrix (Jones,

1941) is the transfer function for the voltages between the input and output signals of the receiver:

$$\begin{pmatrix} V_a \\ V_b \end{pmatrix}_{\text{out}} = \mathcal{J} \cdot \begin{pmatrix} V_x \\ V_y \end{pmatrix}_{\text{in}} = \begin{pmatrix} j_{11} & j_{12} \\ j_{21} & j_{22} \end{pmatrix} \cdot \begin{pmatrix} V_x \\ V_y \end{pmatrix}_{\text{in}} \tag{2.25}$$

The output voltages are denoted V_a and V_b as they do not have to be linear polarization components after being transformed by the Jones matrix.

The instrument can be split into successive parts through which the signals pass. For instance, radiation is first reflected by the antenna ($\mathcal{J}_{\text{antenna}}$), then collected through the horn ($\mathcal{J}_{\text{horn}}$), converted into linear polarization components by the polariser ($\mathcal{J}_{\text{polariser}}$), and then transformed into circular components by a hybrid ($\mathcal{J}_{\text{hybrid}}$). The electronic amplifiers may also introduce different gains and phases ($\mathcal{J}_{\text{electronics}}$). The total Jones matrix of such an instrument would read:

$$\mathcal{J} = \mathcal{J}_{\text{electronics}} \cdot \mathcal{J}_{\text{hybrid}} \cdot \mathcal{J}_{\text{polariser}} \cdot \mathcal{J}_{\text{horn}} \cdot \mathcal{J}_{\text{antenna}}. \tag{2.26}$$

2.6 The Müller Matrix

The Müller matrix (Mueller, 1948) is the transfer function for the signal power, the Stokes parameters. To every Jones matrix exists a Müller matrix. Its entries are real numbers:

$$\begin{pmatrix} S_1 \\ S_2 \\ S_3 \\ S_4 \end{pmatrix}_{\text{out}} = \mathcal{M} \cdot \begin{pmatrix} I \\ Q \\ U \\ V \end{pmatrix}_{\text{in}} = \begin{pmatrix} m_{II} & m_{IQ} & m_{IU} & m_{IV} \\ m_{QI} & m_{QQ} & m_{QU} & m_{QV} \\ m_{UI} & m_{UQ} & m_{UU} & m_{UV} \\ m_{VI} & m_{VQ} & m_{VU} & m_{VV} \end{pmatrix} \cdot \begin{pmatrix} I \\ Q \\ U \\ V \end{pmatrix}_{\text{in}}. \tag{2.27}$$

Depending on the Müller matrix the components of the output vector may not be associated with Stokes parameters I, Q, U, and V, they may rather be linear combinations of these. The elements of the matrix are derived by calculating the outer products of the Jones matrix:

$$m_{ij} = \frac{1}{2}\text{tr}\left(\sigma_i \mathcal{J} \sigma_j \mathcal{J}^\dagger\right), \tag{2.28}$$

with σ being Pauli matrices. The Müller matrix entries expressed by elements of the Jones matrix are listed in Appendix A.

2.7 Radio Emission Mechanism

At 1.4 GHz radio emission is basically produced by two radiation mechanism: synchrotron emission, and thermal (free-free) emission. Briefly, these mechanisms are described as follows:

Synchrotron emission: Relativistic electrons moving in a magnetic field are decelerated and convert a small fraction of their kinetic energy into radio emission. The strength of the synchrotron emission depends on the magnetic field strength, while its spectrum reflects the energy spectrum of the relativistic electrons. The intensity of the emitted radiation is:

$$I(\nu) \propto L B_\perp^{(\gamma+1)/2} \left(\frac{1}{\nu}\right)^{(\gamma-1)/2}, \tag{2.29}$$

with pathlength L and energy spectralindex γ. Only synchrotron emission is polarized. The

degree of polarization is:

$$p = \frac{\gamma + 1}{\gamma + \frac{7}{3}}. \tag{2.30}$$

Thermal emission: Free-free emission is emitted when electrons are deflected by ions. Because of the randomness of the scattering, thermal emission is unpolarized. The emission measure EM is given by:

$$\frac{\text{EM}}{\text{pc cm}^{-6}} = \int\limits_{0}^{s/\text{pc}} \left(\frac{N_\text{e}}{\text{cm}^{-3}} \right)^2 d\left(\frac{s}{\text{pc}} \right). \tag{2.31}$$

2.8 Faraday Rotation

The polarization plane of a linearly polarized electromagnetic field rotates, if propagating through a magnetized plasma. This effect is known as Faraday rotation. Faraday rotation can be understood as the result of a difference between the propagation velocities for right- and left-handed polarized radiation. Since a linearly polarized wave can be composed of two circularly polarized waves, the retardation of one of the circularly polarized waves relatively to the other results in a rotation of the sum, the linearly polarized wave.

The degree of Faraday rotation by which the polarization angle is rotated (FR), is given by the product of rotation measure RM and wavelength λ squared:

$$\text{FR} = \lambda^2 \, \text{RM}, \tag{2.32}$$

in which the rotation measure RM is defined by the integral over the line-of-sight:

$$\text{RM} = 0.81 \int_0^L B_\parallel(l) \, n_\text{e}(l) \, dl, \tag{2.33}$$

with RM in rad m^{-2}, the magnetic field strength parallel to the line-of-sight $B_\parallel$ in μG, the electron density n_e in cm^{-3}, and the line-of-sight length L in pc. It is important to keep in mind that only if $B_\parallel(l)$ and $n_\text{e}(l)$ are uncorrelated, Equation 2.33 can be written as:

$$\text{RM} = 0.81 \, B_\parallel \, n_\text{e} \, L. \tag{2.34}$$

3 Receiving Equipment and Observations

The observational part of this project involves hardware as well as software issues. To allow polarimetric observations, the receiver of the DRAO 26-m telescope requires modifications. The backend system must be set up and software needs to be written to control receiver and polarimeter. Before observing is started the receiver is tested and an observing scheme is developed. This chapter describes the main aspects of performing the survey: 1. hardware issues including frontend, backend, and receiver modifications; 2. development of software; 3. system errors produced by the receiving system and how to correct them; and 4. the observing scheme.

3.1 Hardware

Although a well suited receiver of the DRAO 26-m telescope can be utilized for this project, a few modifications of the receiver circuit were necessary. Subsequently, complete testing of the receiver is unavoidable to identify and remove possible sources of systematic errors. The signals are processed by the backend device – an analog polarimeter shipped from the Max-Planck-Institut für Radioastronomie in Bonn, which is of the type used at the Effelsberg 100-m telescope. In addition to hardware work, software needed to be developed for the read-out of four polarimeter channels as well as the data processing and storage of raw data. The following describes, in more detail, the receiver modifications.

3.1.1 The DRAO 26-m Telescope

The 26-m telescope (Figure 3.1) was build in 1959. Since then, it has been frequently used for spectroscopy of Galactic H I and OH. It is a deep paraboloid ($f/D = 0.3$, where f is the focal distance and D the diameter of the antenna) with an open-mesh surface. The telescope has a diameter of 25.6 m and is located at $-119°\ 37.2'$ longitude and $+49°\ 19.2'$ latitude. The antenna was originally intended for use at 1.4 GHz. At this frequency the aperture efficiency is 55% (10 Jy/K). The antenna surface allows observations at frequencies from about 400 MHz to about 8.4 GHz. At 6.6 GHz the aperture efficiency falls to 11%. Only few observations have been made towards the upper limit of the frequency band. The receiver box is mounted on three support-struts which are arranged at an angle of $33°5$ to the antenna boresight. Different primary focus boxes are available, hosting receivers operating at different frequencies.

The antenna is on a polar mount and can observe the sky between $-34°$ and $+90°$ declination. Survey observations were limited to declinations $\geq -27°$. The rms pointing accuracy is 0.8′ (Knee, 1997). Observations are usually scheduled several days in advance with the telescope left unattended.

3.1.2 Cross-Correlation of Radio Signals

In radio astronomical receivers operating in the Megahertz and lower Gigahertz range, a number of methods are used to stabilize the gain of the receiving system. Gain fluctuations of the amplifier chain and the 1/f-noise limit the detectability of weak radio signals. Aside from circuit designing the amplifiers as stable as possible, principles like the Dicke switch have been applied in the past. Polarimetric

Figure 3.1: The 26-m telescope of the DRAO with the institute buildings in the background.

measurements with present-day receivers are done by *cross-correlating* the polarization components provided by the feed, which improves sensitivity.

The cross-correlation function of two ergodic processes producing the signals $s_1(t)$ and $s_2(t)$ of the real variable t is defined by:

$$\text{ccf} = \lim_{T \to \infty} \frac{1}{2T} \int_{-T}^{T} s_1(t) s_2(t + \tau) \, d\tau. \tag{3.1}$$

The cross-correlation expresses to which degree the two signals are correlated. The integral in Equation 3.1 is a time average so that ccf can be written as:

$$\text{ccf} = \langle s_1(t) \, s_2(t + \tau) \rangle. \tag{3.2}$$

Supposing that $V_1(t)$ and $V_2(t)$ are the noise voltages of two stochastic signals corresponding to two hands of polarization. If received with an uncooled receiver such as the one at the DRAO 26-m telescope, a large fraction of $V_1(t)$ and $V_2(t)$ is uncorrelated receiver noise; the sky only contributes a few percent of correlated – and hence polarized – signal:

$$
\begin{aligned}
V_1 &= G_1 \, (V_{\text{rec1}} + V_{\text{sky1}}) \\
V_2 &= G_2 \, (V_{\text{rec2}} + V_{\text{sky2}}),
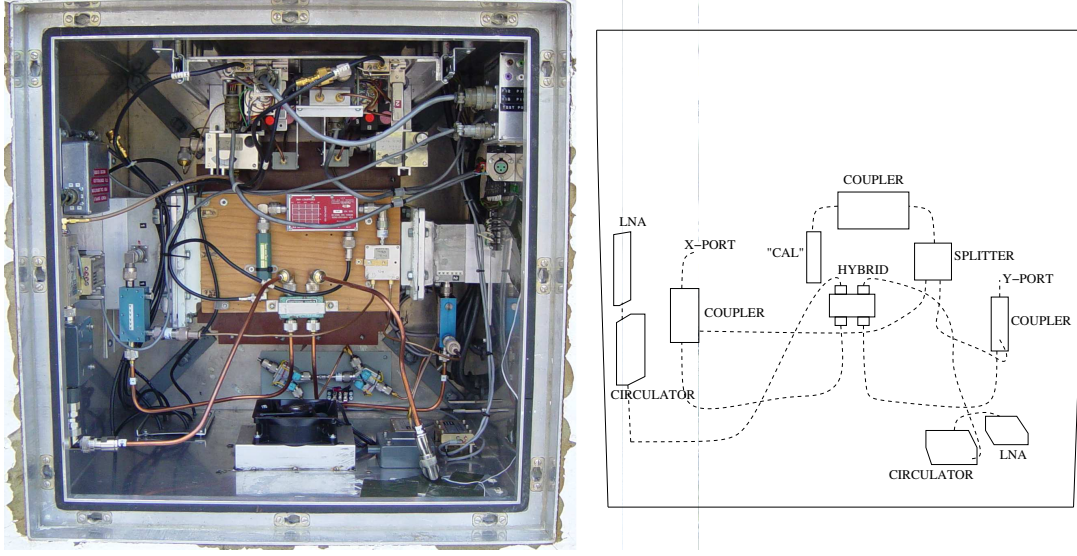\end{aligned}
\tag{3.3}
$$

20

Figure 3.2: The 1.4 GHz receiver of the DRAO 26-m telescope from the inside, reconfigured for po-
larimetry.

with G_1 and G_2 the real gain in the two channels.

To measure the cross-correlation function of $V_1(t)$ and $V_2(t)$ a device is needed that multiplies the signals and averages the product. With Equation 3.2 and $\tau = 0$ the cross-correlation reads ccf = $\langle V_1(t)\, V_2(t) \rangle$ and yields:

$$\text{ccf} = G_1 G_2 \left\langle V_{\text{rec1}} V_{\text{rec2}} + V_{\text{rec1}} V_{\text{sky2}} + V_{\text{rec2}} V_{\text{sky1}} + V_{\text{sky1}} V_{\text{sky2}} \right\rangle. \tag{3.4}$$

The time averages of all products containing V_{rec1} and V_{rec2} are zero because the receiver noise in both channels is uncorrelated and only

$$\text{ccf} = G_1 G_2 \langle V_{\text{sky1}} V_{\text{sky2}} \rangle \tag{3.5}$$

remains.

This is an important principle. Gain errors do not affect the correlation products when there is no polarization. This means that even with gain fluctuations, the product of the two hands of polarization remains zero for unpolarized sources. Moreover, gain variations will change only the calibration of the receiver and not affect the sensitivity. This makes the measurement of weak polarization more accurate.

3.1.3 The Receiver

Receivers at the DRAO 26-m telescope are hosted by focus boxes (see Figure 3.2). These boxes are thermally isolated and temperature controlled by a thermalelectric heater and cooler. Air circulation keeps the receiver temperature constant at 21°C. To allow observations at different frequencies, different boxes hosting various receivers can be installed. The 1.4 GHz receiver used for this survey was originally designed for spectroscopy of H I and OH lines, but the dual polarization design allows polarimetric observations as well.

Figure 3.3 shows a block diagram of the modified receiver that is used for this survey. The frontend consists of a corrugated flange feed (scalar feed) through which the radio signals enter the receiver. The
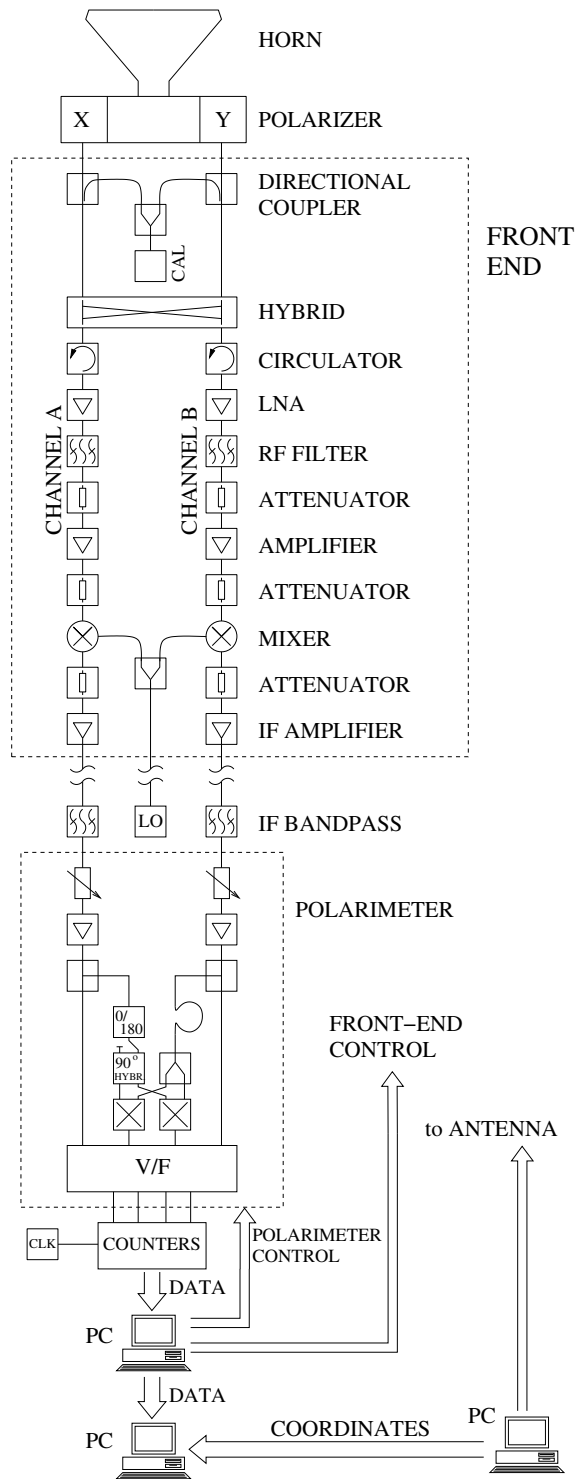
Figure 3.3: Block diagram of the 1410 MHz continuum receiver of the DRAO 26-m telescope after reconfiguration for polarimetry.

Table 3.1: Receiver and antenna specifications

Telescope coordinates	$-119°\ 37.2'$, $+49°\ 19.2'$
Antenna diameter	25.6 m
HPBW (effective)	36′
Aperture efficiency	55%
Bandwidth (November 2002)	12 MHz (10 MHz)
Poiting accuracy	0.8′
Intermediate frequency	150 MHz
System temperature	161 K
Gain variations in 30 days	$\lesssim 4\%$
Ambient temperature stability of the receiver	$\sim 1°C$
Phase tracking across band	$\sim 5°$

feed, which is scaled from a feed designed at the MPIfR, is followed by a piece of circular waveguide and a circular-to-square transition. A dual polarization coupler (DPC) splits the initial input signal into its linear polarization components: E_x and E_y. A calibration signal is injected into the X- and Y-lines through directional couplers. The two signal lines are then cross-coupled by a quadrature hybrid, which is followed by circulators. Two low-noise amplifiers (LNA) amplify the signals. The signals then go through bandpass filters centred at 1412.5 MHz with a 1 dB bandwidth of 35 MHz. The bandpass is followed by attenuation and more amplification. Subsequently, the signals are send into mixers which turn the radio frequency (RF) signals into intermediate frequency (IF) signals centred at 150 MHz. After being once more attenuated, amplified, and bandpass filtered the IF-signals enter the polarimeter. The polarimeter has four output channels, which are connected to the data acquisition PC and continuously read-out.

Receiver Modifications

The original receiver does not have a quadrature hybrid and therefore provides linear polarization components. From the definition of the Stokes parameters (Equation 2.18) it can be seen that cross-correlating linear components does not yield measures for the polarization state of a linearly polarized incoming wave. Although not used at the final receiver, the correlation products of linear components are now calculated for demonstration. Let E_x and E_y be the two analytic representations of a linearly polarized signal corresponding to equation 2.2:

$$
\begin{aligned}
E_x &= a_1 e^{i\omega t} \\
E_y &= a_2 e^{i\omega t}.
\end{aligned}
\tag{3.6}
$$

According to the receiver block diagram (Figure 3.3), the polarimeter performs two multiplications. It calculates the simple product of the two polarization components and the product in which one of the two components is phase shifted by 90°:

$$
\begin{aligned}
E_x E_y^\star &= a_1 a_2 \\
E_{x,-\frac{\pi}{2}} E_y^\star &= a_1 a_2 e^{-i\frac{\pi}{2}}.
\end{aligned}
\tag{3.7}
$$

The time-averages of these products are:

$$
\begin{aligned}
XY &= \mathcal{R}e(E_x E_y^\star) &= a_1 a_2 &= \frac{a_0^2}{2}\sin 2\varphi &\longrightarrow \text{Stokes } U \\
YX &= \mathcal{R}e(E_{x,-\frac{\pi}{2}} E_y^\star) &= a_1 a_2 \cos\frac{\pi}{2} &= 0 &\longrightarrow \text{Stokes } V,
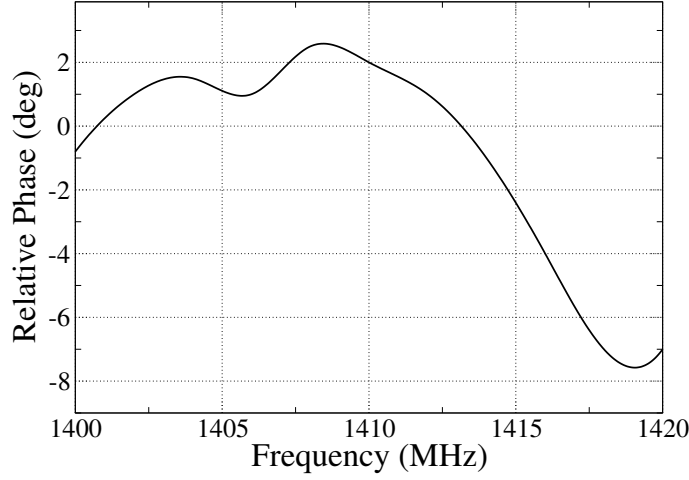\end{aligned}
\tag{3.8}
$$

Figure 3.4: Phase tracking of the two polarization components before entering the polarimeter, measured without IF bandpass filters. The observing frequency is 1410 MHz and the bandwidth is 12 MHz.

which are measures of Stokes U and V, respectively. Linear polarization, however, is described by Stokes U and Q. To measure U and Q, the linear polarization components provided by the DPC must be transformed into circular components.

The transformation of linear into circular components is achieved by installation of additional HF-devices and modification of the receiver circuit as follows:

- A quadrature hybrid is incorporated into the receiver.

- Circulators between the hybrid and the LNA are used to improve matching.

- A number of phase matched cables are necessary to adjust pathlengths and circuit wiring.

These additional system component have resistance and therefore rise the system temperature. Resistance is equivalent to a source of noise. This noise is of the same nature as the signal received from the astronomical source and can therefore not be distinguished. The noise temperature T_L of an attenuator at ambient temperature T_{amb} with loss L measured in dB is given by:

$$T_L = (10^{\frac{L}{10}} - 1)\, T_{amb}. \tag{3.9}$$

Gain and phase measurements of the entire system are made to maximize sensitivity to polarized signals. The following details are worth mentioning:

- The relative phase difference of the two polarization components, measured at the X and Y-port of the DPC, depends on frequency. Before entering the hybrid, this phase mismatch must be compensated. Measurements show that over a frequency band of 100 MHz the relative phase mismatch is about 10°. Good phase matching can therefore only be achieved for a fixed observing frequency and a relatively small bandwidth ($\lesssim 100$ MHz).

- Different pairs of IF bandpass filters were used in November 2002, the first observing month, and December 2002 through May 2003. It was noticed that the first set of filters introduced an additional phase mismatch of 7° across the observing band. Therefore, they were replaced by better ones with a phase match as good as 3°.
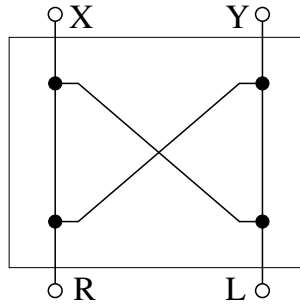
Figure 3.5: Functional block diagram of a quadrature hybrid.

- The phase match of the system without IF bandpass filters is shown in Figure 3.4.

The following system components are important for the signal processing within the frontend and are therefore described in more detail:

Quadrature-Hybrid

The DPC is designed to uncouple the two linear polarization components of an incoming polarized signal. In principle, the system could be changed to circular components by implementing a quarter-wave plate into the horn. Instead of altering the horn, a quadrature hybrid is used, which has the same effect.

A hybrid is a passive device without amplification. According to Figure 3.5, a signal applied to port X or Y splits equally between ports R and L with one of the outputs exhibiting a relative $90°$ phase delay. A very simple hybrid can be made of a ring-like metal plate, with connectors every $\lambda/4$ attached to it. The commercially fabricated hybrids are more sophisticated, but basically the output signals (R, L) are formed by linear combinations of the two input signals, one of them with the phase unchanged, and one with a $90°$ phase shift introduced. Hence, the outputs read:

$$
\begin{aligned}
R &= \tfrac{1}{2}(X + Y_{+\pi/2}) \\
L &= \tfrac{1}{2}(Y + X_{+\pi/2}) = \tfrac{1}{2}(X + Y_{-\pi/2}).
\end{aligned}
\tag{3.10}
$$

The implementation of a quadrature hybrid is essential. But where should it be incorporated? The two possibilities are: 1. as a *pre-amp* hybrid between the horn and the LNA; or 2. as a *post-amp* hybrid somewhere between the LNA and the polarimeter. The first option – ahead of the LNA – seems less convenient, because the hybrid, due to its loss, increases the receiver temperature much more than in the pre-amp case. However, implementing the hybrid behind the amplifier means that the two linear components (X, Y) are amplified before being transformed into circular components. Gain variations of the amplifiers therefore result in more complicated amplitude and phase variations of the R- and L-components. Such a system would not provide the advantage of cross-correlation for measuring weak signals, because now gain variations do change the sensitivity and produce fake polarization if there is none. Hence, despite the increase in system temperature, the hybrid must be incorporated ahead of the LNA, as a pre-amp hybrid.

The hybrid at the DRAO 26-m telescope is uncooled ($T_{\mathrm{amb}} \approx 290$ K) and has a loss of about 0.3 dB. According to equation 3.9, it increases the receiver temperature by approximately 20 K. The integration of the hybrid requires the incorporation of additional cables. The loss along 1 m of coax cable is of the order of 0.15 dB, which introduces additional 10 K receiver noise.

Circulators

Circulators are added in to improve matching between the hybrid and the LNAs. This prevents backscattering of signals from the X- and Y-ports of the hybrid into the other, which would produce cross-talk and thus increase instrumental polarization.

A ferrite circulator or isolator is a device that allows RF to flow between two adjacent ports. This flow is restricted to one direction only. The transmission line is placed between ferrite material and magnets. The magnetic field induced by the magnets allows RF to pass in one direction without being attenuated, but not in the other direction.

The isolators used here have an insertion loss of about 0.25 dB and an isolation in the reverse direction of about -30 dB. According to Equation 3.9 the insertion loss rises the system temperature by about 17 K.

Calibration Noise Source

A calibration signal is generated by a noise source, Noise/Com Inc Model NC3101E, generating a signal of constant amplitude. The "cal" is switched on every 24 s for a duration of 400 ms. The signal is split and injected through directional couplers and thus produces a correlated, polarized, signal at the X- and Y-ports of the hybrid.

Although the hybrid transforms a relative amplitude difference of E_x and E_y into a relative phase difference between E_r and E_l, and a relative phase difference between E_x and E_y into a relative amplitude difference of E_r and E_l, the gain and phase of the cal, measured at the X- and Y-port of the hybrid, do not have to be well matched. Important is that the cal produces signals in R and L that have constant amplitude and phase. This is then recorded as a constant reference signal in the RL and LR cross-correlations. The reference signals in RL and LR are later transformed into polarized intensity and polarization angle.

The directional couplers, through which the cal signal is injected, have an insertion loss of about 0.2 dB on their main line. This adds additional 15 K to the receiver noise.

Low-Noise Amplifiers

Low-noise amplifiers are specifically designed to have a high gain and a comparatively low thermal noise. The LNAs used here are two Berkshire (L-1.4-45HR) build in 1991. They have a quoted gain of 57.0 dB, and 51.6 dB, respectively. The thermal noise of these amplifiers is about 30 K. These LNAs are based on HEMT transistors.

3.1.4 System Temperature

Because of their loss, the receiver components contribute thermal noise. This raises the effective noise temperature of the receiver. The receiver temperature T_{rec} is the sum of all noise contributions within the receiver. In case of the DRAO 26-m receiver, and in most other receivers used in radio astronomy, several amplification stages are combined serially as a cascade of amplifiers. It can be shown that the receiver temperature of a cascaded system is:

$$T_{\mathrm{rec}} = T_1 + \frac{1}{G_1}T_2 + \frac{1}{G_1 G_2}T_3 + \cdots + \frac{1}{G_1 G_2 \ldots G_{n-1}}T_n, \tag{3.11}$$

(see e.g. Rohlfs & Wilson, 1996, for derivation) with T_n and G_n being the noise temperature and gain in the n-th amplification stage. Therefore, only the receiver components ahead of the first amplifier

contribute significantly to the receiver temperature. In case of the receiver used for this survey, these are the horn, DPC, couplers, hybrid, and circulators.

The system temperature is the sum of receiver temperature and all other noise contributions such as antenna temperature. Antenna noise originates from the sky background, ohmic losses, and ground pickup or spillover from side lobes (atmospheric noise and the actual sky signal). Along with bandwidth and integration time, the system temperature determines the sensitivity of the receiver. The rms noise temperature T_{rms} of the system is defined by:

$$T_{rms} = \frac{C_s\, T_{sys}}{\sqrt{B\, t}}, \tag{3.12}$$

with bandwidth B and integration time t. The constant C_s depends on the type of receiver used for the observations.

Adding the above listed noise contributions and allowing additional 60 K for ground radiation, atmospheric effects and other noise sources, the system temperature without sky emission results in about 160 K. In case of total power observations, the constant C_s is unity (see various textbooks, e.g. Kraus, 1966, p. 258). With a bandwidth of 12 MHz and an integration time of 60 s per pixel, the theoretical rms due to receiver noise in total power is 6 mK.

The polarimetric measurements are done on correlated signals. The constant C_s is in case of a correlation receiver 0.71 and the theoretical rms in the cross-correlated channels thus calculates to 4 mK. These are theoretical values. The final errors in Stokes U and Q are greater for reasons discussed later (Section 4.3).

3.1.5 Polarimeters

The only backend device utilized for this survey is a continuum polarimeter brought to DRAO from Effelsberg. The S300-4 narrow band polarimeter is capable of performing the analog multiplication of three individual input channels of which only two are used here. The same type of polarimeter is used on the Effelsberg 100-m telescope for narrow band polarimetry. Prior to shipping, a few modifications of the polarimeter were made. All coax cables and lines were checked and replaced, if necessary. The internal multipliers were substituted by new ones with improved performance and the transformers were replaced to stabilize power supply.

A multiplying polarimeter is a correlator that calculates products of the incoming signals. Usually these signals are the two polarization components of the received radio waves, ideally perfect linear or circular. Different types of polarimeters are described now with an emphasis on analog polarimeters.

Analog Multiplying Polarimeter

Let E_x and E_y be the two analytic signals representing linear polarization components of a linearly polarized radio wave ($\delta = 0$) with amplitude A_0 and position angle φ:

$$\begin{aligned} E_x &= A_x e^{i\omega t} \\ E_y &= A_y e^{i\omega t}, \end{aligned} \tag{3.13}$$

with

$$\begin{aligned} A_x &= A_0 \cos\varphi \\ A_y &= A_0 \sin\varphi. \end{aligned} \tag{3.14}$$

In case of the DRAO 26-m-telescope receiver, linear components are transformed into circular by the hybrid:

$$\begin{aligned} E_r &= 0.5 \left(A_x\, e^{i\omega t} + A_y\, e^{i\left(\omega t - \frac{\pi}{2}\right)} \right) \\ E_l &= 0.5 \left(A_x\, e^{i\left(\omega t - \frac{\pi}{2}\right)} + A_y\, e^{i\omega t} \right). \end{aligned} \tag{3.15}$$

These signals are fed into the polarimeter. Correlation of E_r and E_l yields:

$$\begin{aligned} E_r E_l^\star &= \tfrac{1}{4} \left(A_x e^{i\omega t} + A_y e^{i\left(\omega t - \frac{\pi}{2}\right)} \right) \left(A_x e^{-i\left(\omega t - \frac{\pi}{2}\right)} + A_y e^{-i\omega t} \right) \\ &= \tfrac{1}{2} A_x A_y + \tfrac{i}{4} \left(A_x^2 - A_y^2 \right). \end{aligned} \tag{3.16}$$

The time-average of this product is $\mathcal{R}e\,(E_r E_l^\star)$. With the amplitudes of the linear polarization components A_x and A_y, this gives:

$$\mathrm{RL} = \mathcal{R}e\,(E_r E_l^\star) = \frac{1}{2}\,A_x A_y = \frac{A_0^2}{4}\,\sin 2\varphi \quad \longrightarrow \quad \text{Stokes } U. \tag{3.17}$$

According to the definition of the Stokes parameters, this product corresponds to Stokes U. This polarimeter channel is also called the sine-channel.

To achieve full information on the polarization state the polarimeter calculates a second product: the product of E_r and E_r, with E_r phase-delayed by $90°$. The correlation then yields:

$$\begin{aligned} E_{r,-\frac{\pi}{2}} E_l^\star &= \tfrac{1}{4} \left(A_x e^{i\left(\omega t - \frac{\pi}{2}\right)} + A_y e^{i\left(\omega t - \pi\right)} \right) \left(A_x e^{-i\left(\omega t - \frac{\pi}{2}\right)} + A_y e^{-i\omega t} \right) \\ &= \tfrac{1}{4} \left(A_x^2 - A_y^2 \right) - \tfrac{i}{2} A_x A_y \end{aligned} \tag{3.18}$$

with the time-average of this product:

$$\mathrm{LR} = \mathcal{R}e\,(E_{r,-\frac{\pi}{2}} E_l^\star) = \frac{1}{4} \left(A_x^2 - A_y^2 \right) = \frac{A_0^2}{4}\,\cos 2\varphi \quad \longrightarrow \quad \text{Stokes } Q, \tag{3.19}$$

which corresponds to Stokes Q. This polarimeter channel is also called the cosine-channel. The sine- and cosine-channels provide all information required to fully describe the polarization state of a linearly polarized radio wave. In case of partial polarization Stokes I is also required.

In analog correlators the multiplication of the two input signals is done by multipliers. Such a multiplier takes advantage of the equation: $(A + B)^2 - (A - B)^2 = 4AB$. Hence, the product of A and B is determined by detecting the sum and difference of the two signals with square-law detectors, and subsequently subtracting these signals. In practise, analog multipliers are subject to gain errors and non-linearities. In particular the products contain quadratic terms in the form:

$$AB + \alpha A^2 + \beta B^2, \tag{3.20}$$

whereas α and β are usually small. Moreover, the products have DC offsets which are sensitive to the ambient temperature. In case of the S300 polarimeter, the amplitude of fluctuations of the DC term is orders of magnitudes larger than signals caused by polarized radiation from the sky.

To handle quadratic terms and DC offsets, the correlation products are calculated twice: at first with the relative phase between the two components unchanged and a second time with one of the two input signals phase shifted by $180°$. This causes the sign of the product AB to change, but not the sign of the quadratic terms and DC offsets. The phase shifter is switched periodically between zero and $180°$. The pure correlation products can be recovered by taking the difference of the phase shifted and unshifted

correlator outputs:

$$\begin{aligned} RL &= 0.5\,(RL_0 - RL_{180}) \\ LR &= 0.5\,(LR_0 - LR_{180}). \end{aligned} \tag{3.21}$$

Digital Cross-Correlator

Digital cross-correlators are often used in synthesis telescopes but also some single-antenna telescopes cross-correlate signals digitally (e.g. the Green-Bank Telescope). The inputs of such a correlator are digitized samples of data from each antenna or each hand of polarization. The output of a correlator is the cross-correlation function (ccf) of data received in a finite time interval, which is adapted to the bandwidth used for the observation. The digitized data within the time interval are called "lags".

By Fourier transforming ccf consisting of N lags, a cross-power spectrum with N channels is obtained. As ccf is antisymmetric about $\tau = 0$ (Equation 3.1) the Fourier transformation results in a complex spectrum. If circular polarization components are correlated, the real and imaginary parts of the Fourier transformed ccf correspond to Stokes U and Q.

A correlator in which the correlation is followed by a Fourier transformation is called XF-correlator. It is called FX-correlation if the signals are first Fourier transformed and then multiplied.

Other Types of Polarimeters

In bolometric receivers the signals of the two hands of polarization are detected by square-law detectors and thus phase information is not preserved. Stokes parameters are retrieved by adding and subtracting the detected power levels in the following way:

$$\begin{aligned} I &= RR + LL \\ Q &= RR - LL. \end{aligned} \tag{3.22}$$

Stokes U is measured by rotation of the plane of polarization with respect to the feed. In such polarimeters, small quantities (U, Q) are derived by subtraction or addition of two large quantities (RR, LL). The gain in the two channels must therefore be sufficiently stable, a challenging design goal. These types of polarimeters are sometimes used in bolometric receivers mapping the CMB polarization at frequencies around 100 GHz (e.g. Siringo et al., 2004; Tauber, 2004).

Another type of polarimeter is the adding polarimeter, which consists of a network of 90°- and 180°-hybrids performing phase-correct additions. Instead of calculating products of E_r and E_l such a polarimeter has the following outputs (see e.g. von Hoensbroech & Xilouris, 1997):

$$\begin{aligned} \text{channel 1} &= \left\langle |E_r|^2 \right\rangle = \left\langle E_r E_r^\star \right\rangle \\ \text{channel 2} &= \left\langle |E_l|^2 \right\rangle = \left\langle E_l E_l^\star \right\rangle. \end{aligned} \tag{3.23}$$

Total power I and Stokes V are derived from:

$$\begin{aligned} I &= \text{channel 1} + \text{channel 2} \\ V &= \text{channel 2} - \text{channel 1}. \end{aligned} \tag{3.24}$$

Stokes U and Q are as follows:

$$\begin{aligned} U &= \text{channel 4} - I \\ Q &= I - \text{channel 3}. \end{aligned} \tag{3.25}$$

Calibration is required to find scaling factors for total power I and the correlator output channels 3 and 4. Again, the gain of the signals fed into such a polarimeter must be stable because Stokes U and Q are given by differences of large and small quantities.

3.1.6 System Adjustments

The implementation of a hybrid requires the adjustment of relative gain and phase of the receiver channels carrying the two hands of polarization. As the DPC provides linear polarization components a hybrid is used to form circular polarization hands out of linear. Within the hybrid this is done by phase delaying and adding the linear components. But the hybrid as well as other receiver components introduce errors in terms of phase and gain mismatches between the two components. These mismatches affect the sensitivity of the receiving system to polarized signals and must be compensated by adjustment of cable length and integration of attenuators in the receiver circuit.

The following questions must be investigated to estimate the importance of system adjustments and recognize systematic errors in the data :

- How do phase and gain mismatches of the linear polarization components (E_x, E_y) in the pre-hybrid part affect the measurement of Stokes U and Q?

- How do gain and phase mismatches of the circular polarization components in the post-hybrid (E_r, E_l) affect the cross-correlations (RL, LR)?

- The input signals have a bandwidth of 12 MHz. How do phase slopes across the observing band alter the cross-correlations.

It now follows a discussion of these questions.

Phase- and Gain-Matching in the Pre-Hybrid Part

The adjustment of relative power levels and phases in the X and Y signal paths of the receiver, ahead of the hybrid, must be discussed. There are no active devices, such as amplifiers, in this part of the receiver. All devices are passive and power level mismatches either reflect different polarization angles of the incoming signal or are caused by different attenuation of the receiver components.

A phase mismatch may be caused, for example, by different cable lengths or the DPC itself. To calculate the effect of mismatches of the power levels and phases in the pre-hybrid part, the two *complex* gains $g_x = G_x\,e^{i\epsilon_x}$ and $g_y = G_y\,e^{i\epsilon_y}$ are introduced, with the two *power* gains G_x and G_y, and the pre-hybrid phase error $\Delta\epsilon_{xy} = \epsilon_x - \epsilon_y$. The linear polarization components are then expressed by:

$$
\begin{aligned}
E_x &= G_x A_x\, e^{i(\omega t+\epsilon_x)}\\
E_y &= G_y A_y\, e^{i(\omega t+\epsilon_y)}.
\end{aligned}
\tag{3.26}
$$

After passing through the hybrid the two linear polarization components are transformed into circular:

$$
\begin{aligned}
E_r &= \tfrac{1}{2}\left(G_x A_x\, e^{i(\omega t+\epsilon_x)} + G_y A_y\, e^{i(\omega t+\epsilon_y-\pi/2)}\right)\\
E_l &= \tfrac{1}{2}\left(G_x A_x\, e^{i(\omega t+\epsilon_x-\pi/2)} + G_y A_y\, e^{i(\omega t+\epsilon_y)}\right).
\end{aligned}
\tag{3.27}
$$

The real parts of the products measured with an analog polarimeter are:

$$
\begin{aligned}
\text{RL} &= \mathcal{R}e(E_r E_l^\star) &&= \tfrac{1}{2}G_x G_y A_x A_y \cos\Delta\epsilon_{xy}\\
\text{LR} &= \mathcal{R}e(E_{r,-\frac{\pi}{2}} E_l^\star) &&= \tfrac{1}{4}\left(G_x^2 A_x^2 - G_y^2 A_y^2\right).
\end{aligned}
\tag{3.28}
$$

With the polarization angle φ, $A_x = A_0 \cos\varphi$, and $A_y = A_0 \sin\varphi$ this becomes:

$$
\begin{aligned}
\text{RL} &= \tfrac{1}{4}A_0^2 G_x G_y \sin 2\varphi \cos\Delta\epsilon_{xy}\\
\text{LR} &= \tfrac{1}{8}A_0^2\left(G_x^2 - G_y^2 + \left(G_x^2 + G_y^2\right)\cos 2\varphi\right)
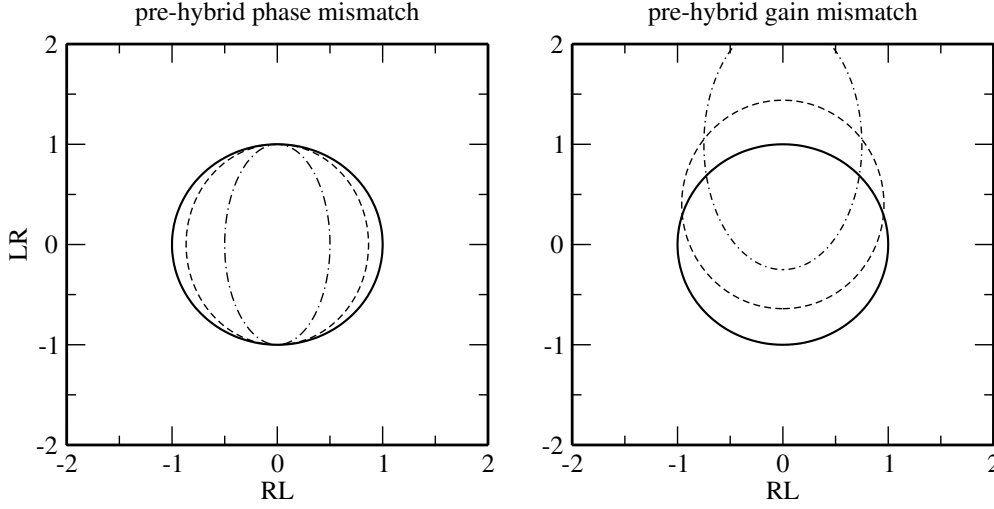\end{aligned}
\tag{3.29}
$$

Figure 3.6: Calculated response of the system taking phase errors $\Delta\epsilon_{xy}$ and power level (G_x, G_y) mismatches in the pre-hybrid part into account. In the left panel is shown, with $G_x = 1$ and $G_y = 1$: $\Delta\epsilon_{xy} = 0°$ (thick line), $\Delta\epsilon_{xy} = 30°$ (dashed line), and $\Delta\epsilon_{xy} = 60°$ (dash-dotted line). The right panel shows, with $\Delta\epsilon_{xy} = 0°$: $G_x = G_y = 1$ (thick line), $G_x = 1.2$ and $G_y = 0.8$ (dashed line), and $G_x = 1.5$ and $G_y = 0.5$ (dash-dotted line).

How does a phase mismatch in the pre-hybrid part affect the cross-correlation products? Equations 3.29 show that RL is sensitive to the cosine of the phase error $\Delta\epsilon_{yx}$, whereas LR is not affected by a phase mismatch. Hence, a phase mismatch results in an elliptical response, meaning that the amplitude of the cross-correlation products depends on the polarization angle of the incoming polarized signal (Figure 3.6). In practise, the X- and Y-components should be brought "in phase" before entering the hybrid to improve the sensitivity of the receiver. This can be achieved by adjusting the cable length between the horn and the hybrid.

Furthermore, Equations 3.29 show that a power level mismatch in the pre-hybrid part also leads to an uneven response and thus reduces the sensitivity to polarized emission. The centre of the response ellipse is shifted along the LR-axis (Figure 3.6). The gain can be adjusted by incorporation of attenuators.

To summarize: Gain and phase mismatches in the pre-hybrid part of the receiver cause uneven response and by this reduce the sensitivity of the system. Therefore, in the receiver configuration set up for this survey, no active devices sensitive to gain and phase fluctuations are incorporated ahead of the hybrid.

Phase- and Gain-Matching in the Post-Hybrid Part

The effects of gain and phase mismatches in the post-hybrid part are now discussed. The following assumes a perfectly matched pre-hybrid part with $\Delta\epsilon_{xy} = 0°$ and $G_x = G_y = 1$. The two complex gains for the post-hybrid part are then $g_r = G_r\,e^{i\epsilon_r}$ and $g_l = G_l\,e^{i\epsilon_l}$, with the post-hybrid phase error $\Delta\epsilon_{rl} = \epsilon_r - \epsilon_l$. After passing through the hybrid, the two circular polarization components are:

$$
\begin{aligned}
E_r &= \tfrac{1}{2}G_r\,e^{i\epsilon_r}\left(A_x\,e^{i\omega t} + A_y\,e^{i(\omega t - \pi/2)}\right)\\
E_l &= \tfrac{1}{2}G_l\,e^{i\epsilon_l}\left(A_x\,e^{i(\omega t - \pi/2)} + A_y\,e^{i\omega t}\right).
\end{aligned}
\tag{3.30}
$$

The cross-correlation products are:

$$
\begin{aligned}
E_r E_l^\star &= \tfrac{1}{4} G_r G_l \left(2 A_x A_y + i(A_x^2 - A_y^2) \right) e^{i\Delta\epsilon_{rl}} \\
E_{r,-\frac{\pi}{2}} E_1^\star &= \tfrac{1}{4} G_r G_l \left(A_x^2 - A_y^2 - i 2 A_x A_y \right) e^{i\Delta\epsilon_{rl}}.
\end{aligned}
\tag{3.31}
$$

Taking the real-part yields:

$$
\begin{aligned}
\mathrm{RL} &= \mathcal{R}e(E_r E_l^\star) &&= G_r G_l \left(\tfrac{1}{2} A_x A_y \cos\Delta\epsilon_{rl} - \tfrac{1}{4}(A_x^2 - A_y^2) \sin\Delta\epsilon_{rl} \right) \\
\mathrm{LR} &= \mathcal{R}e(E_{r,-\frac{\pi}{2}} E_1^\star) &&= G_r G_l \left(\tfrac{1}{2} A_x A_y \sin\Delta\epsilon_{rl} + \tfrac{1}{4}(A_x^2 - A_y^2) \cos\Delta\epsilon_{rl} \right).
\end{aligned}
\tag{3.32}
$$

Expressing A_x and A_y by A_0 and the polarization angle φ gives:

$$
\begin{aligned}
\mathrm{RL} &= \tfrac{1}{4} G_r G_l A_0^2 \left(\sin 2\varphi \cos\Delta\epsilon_{rl} - \cos 2\varphi \sin\Delta\epsilon_{rl} \right) \\
\mathrm{LR} &= \tfrac{1}{4} G_r G_l A_0^2 \left(\sin 2\varphi \sin\Delta\epsilon_{rl} + \cos 2\varphi \cos\Delta\epsilon_{rl} \right).
\end{aligned}
\tag{3.33}
$$

Unlike for mismatches in the pre-hybrid part, gain variations in the post-hybrid part change the cross-correlation products linearly and are therefore easily to detect and to correct. Phase variations, which may be caused by amplifier drifts, expansion or shrinkage of cables due to temperature variations for instance only rotate the RL-LR coordinate system and do not change the receiver response. This means that gain and phase mismatches in the post-hybrid part are corrected during the data calibration without loss of sensitivity.

Continuum Polarimetry

So far the discussion of receiver adjustments was focused on monochromatic waves. But continuum observations are done by integrating the signal over a certain frequency band. In polarimetric measurements it is important to ensure sufficient phase tracking over the observing band. Different cable lengths in the post-hybrid RF- and IF-parts cause runtime differences of the signal across the band. It is therefore common practise to correct phase mismatches by adjusting the cable length in either of the two receiver channels until equal signal runtime is achieved.

Poor phase tracking in the post-hybrid part causes bandwidth depolarization. This means that, if polarization angles of received radiation vary over the observing band, the vector sum results in a decreased polarized intensity. If the variation of the polarization angle is introduced within the receiver, the sensitivity of the receiving system is decreased.

Figure 3.7 shows the sensitivity of a receiving system calculated for a linear phase gradient across the observing band. If the phase gradient reaches $60°$ over the bandwidth the sensitivity is reduced by 5%. At an IF of 150 MHz signal runtime can simply be adjusted by inserting a few more centimeters of cable in the preceding channel. In the receiver used for this survey, the phase tracking measured without IF filters is better than $5°$ (Figure 3.4). The phase tracking is better than $10°$ when the IF filters are included. In practise this means no significant loss of sensitivity.

3.2 Computer and Software

The computer system of the DRAO 26-m telescope was mainly developed to allow spectroscopic observations. Several programs exist for scheduling of observations, controlling the antenna and spectrometer, as well as for data acquisition. The existing control system was not suited for the kind of observations intended for the polarization survey. Therefore, the entire backend control including software for the frontend and polarimeter control, as well as for the data acquisition needed to be rewritten.
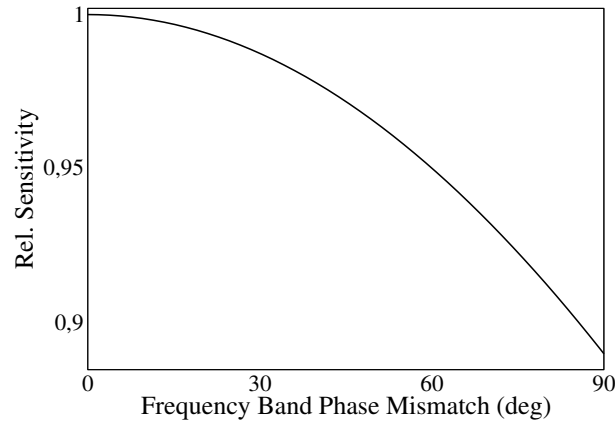
Figure 3.7: Calculation of the sensitivity loss for a linear phase gradient across the observing band. On the abscissa is plotted the phase difference between the band limits.

Table 3.2: Interface card specifications.

Manufacturer	National Instruments
Model	NI 6601
Number of counters	4
Counter size / number of bits	32
Number of digital I/O lines	32
Maximum source frequency	20 MHz

The available system utilizes two computers: an IBM 520 and a PDP 11/53. The actual telescope coordinates are transmitted by synchros from the antenna to the PDP 11/53, which, in turn, operates as an interface to the larger IBM 520. Spectroscopic observations can be scheduled and queued on the IBM 520 computer, which also controls the tracking and antenna positioning. The existing programs for scheduling and antenna control needed only minor modifications to be usable for continuum drift scans. Therefore, observations are planned and scheduled on the IBM 520, using these programs. The telescope position, local sidereal time (LST), wind speed, and observing status are transmitted via the local network (LAN) to another PC handling the data storage (Figure 3.8).

The analog polarimeter has four outputs, which are connected over several meters of coax cable to the data acquisition PC holding an interface card. Over such a distance the transmission of a frequency modulated signal (FM) is less susceptible to interference than that of an amplitude modulated signal (AM). Therefore, the output voltages are converted into a sine-wave signal with frequency proportional to the voltage of the correlation products (typically around 500 kHz) by a voltage to frequency converter. An adjacent analog-to-digital converter transforms the sine-wave into signals conforming to TTL logic, which can then be fed into the interface card.

The interface card consists of four counters and buffers. Its specifications are listed in Table 3.2. The counters are programmed to count the number of positive edges of the TTL signals send from the polarimeter. Such counters need an external gate signal to trigger the counting. This is provided by a low-frequency signal generator. At each positive edge of the TTL gate signal, count numbers are written into the buffer and counting is re-initiated. These count numbers are directly proportional to the correlation products. The frequency of the gate signal is 25 Hz, resulting in an integration time of 40 ms. After 200 integrations (8 s) the buffers are full. Read-out of the buffers and restarting the
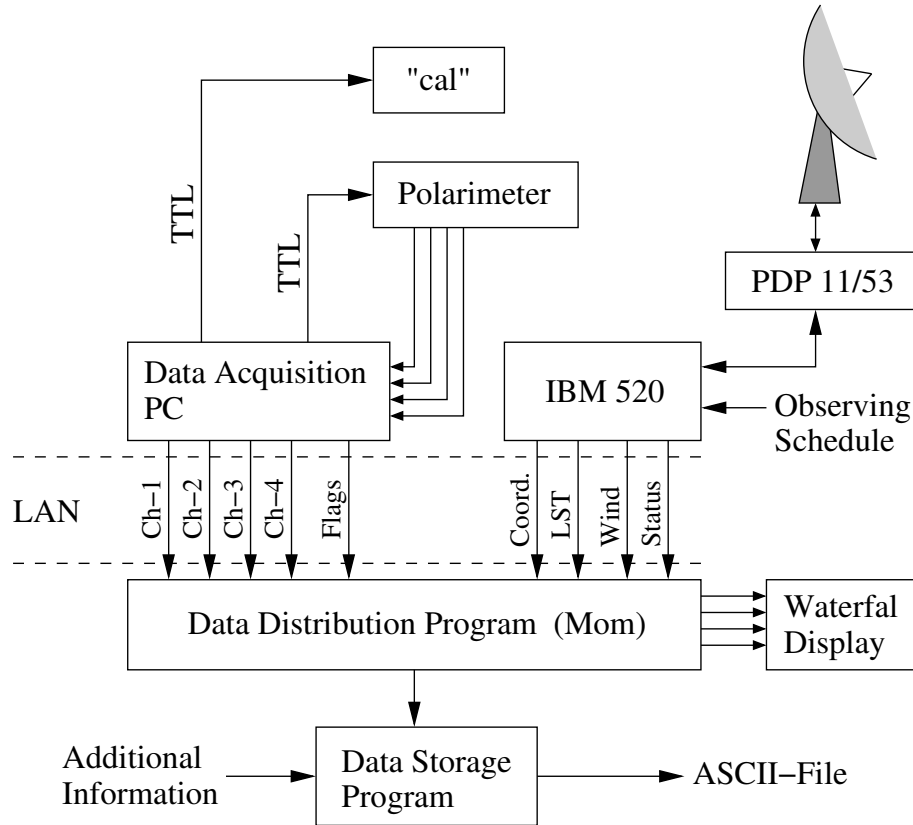
Figure 3.8: Flow diagram of the data stream as explained in the text.

counters requires about 400 ms. This results in cycles of roughly 8.4 s during which 4×200 packets of integrations are gathered and transmitted to the data storage PC.

The interface card is also equipped with digital I/O lines. These lines are used to control the noise source of the receiver and the internal $0/180°$-phase shifter of the polarimeter. During intervals of 200 integrations ($\sim$ 8 s), the phase shifter is set to $0°$ during the first half of the cycle ($\sim$ 4 s) and $180°$ during the second half ($\sim$ 4 s), resulting in 100 integrations at each phase. The noise source is switched every third cycle.

The data reduction is done later on separate PCs, involving different stages of data reading, processing, flagging and gridding. The data acquisition and most of the reduction and calibration tools described in the following sections are written in *glish*, a scripting language within the *AIPS++* (McMullin et al., 2004) environment. It was not possible to take advantage of the TOOLBOX package used at the Effelsberg 100-m telescope because of lacking detailed documentation.

3.2.1 Telescope Scheduling Software

The program used for scheduling of survey observations drives and holds the telescope at given coordinates. The telescope control software was not intended for drift scanning and tries to correct the telescope position after 60 minutes of observing. Therefore, drift scans are observed as sub scans with 57 minute lengths each.

Another problem with telescope positioning was encountered at declinations larger than 85°, probably because of limitations of the pointing model. Here, the telescope cannot be controlled by software but must be positioned manually.

3.2.2 Data Acquisition Software

On the data storage PC, data streams carrying information about the current telescope status, ongoing observations, telescope position, LST, and wind speed are continuously read-out by the data distribution program (Figure 3.9, top). This program merges the data on arrival and forwards them to the data storage program (Figure 3.9, bottom) in an appropriate format. In addition, the data are displayed for checking purposes on the "Waterfall Display" (Figure 3.10).

The data distribution program also corrects the telescope position sent from the IBM 520, because the telescope position is provided in equatorial coordinates in the current epoch. These coordinates must be transformed to J2000 coordinates. Additionally, the pointing model must be subtracted from these coordinates as the IBM 520 automatically applies the pointing correction.

Telescope-use prevented access to the system before July 2002. The data acquisition software, which therefore needed to be written prior to the completion of the hardware, had to be as flexible as possible. It was also not fully decided which observing modes will be available: whether, e.g. the telescope will be capable of observing maps, etc.

3.2.3 Data Reduction Program

The raw data must be processed before their quality can be examined. This is done by the data reduction program (DRP, Figure 3.11). This program reads the raw data, which are stored on disk in form of ASCII-files, and performs the following processing steps:

1. Removal of spikes and interference as explained in Section 4.1.1.

2. Separation of the different states of the internal phase switch and calibration signal, taking circuit times into account.

3. Calculation of the cross-correlation values by computing the difference of the signals of channel 3 and 4 at phase zero and 180° of the polarimeter (Equation 3.21).

4. Averaging packets of data of 4×200 integrations.

Any further reduction steps such as calibration, gridding, and interpolation will be described in Chapter 4. These data reduction steps are implemented by glish-scripts rather than graphical programs.

3.3 Instrumental Errors – Time-Invariable

The discussion in Section 3.1.6 demonstrated the point of relative gain and phase adjustments in the receiving system to maximize sensitivity and circularity of the response. Apart from errors due to gain and phase mismatches, the system components themselves may introduce errors such as cross-coupling or non-circular responses. These errors modify the initial Stokes parameters of the source and are most generally described by a 4×4 matrix, the Müller matrix. In this section the formalism used to describe these errors will be explained, roughly following Heiles et al. (2001) and Heiles (2002).
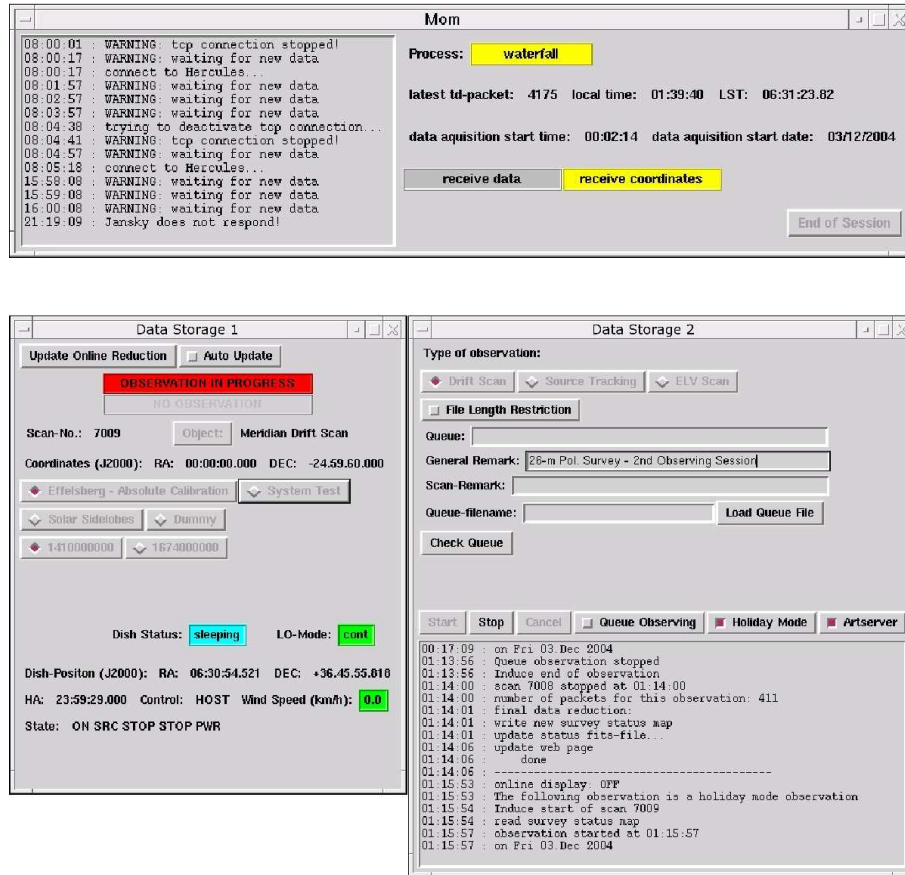
Figure 3.9: On the top a screenshot of the data distribution program (Mom) that receives and merges the incoming data streams from the polarimeter and the IBM 520 computer is displayed. This window shows only status information, except for the "End of Session" button to stop data acquisition. The data stream is visualized by yellow panels. The current sidereal and local times as well as status information are displayed. The two bottom screenshots show the data storage program (Data Storage 1 / 2) that receives, distributes and writes the raw data onto disk whenever the IBM 520 reports an observation. Additional information such as source name, project name, frequency and type of observation may be provided by the observer but are not mandatory to start an observation. All displayed messages are logged into a file.
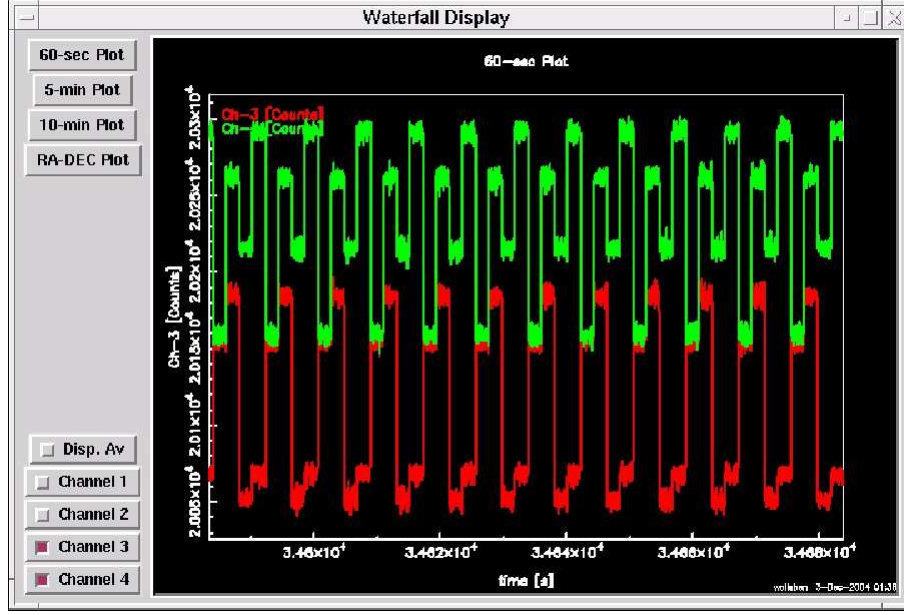
Figure 3.10: A screenshot of the Waterfall Display that plots the incoming data streams of all four channels in real-time. Here the display shows channel three and four, the sine and cosine channels of the polarimeter. Visible are the four phases of an integration: 1. phase zero, cal off; 2. phase zero, cal on; 3. phase 180°, cal on; 4. phase 180°, cal off. This display is very usefull for early recognition of problems with the system.

3.3.1 An Imperfect Feed

The feed is the first device of the receiver system that the signal from the source encounters. A perfect dual linear polarized feed uncouples two signals that are orthogonal, linear polarization components of the incoming wave. But feeds are usually designed for a certain bandwidth and their properties vary over this frequency band. Moreover, their outputs are only approximately linear or circular polarization components and are usually not perfectly orthogonal.

Here the case of a dual linear feed as used at the DRAO 26-m telescope is considered. Following Conway & Kronberg (1969) the imperfections of a feed are represented by a Jones matrix. Let $E = E_x + E_y$ be the analytic signal of the incoming wave. The feed output is then:

$$\begin{pmatrix} E_a \\ E_b \end{pmatrix}_{\text{out}} = \begin{pmatrix} 1 & \epsilon_1 e^{i\phi_1} \\ \epsilon_2 e^{-i\phi_2} & 1 \end{pmatrix} \begin{pmatrix} E_x \\ E_y \end{pmatrix}_{\text{in}} , \qquad (3.34)$$

with ϵ_1 and ϵ_2 representing the amplitude of cross coupling between the two polarizations, meaning that a small amount of one polarization component is received through the other, and vice versa. ϕ_1 and ϕ_2 are the phase angles of these coupled voltages. Depending on the errors the outputs can be arbitrary hands of polarization and are therefore denoted a and b.

The entries of the corresponding Müller matrix can be found by employing Appendix 8.2. Under the

Figure 3.11: The raw data reduction program that reads the raw data and does flagging, processing and gridding. The user can examine the data on different types of displays. Parameters for data flagging can be chosen and individual channels can be searched for interference. Data can be stored on disk in a space saving AIPS++ binary file format.

assumption that $\epsilon_1 \approx \epsilon_2 \approx 0$ the transformation of the original signal by the feed reads:

$$\begin{pmatrix} S_1 \\ S_2 \\ S_3 \\ S_4 \end{pmatrix}_{\text{out}} = \mathcal{M}_{\text{feed}} \begin{pmatrix} I \\ Q \\ U \\ V \end{pmatrix}_{\text{in}} \quad \text{with} \quad \mathcal{M}_{\text{feed}} = \begin{pmatrix} 1 & 0 & \alpha_f & \beta_f \\ 0 & 1 & \gamma_f & \delta_f \\ \alpha_f & -\gamma_f & 1 & 0 \\ \beta_f & -\delta_f & 0 & 1 \end{pmatrix}, \tag{3.35}$$

and

$$\begin{aligned} \alpha_f &= \epsilon_1 \cos\phi_1 + \epsilon_2 \cos\phi_2 \\ \beta_f &= \epsilon_1 \sin\phi_1 + \epsilon_2 \sin\phi_2 \\ \gamma_f &= \epsilon_1 \cos\phi_1 - \epsilon_2 \cos\phi_2 \\ \delta_f &= \epsilon_1 \sin\phi_1 - \epsilon_2 \sin\phi_2. \end{aligned} \tag{3.36}$$

The imperfections of a feed are described by four independent parameters to good approximation.

3.3.2 The Quadrature Hybrid

The quadrature hybrid forms the sum of two input signals while phase shifting one of the inputs. In a perfect hybrid the signal powers are split equally and the phase shift is exactly $90°$. Again, hybrids are designed for a specific frequency range and the perfect hybrid is achieved only to a certain degree.

In general, a hybrid can be described by the following Jones matrix:

$$\begin{pmatrix} E_a \\ E_b \end{pmatrix}_{\text{out}} = \begin{pmatrix} \sqrt{0.5} & g_{ya}e^{i\phi_{ya}} \\ g_{xb}e^{i\phi_{xb}} & \sqrt{0.5} \end{pmatrix} \begin{pmatrix} E_x \\ E_y \end{pmatrix}_{\text{in}}, \tag{3.37}$$

with $g_{ya} = g_{xb} = \sqrt{0.5}$ and $\phi_{ya} = \phi_{xb} = -90°$ for a perfect hybrid in which case E_a and E_b were right and left handed polarization components. Depending on the hybrid they do not have to be perfectly circular so they are denoted a and b.

Under the assumption that $g_{ya} \approx g_{xb} \approx \sqrt{0.5}$, the corresponding Müller matrix for the hybrid is:

$$\begin{pmatrix} S_1 \\ S_2 \\ S_3 \\ S_4 \end{pmatrix}_{\text{out}} = \mathcal{M}_{\text{hybrid}} \begin{pmatrix} I \\ Q \\ U \\ V \end{pmatrix}_{\text{in}} \quad \text{with} \quad \mathcal{M}_{\text{hybrid}} = \begin{pmatrix} 1 & 0 & \alpha_h & \beta_h \\ 0 & 0 & \gamma_h & \delta_h \\ \alpha_h & -\gamma_h & 1 & 0 \\ \beta_h & -\delta_h & 0 & 0 \end{pmatrix}, \tag{3.38}$$

with

$$\begin{aligned} \alpha_h &= \sqrt{0.5}\left(g_{ya}\cos\phi_{ya} + g_{xb}\cos\phi_{xb}\right) \\ \beta_h &= \sqrt{0.5}\left(-g_{ya}\sin\phi_{ya} + g_{xb}\sin\phi_{xb}\right) \\ \gamma_h &= \sqrt{0.5}\left(g_{ya}\cos\phi_{ya} - g_{xb}\cos\phi_{xb}\right) \\ \delta_h &= \sqrt{0.5}\left(-g_{ya}\sin\phi_{ya} - g_{xb}\sin\phi_{xb}\right). \end{aligned} \tag{3.39}$$

In case of a perfect hybrid the Stokes parameters S_1, S_2, S_3, and S_4 can be associated with Stokes I, $-V$, U, and $-Q$. Hence, the perfect hybrid – or a quarter-wave plate within the horn – only changes the order of Stokes parameters in the output vector.

3.3.3 System Gain

After being converted into approximate circular polarization components, the signals go through different amplifier chains. These chains have complex gains, causing different amplification and phase delays. The *system* gain therefore represents the time-independent signal deformation of the receiving

system. Unlike electronic gain, the system gain describes steady properties of the system devices and may only change by modification of the receiving system. The Jones matrix for the system gain is:

$$
\begin{pmatrix} E_x \\ E_y \end{pmatrix}_{\text{out}} = \begin{pmatrix} g_x e^{i\psi_x} & 0 \\ 0 & g_y e^{i\psi_y} \end{pmatrix} \begin{pmatrix} E_x \\ E_y \end{pmatrix}_{\text{in}},
\tag{3.40}
$$

with the voltage gains g_x and g_y and the phase delays ψ_x and ψ_y. The corresponding Müller matrix for the system gain is:

$$
\begin{pmatrix} S_1 \\ S_2 \\ S_3 \\ S_4 \end{pmatrix}_{\text{out}} = \mathcal{M}_{\text{amp}} \begin{pmatrix} I \\ Q \\ U \\ V \end{pmatrix}_{\text{in}},
\tag{3.41}
$$

with

$$
\mathcal{M}_{\text{amp}} = \begin{pmatrix} \frac{1}{2}\left(g_x^2 + g_y^2\right) & \frac{1}{2}\left(g_x^2 - g_y^2\right) & 0 & 0 \\ \frac{1}{2}\left(g_x^2 - g_y^2\right) & \frac{1}{2}\left(g_x^2 + g_y^2\right) & 0 & 0 \\ 0 & 0 & g_x g_y \cos \Delta\psi & -g_x g_y \sin \Delta\psi \\ 0 & 0 & g_x g_y \sin \Delta\psi & g_x g_y \cos \Delta\psi \end{pmatrix},
\tag{3.42}
$$

here $\Delta\psi = \psi_x - \psi_y$ can be considered a phase mismatch in the post-hybrid part which results in a 2×2 sub rotation-matrix in the Müller matrix.

3.3.4 The System Müller Matrix

In principle one can set up an individual Müller matrix for each component of the receiving system. The product of all matrices results in a matrix describing the entire system. The order in which these matrices must be applied corresponds to the signal path through the receiving system. Taking the above mentioned matrices as examples the transformation of the incoming signal is described by:

$$
\begin{pmatrix} S_1 \\ S_2 \\ S_3 \\ S_4 \end{pmatrix}_{\text{out}} = \mathcal{M}_{\text{amp}} \mathcal{M}_{\text{hybrid}} \mathcal{M}_{\text{feed}} \mathcal{M}_{\text{PA}} \begin{pmatrix} I \\ Q \\ U \\ V \end{pmatrix}_{\text{in}}.
\tag{3.43}
$$

In general, the matrix $\mathcal{M}_{\text{PA}}$ represents the rotation of the sky relative to the receiver coordinates and is a simple rotation matrix affecting only Stokes U_{in} and Q_{in}. This must only be taken into account for azimuthal mounted telescopes. In case of the DRAO 26-m telescope it is the unit matrix due to the equatorial mounting.

The system Müller matrix has 7 free parameters and an irrelevant phase. Algebraic multiplication of the individual matrices results in a far too complicated system matrix. This would be of no use for the calibration of the 26-m Survey, therefore the following form is used.

Assuming a uniform (perfect) system gain, which can be achieved by a pre-calibration, matrix multiplication gives the system Jones matrix taking only the feed and hybrid into account:

$$
\mathcal{J}_{\text{sys}} = \left(\begin{bmatrix} \sqrt{0.5} + g_{ya}\epsilon_2 e^{i(\phi_{ya}-\phi_2)} \\ g_{xb}e^{i\phi_{xb}} + \sqrt{0.5}\epsilon_2 e^{-i\phi_2} \end{bmatrix} \quad \begin{bmatrix} \sqrt{0.5}\epsilon_1 e^{i\phi_1} + g_{ya}e^{i\phi_{ya}} \\ \sqrt{0.5} + g_{xb}\epsilon_1 e^{i(\phi_{xb}+\phi_1)} \end{bmatrix} \right),
\tag{3.44}
$$

which results in the following Müller matrix:

$$
\mathcal{M}_{\text{sys}} = \begin{pmatrix} \left[1 + \alpha_f\alpha_h + \beta_f\beta_h\right] & \left[-\alpha_f\gamma_h - \beta_f\delta_h\right] & \alpha_f + \alpha_h & \beta_h \\ \left[\gamma_f\alpha_h + \delta_f\beta_h\right] & \left[-\gamma_f\gamma_h - \delta_f\delta_h\right] & \gamma_h + \gamma_f & \delta_h \\ \alpha_f + \alpha_h & -\gamma_h & \left[1 + \alpha_f\alpha_h - \gamma_f\gamma_h\right] & \left[\alpha_f\beta_h - \gamma_f\delta_h\right] \\ \beta_f + \beta_h & -\delta_h & \left[\beta_f\alpha_h - \delta_f\gamma_h\right] & \left[\beta_f\beta_h - \delta_f\delta_h\right] \end{pmatrix}.
\tag{3.45}
$$

This parameterized form will be usefull for the analysis of the system matrix of the DRAO 26-m telescope, later in Section 4.3.1.

3.3.5 Deriving the System Müller Matrix

In practise, it is often impossible to determine the system Müller matrix accurately by theoretical computation. Instead, the matrix must be determined by calibration. For the calibration of the 26-m Survey not the parameterized form of the system matrix (Equation 3.45) is used but the matrix entries itself are found. This can be achieved by least-square fitting, for example, if reference values exist and system noise has been removed. If the data still contain system noise more advanced fitting algorithms must be applied.

If the matrix entries can be found by least-square fitting, the coefficients m_{XX} of the following set of m equations corresponding to reference values $n = 1, 2, \ldots, m$ must be determined:

$$
\begin{aligned}
I_{\text{obs},n} &= m_{\text{II}}I_{\text{ref},n} &+& \quad m_{\text{IV}}V_{\text{ref},n} &+& \quad m_{\text{IU}}U_{\text{ref},n} &+& \quad m_{\text{IQ}}Q_{\text{ref},n} \\
V_{\text{obs},n} &= m_{\text{VI}}I_{\text{ref},n} &+& \quad m_{\text{VV}}V_{\text{ref},n} &+& \quad m_{\text{VU}}U_{\text{ref},n} &+& \quad m_{\text{VQ}}Q_{\text{ref},n} \\
U_{\text{obs},n} &= m_{\text{UI}}I_{\text{ref},n} &+& \quad m_{\text{UV}}V_{\text{ref},n} &+& \quad m_{\text{UU}}U_{\text{ref},n} &+& \quad m_{\text{UQ}}Q_{\text{ref},n} \\
Q_{\text{obs},n} &= m_{\text{QI}}I_{\text{ref},n} &+& \quad m_{\text{QV}}V_{\text{ref},n} &+& \quad m_{\text{QU}}U_{\text{ref},n} &+& \quad m_{\text{QQ}}Q_{\text{ref},n},
\end{aligned}
\tag{3.46}
$$

with "obs" referring to observed Stokes parameters and "ref" to the reference values, taken from catalogues of standard calibration sources, for example.

If the data still contain system noise the observed Stokes parameters cannot be compared with standard values. In this case, iterative algorithms may be applied to approximately remove system noise and find the system matrix. For the 26-m Survey, the system matrix is found in two iterative steps: a "pre-calibration" and a "second calibration".

The Jones and Müller matrices describe linear cross-coupling of voltages and powers, respectively. Usually, instrumental errors are sufficiently described by first-order terms of cross-coupling.

3.3.6 The Response Pattern

The response or diffraction pattern is the fingerprint of a telescope. A telescope's response pattern is described by diffraction theory. Briefly, in total power the angular pattern of the beam is the Fourier transform of the electric field distribution across the aperture. At the DRAO 26-m telescope, the aperture is blocked by three support struts and the receiver box in the projected centre of the surface. The legs produce a series of diffraction cones in the response pattern, whereas the receiver blockade produces the circular side lobes. Irregularities of the antenna surface make the side lobe structure more complicated. The response pattern of the DRAO 26-m telescope in total power at 1.4 GHz has been measured by Higgs & Tapping (2000). Notable side lobe structure was detected as far as 45° off the main beam at a level of −49 dB.

Calculations show that these side lobes usually produce high instrumental polarization (Landecker, priv. comm.). This means that an initially *unpolarized* source will be detected as *polarized* if received through the side lobes. While the correction for main beam instrumental polarization is relatively
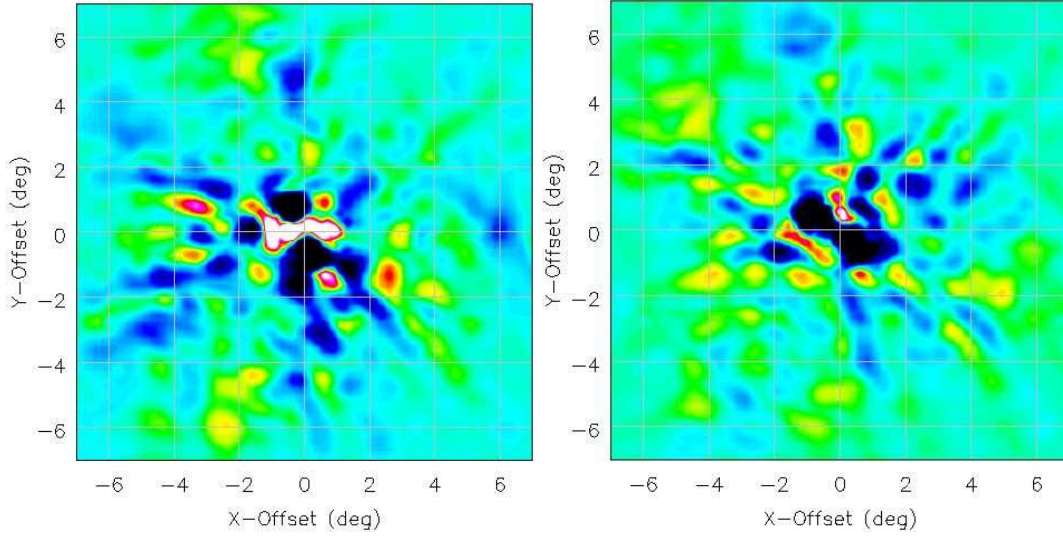
Figure 3.12: The response pattern of the DRAO 26-m telescope observed with a digital backend with 4 MHz bandwidth, centred at 1.42 GHz, using the Sun as unpolarized source. Shown is the received amplitude in the two cross-correlation channels RL (left) and LR (right) on linear scale. Although the maps are not calibrated, the extent and complicated structure of the response pattern can be seen. The total observing time spend for these observations was 60 hours.

straightforward, the correction of side lobe polarization is much more difficult. This requires the exact knowledge of the response pattern in Stokes U and Q as well as fully sampled total power maps for the deconvolution in the image plane.

For checking purposes the response pattern of the DRAO 26-m telescope has been measured within a $15° \times 15°$ area centred at the Sun. The radiation of the Sun is generally unpolarized at 1.4 GHz and its equivalent brightness temperature observed with this telescope is about $200,000$ K. The Sun is extended with a diameter of roughly $35'$ at 1.4 GHz. Its flux is not constant and can vary due to solar activity, which must be taken into account for side-lobe mapping. Figure 3.12 shows the measured response pattern for the two cross-correlation channels. The percentage polarization outside the main beam varies from -3.3% to 4.3% in Stokes U, and -2.5% to 1.7% in Stokes Q.

A correction of the 26-m Survey for side lobe polarization is not intended because of the following reasons: First, the sampling of the total power map of the survey is not sufficient to allow deconvolution of the polarization maps with the response pattern. Second, only strong, compact sources may cause measurable instrumental polarization through the side lobes. The brightness temperature of the diffuse total power emission is comparably lower and is received through a large area around the main beam, partially cancling out the instrumental polarization components of the side lobe structure.

3.4 Instrumental Errors – Time-Variable

In this section time-variable errors will be discussed. These errors are mainly introduced by the active receiver components, but also by variations of the ambient temperature, which may cause changes in the IF path length and thus affect the relative phase of the IF signals. A calibration signal is injected to detect and correct these as *electronic* gain denoted errors.

3.4.1 Electronic Gain

The two hands of polarization are amplified by the LNAs, one LNA for each hand. But amplifiers are not perfectly stable; their gain varies in a random fashion. Moreover, amplifiers introduce a phase delay, which, if unstable, results in relative phase fluctuations between the E_r and E_l polarization components. Relative gain and phase variations in the post-hybrid part affect the cross-correlation (Section 3.1.6). Therefore, variations of the complex electronic gain must be corrected.

The amplitude and phase of the polarized reference signal (cal) is measured with the polarimeter. The cal is detected "on top" of the sky and system noise: $RL = RL_{system} + RL_{sky} + RL_{cal}$ and $LR = LR_{system} + LR_{sky} + LR_{cal}$. In polarization, the reference signal is a vector whose components, RL_{cal} and LR_{cal}, must be derived by subtraction of sky and system noise. This is done by subtracting the mean of 5 integrations that precede and follow each cycle of cal-signal injection. The resulting values for RL_{cal} and LR_{cal} give instantaneous polarized intensity and polarization angle of the cal and thus the current electronic gain of the receiver. The correction of the raw data is then done by referring the observed polarized intensities and angles to the reference signal.

The cal is detected after passing through the receiving system, just as the sky signal. Thus, it suffers from the same time-invariable errors as the sky signal, except for errors caused by the feed and antenna. This, however, means that the *absolute* polarized intensity and angle of the cal may be wrong but it still correctly traces electronic gain variations.

The order of application of these corrections is important! Corresponding to the path of the signal through the receiving system, raw data must first be corrected for electronic gain and then for the system Müller matrix.

3.5 Other Errors

In this section a summary of errors is discussed that do not fit into the above scheme. Such errors are ionospheric Faraday rotation, which is negligible for night-time observations at 1.4 GHz but may be strong shortly before sunrise and after sunset. But interference of solar or terrestrial radiation as well as weather changes can also cause problems.

3.5.1 Ionospheric Effects

The ionosphere adjoins the Earth's mesosphere at a height of roughly 80 km. Within the F1- and F2-layer of the ionosphere solar UV radiation detaches electrons from atmospheric atoms. In combination with the Earth's magnetic field these free electrons give rise to Faraday rotation. The amount of free electrons, and thus the rotation measure, depends on solar activity, time of the day, and geographic location of the telescope.

Other possible ionospheric effects at 21 cm wavelength are refraction and damping of radio waves. The free electrons are set into vibration by the electromagnetic field and lose energy borrowed from the field by collisions with atoms or ions. The errors caused by refraction and damping are negligible at that wavelength.

Although survey observations took place almost at the maximum of the solar activity cycle 22, no evidence for any such effects are found during night when the total electron content of the ionosphere (TEC) is small and ionospheric Faraday rotation is low. However, some of the day-time observations show rapid changes of the polarization angle, which are not confirmed by neighboring drift scans. These data are manually flagged and rejected. With the DRAO synthesis telescope, Faraday rotation of up to $10°$ is observed at solar maximum and as much as $5°$ at solar minimum, both during day time. At night, values between zero and $5°$ are observed (A. Gray, priv. comm.).
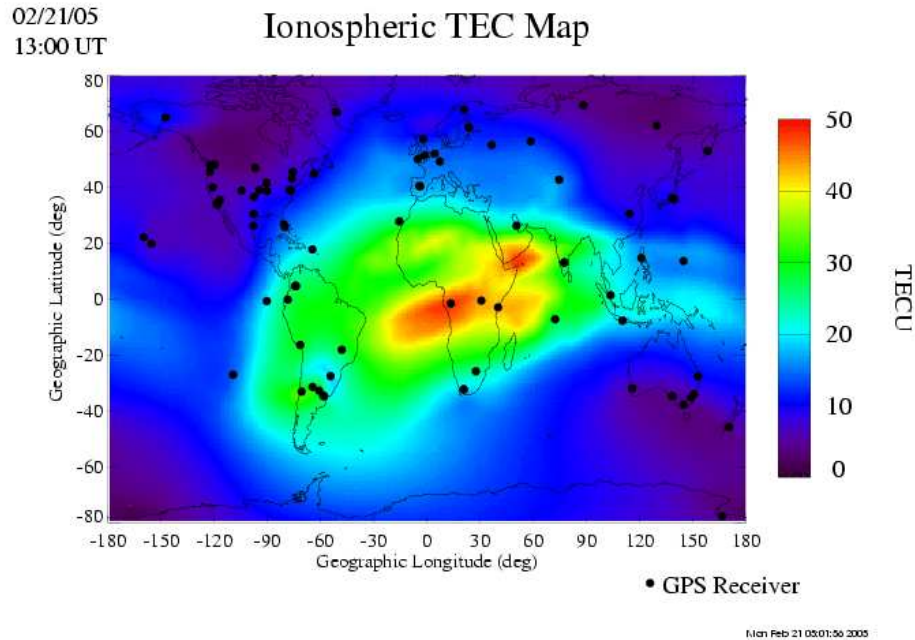
Figure 3.13: Example map of the TEC from February 21, 2005 demonstrating the distribution of electrons in the ionosphere during night in Canada. The map is taken from http://iono.jpl.nasa.gov/.

Presently, the capabilities for a prediction and correction of these effects are limited. Although ionospheric effects are negligible in the survey data, two approaches for the correction of ionospheric Faraday rotation are mentioned here. These are the theoretical modelling of the ionosphere and the direct measurement of the electron content.

Campbell (1999) has suggested a prediction of ionospheric Faraday rotation by using the Parameterized Ionospheric Model (PIM). The PIM is a theoretical model of the global ionospheric climatology, developed at USAF Phillips Laboratory. Originally, PIM was intended to calculate the TEC of the atmosphere. A variant of PIM, initially motivated for application to VLBI astrometry (PIMVLBI), includes routines to calculate $B_\parallel$ and $B_\perp$ of the Earth's magnetic field for a given line-of-sight. The usefullness of PIM and PIMVLBI for the correction of polarization data is rather limited because it is a static model that is not intended for generating time-series of ionospheric conditions. Moreover, it often fails to predict the right trend late in the day. At DRAO, another model is under development based on Chapman layers using the solar flux at 10.7 cm as input. Initial versions seem promising, predicting trends correctly where PIM fails (A. Gray, K. Tapping, priv. comm.).

The other approach requires a GPS (Global Positioning System) receiver installed at the telescope site. With such a receiver the TEC can be monitored for the local site. By measurement of the time delay of the GPS signals, the ionospheric-induced delay and hence the TEC along the line-of-sight to each visible satellite can be determined. In conjunction with an ionospheric model this method makes an accurate correction possible. Tests at the VLA have shown that the accuracy is sufficient to correct for Faraday effects to $\lesssim 2°$ at 327 MHz (Erickson et al., 2001).

3.5.2 Miscellaneous

Rather rarely occurring errors encountered during survey observations are the following:

- Solar interference: If observations are done at day-time, solar radiation may be received through the side lobes and interfere with the main beam signal. Solar interference can be avoided by not planning observations within a radius of several tens of degrees around the Sun.

- Radio-frequency interference: Interference with terrestrial signals can often not be avoided but must be recognized and flagged out by software processing. By selecting a protected frequency band, RFI can be minimized.

- Weather changes: Wind and snowfall can affect the data by pushing the antenna and changing the pointing. In addition, snow and rain changes reflectivity of ground and antenna and thus affect the system temperature. The correct pointing of the telescope must be checked and unusual system temperature drifts detected during data reduction.

- Hard- and software modifications: During the survey observations, improvements of hard- and software were frequently made. This can change properties of the system. This must be taken into account during data reduction.

3.6 Observing

The effects of the main contribution to the antenna temperature – stray and ground radiation – can be minimized by drift scanning. By restricting observations to night-time, solar interference and errors due to ionospheric Faraday rotation are also minimized. In the following, the origin and characteristics of ground radiation will be discussed, the observing strategy explained and observations summarized.

3.6.1 Ground Radiation

Ground radiation is received through the side and back lobes, and raises the antenna temperature and hence the system temperature. Investigations of Mezger (in Altenhoff et al., 1960) showed that at centimetre wavelengths rough and dry ground behaves like a black body of approximately ambient temperature. Deviations from a black body were found for smooth water and metal surfaces, as well as for asphalt and concrete. If the surface is smooth compared to the observing wavelength it reflects emission from the sky and thus has a brightness temperature of a few Kelvin.

Ground radiation is expected to be time variable. Seasonal variations of the ground temperature on time scales of months or weeks, as well as on time scales of days and hours, because of day-night variations of the ambient temperature, are possible. Environmental parameters influence the ground radiation. The ground cools down in the winter and after sunset, and rain changes the emission and reflection coefficients of the ground. The ground-reflected signal depends on siderial time while drift scanning the sky.

The following definitions are useful for the estimate of ground radiation offsets in total power (e.g. Kraus, 1966). The stray factor β of a telescope expresses the fraction of radiation received through the side lobes if the telescope is uniformly illuminated. The radiative efficiency or ohmic-loss factor η_R reflects the effects of ohmic losses in the feed and on the antenna surface. These factors are $\eta_R = 0.995$ and $\beta = 0.26$ (Higgs & Tapping, 2000) for the DRAO 26-m telescope

If the antenna is pointed (horizontally) to the horizon, half of its side lobes receive radiation from the ground while the other half and the main lobe see the atmosphere (see Figure 3.14). In this case, the
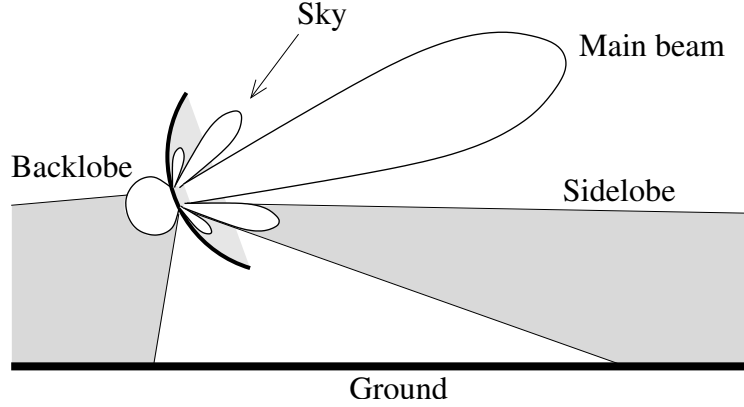
Figure 3.14: Ground radiation is received through the side and back lobes of the antenna.

side lobe contribution to the ground offset in total power is $\eta_R \beta (T_{amb} + T_{atm})/2 \approx 41$ K at an ambient temperature of $T_{amb} = 300$ K and an atmospheric temperature of $T_{atm} = 16$ K.

If the telescope is pointed (vertically) to the zenith, only the back lobes receive ground radiation (see Figure 3.14). Usually, the back lobes have a very low gain but fill the whole hemisphere of 2π steradians. Assuming that 10% of the total side lobe emission is received through the back lobes, the side lobe contribution to the ground offsets for the vertically adjusted antenna is $(0.1\,T_{amb} + 0.9\,T_{atm})\eta_R\beta \approx 12$ K.

The spillover efficiency η_{spo} describes how good the feed illuminates the reflector surface. The DRAO 26-m telescope has a spillover efficiency of 0.95 (Higgs & Tapping, 2000). For a horizontally adjusted telescope half of the spillover signal is received from the atmosphere and half from the ground. This results in a contribution of spillover noise to the ground offset in total power of $\eta_R(1 - \eta_{spo})(T_{amb} + T_{atm})/2 \approx 8$ K. If the telescope is pointed to the Zenith only the ground contributes to the spillover signal with $\eta_R(1 - \eta_{spo})\,T_{amb} \approx 15$ K.

This can already explain roughly the observed ground offsets at the DRAO 26-m telescope in total power. These profiles show that the ground offset is highest for the horizontal telescope. It is about 15 K lower for the vertical telescope. The estimated ground radiation offsets at $0°$ and $90°$ elevation are 49 K, and 27 K, respectively. The relative variation in total power is of the order of 20 K, which is in reasonable agreement with the actually observed profiles.

Another estimate shows the effect of seasonal variation of the ambient temperature. Assuming a difference of the ambient temperature of 30 K between summer and winter, the corresponding change of the ground radiation offset is about 4 K during the night for the horizontal telescope, and about 2 K for the vertical telescope. As somewhat smaller temperature variations also occur between day and night, the variation of the ground offset on time scales of hours can be of the order of 1 K, depending on the ambient temperature drift during the observation.

The degree of instrumental polarization of the side lobes can exceed the main lobe instrumental polarization by several percent. This means that – even if unpolarized – the ground radiation causes ground offsets in Stokes U and Q in the same way as in total power. On the basis of the measurements made for this survey it is impossible to judge how much the ground radiation itself is polarized, or whether the relevant side lobes are polarized.

Modeling ground radiation is difficult. The response pattern is influenced by surface deformations and defects in the optical path. These effects usually cannot be calculated with high precision. Even if the response pattern is measured for a telescope, the ground radiation depends, in a more or less unpredictable way, on weather and the surrounding landscape. However, attempts of rough modelling

Table 3.3: Survey specifications

Integration time per pixel	$\frac{1}{\cos\delta}$ 60 s
Observing period	November 2002 - May 2003
Average error	30 mK
Declination range	$-27°$ to $90°$

in total power have been made by e.g.: Altenhoff et al. (1960), Higgs (1967), and Brouw & Spoelstra (1976).

3.6.2 Observing Strategy

To avoid mixing of ground radiation and large-scale sky-emission, observing is done by drift scanning the sky with the telescope stationary at the Meridian. This keeps the azimuth and elevation depended component of the ground radiation constant. Each night, a fixed declination between $-27°$ and $+90°$ is observed. The order of declinations is random, to avoid systematic effects. Declinations are first selected from a grid with $5°$ steps in declination, later from a grid with $2.5°$.

Ground radiation profiles for all Stokes parameters are required to subtract ground offsets from the drift scans and extrapolate the zero-levels in Stokes U and Q below zero declination. These profiles are measured by sweeping the telescope between $-27°$ and $+90°$ declination along the Meridian. A series of elevation scans must be made at different sidereal times to eliminate sky emission.

The northern celestial pole (NCP) has often been used as a reference and calibration point in polarization surveys. For calibration purposes, the NCP is occasionally observed by drift scanning. The diffuse emission at the pole is moderately polarized and the NCP can be used to check the receiver response. During a 12 hours observation the polarization vector performs a full rotation on the sky, which should result in a uniform cycle in the Stokes U-Q plane with radius corresponding to the polarized intensity of the NCP.

Although the angular resolution of the telescope is not sufficient to use maps of polarized compact sources for calibration, maps of standard calibrators – polarized and unpolarized – are made prior and after each drift scan for pointing checks.

The survey specifications are listed in Table 3.3. In summary, the following observations were made:

- The survey drift-scans were made during 168 nights from November 2002 through May 2003. Table 3.4 gives a summarized observing log. A drift scan was started when the sun was below $15°$ elevation and stopped 1-2 hours after sunrise. A coverage of 21.7% of the sky observable from DRAO on a grid of $15'$ cell size could be achieved.

- Elevation scans were made every 2 - 3 months. A complete elevation scan took 1.5 h with a scanning speed of $1.3°$/min. Table 3.5 gives direction and observing dates in local and sidereal time of elevation scans used for the calibration.

- Two NCP scans were made. An analysis of these scans is given in Section 4.3.2.

- Standard calibrators were mapped to check the pointing. No pointing problems were noted.

- Occasionally, drift scans were repeated for system checks.

Table 3.4: Summarized listing of survey drift scans.

Month	Declination (°)	Comment
Oct. 2002	60, 65	10 MHz bandpass filters
Nov. 2002	70, 75, 80, -25, -20, -15, -10 -5, 0, 5, 10, 15, 20, 25, 30, 35 40, -25, 45, 50, 55, -22.5, -17.5	10 MHz bandpass filters and software problems
Dec. 2002	-12.5, -10, 3.5, 8.5, 13.5, 18.5 22.5, 27.5, 32.5, 37.5, 42.5, 47.5 52.5	Power failures
Jan. 2003	57.5, 62.5, 67.5, 72.5, 77.5, -7.5 -2.5, 2.5, 7, 12, 17, -20, -12.5 -7.5, -5, 50, 75, 41, -24, 46, -12.5 -15, 51, -19, 56, -14, 10, 40, 20 60, 30	Periods of snow
Feb. 2003	79, 1, 59, 21, -11, 71, -4, -6, -9 69, 76, 26, 24, 29, 31, 34, 36, 39 -1, -16	Software and hardware modifications
Mar. 2003	64, 66, 70, 6, -21, 16, -25, -11, 6 44, 49, 54, 60, 11, 19, 2, 37, 28,74 -2, 23, 13.5, 33, -8, -7, 61.5, 53, -18	Some snow
Apr. 2003	77, 43, 48, -13, 4, 47, 72, 13, 14 8, 9, 58, 68, 65, 15, 5, 0, 35, -22 57, 38, 61, -3, 85, 25, 45, 52, 18	
May 2003	-17, 22, 41.5, 63, -9.5, -12, -4.5 -20.5, 27, -19.5, 32, 17.5, 6.5, -14.5 -23, 54.5, 11.5, -6, 59.75, -26, -27 -28, -29	

Table 3.5: Observing dates of the elevation scans used for the determination of ground radiation profiles.

Date	LT	LST	Direction
Dec 12, 2002	18:18	23:36	down
	19:26	0:52	up
	21:00	2:27	down
	22:37	4:05	up

4 Data Processing and Absolute Calibration

The data reduction results in Stokes U and Q maps of the northern sky, showing the distribution and strength of polarized emission at 1.4 GHz. To transform the observed correlation products into Stokes parameters a calibration is required. The data are then averaged and gridded for scientific analysis. This chapter describes the data reduction steps. A detailed error analysis is presented at the end of this chapter.

4.1 Reduction Chain

After having discussed the different system adjustments, error sources, and observing methods in the previous chapter, this chapter gives a detailed description of the data processing and calibration steps – the data reduction. The first processing steps are done with the Data Reduction Program described in Section 3.2.3, for most of the other reduction steps individual glish-scripts are written. A flow diagram illustrating the different stages of data reduction is shown in Figure 4.1.

Three additional surveys for the absolute calibration of the raw data are utilized. The 1.42 GHz Stockert 25-m Survey (Reich & Reich, 1986; Reich, 1982) is used for the calibration of the total power data, the LDS serves as reference for the calibration of the instrumental response and provides zero-levels in Stokes U and Q, and data from the EMLS made with the Effelsberg 100-m telescope are used to adjust the Stokes U and Q intensity scales. The resolution and sensitivity of the first two surveys is comparable with the 26-m Survey, whereas the EMLS has a higher angular resolution and better sensitivity.

4.1.1 Radio Frequency Interference Flagging

The first reduction step is the flagging of data corrupted by RFI. Flagging in this context means that data affected by RFI are "marked" by a search routine and excluded from further data processing. The enormous amount of data does not allow a visual – by hand – flagging, instead, an automated flagging routine is developed.

RFI is mainly generated by terrestrial radio transmitters, radar, or locally operating devices, which may produce a spectrum of harmonic lines. Satellites, although supposed to transmit outside the protected band from $1,400$ to $1,427$ MHz, may also generate RFI in the protected band. Even if transmitting at frequencies outside the observing band, strong radio transmitters can push the LNAs into saturation and thus affect the system gain. Figure 4.2 shows an extreme RFI event several seconds of duration. Most of the observed RFI is shorter in time and usually only a few integrations (between ~ 1 and ~ 10) are affected.

The remote observatory site is surrounded by mountains which block the terrestrial RFI to some extent. In addition, the institute buildings are screened by a Faraday cage, which reduces most of the RFI caused by local computers and backend devices. Therefore, the DRAO provides ideal conditions for radio observations in the L-band. In fact, only 0.1% of the total observing time is lost due to
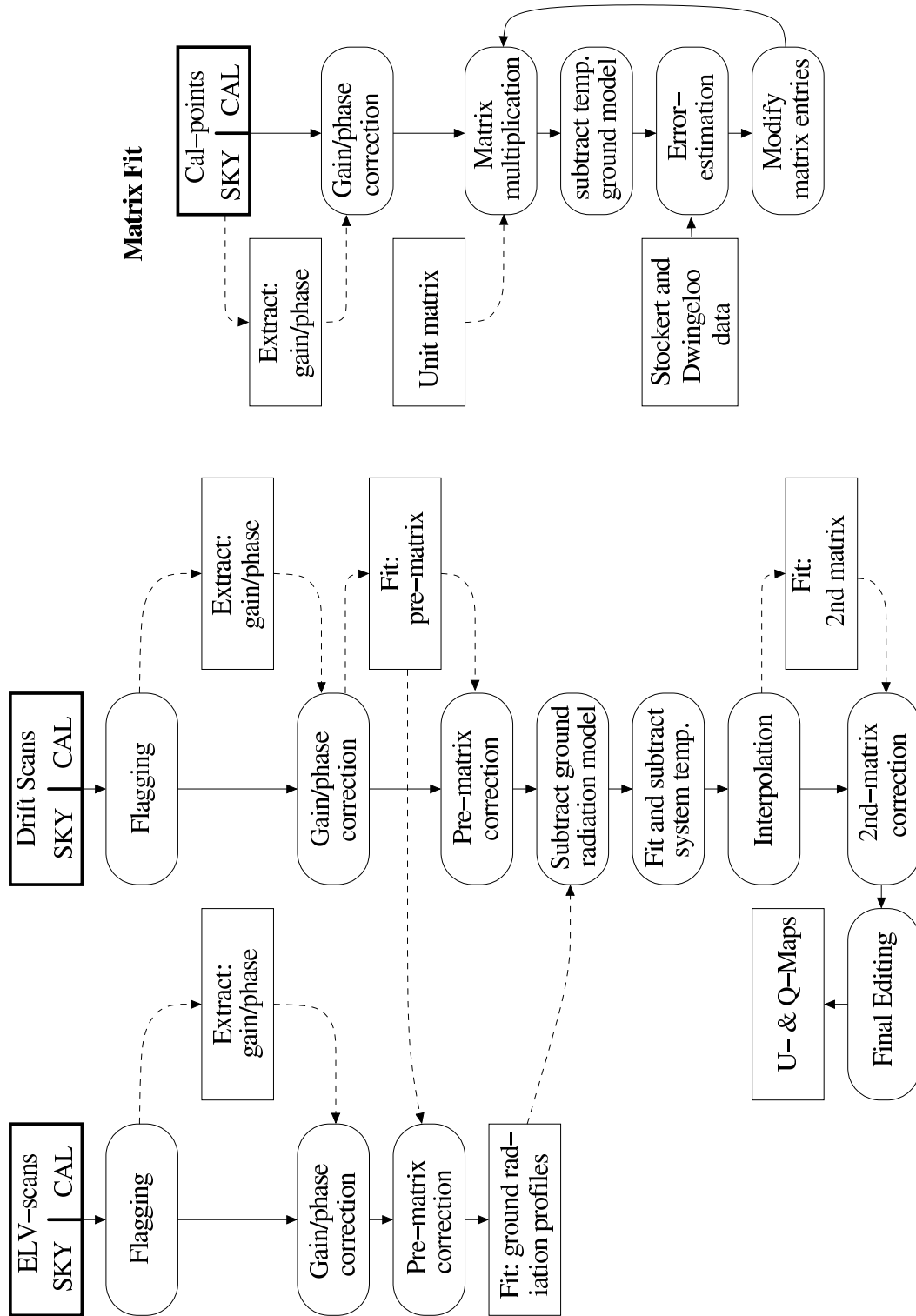
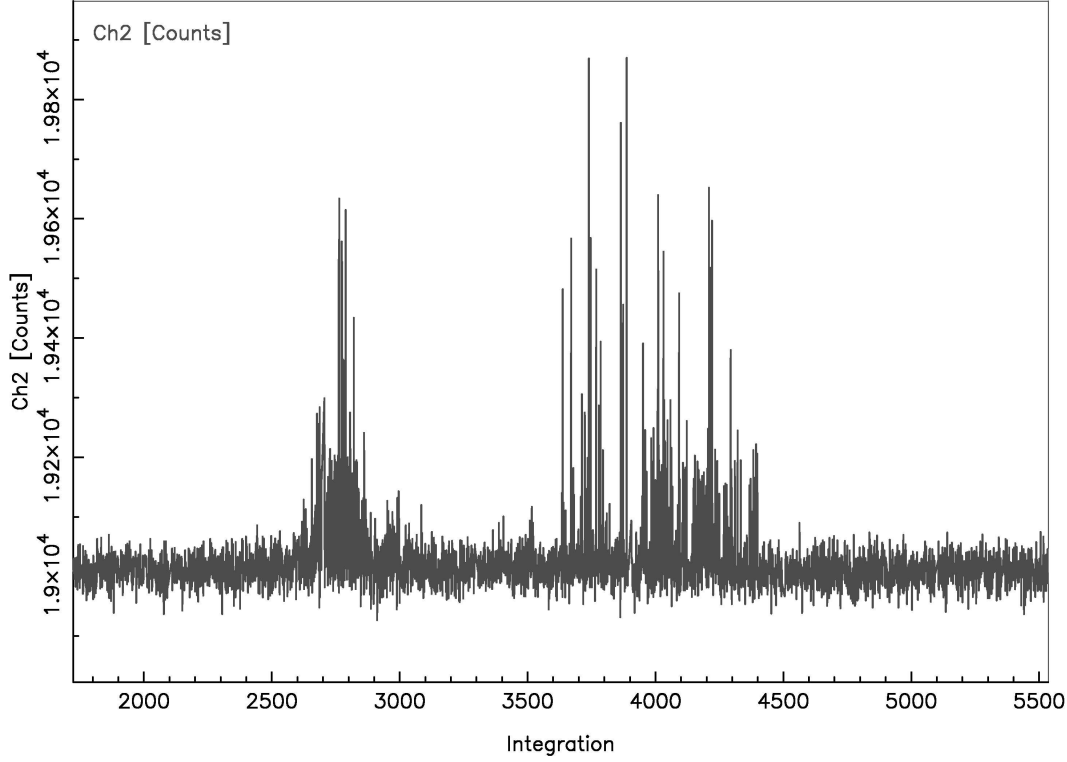**Matrix Fit**

Figure 4.1: Reduction chain

Figure 4.2: An example for RFI in one of the total power channels. The width of the plot is 150 s, the amplitude of the strongest peaks is roughly 8 K.

interference. Some RFI could be observed at the beginning and end of working hours, most likely caused by automotive electronics or ignition of engines.

The RFI flagging is implemented in the Data Reduction Program (DRP). Interferences are detected by an algorithm that searches for short-term peaks separately in all four channels. The search is performed within a two minute time window, which is moved along the time-axis of the raw data. Integrations with signal levels higher than $4.5\,\sigma_{\mathrm{rms}}$ above the average signal level in one or more channels within the window are flagged. RFI flagging is done twice and all four channels of flagged integrations are removed from further data processing.

An automatic flagging routine always requires a trade-off of the search parameters to enable safe detection of RFI while leaving sky emission untouched. The parameters used here have been tested and result in good identification of short-term RFI. Possible long-lasting interference must be flagged in the map at a later reduction stage.

4.1.2 Assorting the Raw Data

First, pure correlation products are derived by calculating differences of the two polarimeter-phases (0/180°) for each channel, averaged over 100 integration (Equation 3.21). This is done by the DRP.

Then, the raw data are arranged in bins, one for each observing month. This allows to check for time-variability of the instrumental response. Second, the calibration signals are extracted from the raw data and fitted by least-square fitting. The electronic gain is found to change slowly, which permits fitting of first order polynomials over 1 hour intervals, the typical subscan length.

Implemented in the sorting script is a checking routine for the telescope position. Observations were usually done unattended and accidental telescope movements due to snow or wind may not be recognized. Therefore, the hour angle and declination of each scan is checked and observations are flagged out if necessary.

Additional observations such as elevation scans, NCP measurements, and maps require a somewhat different procedure. Elevation scans, for example, require higher order polynomial fits of the extracted calibration signals, because the receiver shows an elevation-dependend gain. Moreover, the coordinates of manually performed observations, such as NCP scans, must be derived from the LST recordings, because the coordinates provided by the telescope control system are wrong in that case.

4.1.3 Electronic Gain

The cal signal is periodically injected into the signal path and is used to track electronic gain fluctuations. The intrinsic polarized intensity $PI_{standard}$ and polarization angle $PA_{standard}$ of the cal is assumed constant over the observing term. Hence, variations of the *measured* polarized intensity PI_{cal} and polarization angle PA_{cal} of the cal must be interpreted as gain and phase drifts within the receiver.

With the separated sky and fitted cal signals the data can be corrected for electronic gain fluctuations. The total power channels are multiplied with the reciprocal of the measured cal signal strengths and the polarization channels are rotated and normalized according to PI_{cal} and PA_{cal}:

$$
\begin{aligned}
\mathrm{RR}'_{sky} &= \mathrm{RR}_{sky}/\mathrm{RR}_{cal} \\
\mathrm{LL}'_{sky} &= \mathrm{LL}_{sky}/\mathrm{LL}_{cal} \\
\mathrm{RL}'_{sky} &= \left(\mathrm{RL}_{sky}\ \cos 2PA_{cal} - \mathrm{LR}_{sky}\ \sin 2PA_{cal}\right)/PI_{cal} \\
\mathrm{LR}'_{sky} &= \left(\mathrm{LR}_{sky}\ \cos 2PA_{cal} + \mathrm{RL}_{sky}\ \sin 2PA_{cal}\right)/PI_{cal}.
\end{aligned}
\tag{4.1}
$$

RR_{cal} and LL_{cal} are the measured strength of the cal in total power and RL_{cal} and LR_{cal} the amplitudes in the sine- and cosine-channel. Polarized intensity and angle of the cal are given by $PI_{cal} = \left(\mathrm{RL}_{cal}^2 + \mathrm{LR}_{cal}^2\right)^{0.5}$ and $PA_{cal} = 0.5 \arctan\left(\frac{\mathrm{RL}_{cal}}{\mathrm{LR}_{cal}}\right)$.

Although the precise strength and polarization angle of the noise source is unknown and not relevant at this point, a rough estimate of $PI_{standard}$ and $PA_{standard}$ can be derived by applying the matrices 4.5 and 4.6 to the measured values. By this, the cal signal is found to have the following approximate strength:

$$
\begin{aligned}
< PI_{standard} > &= 41\ \mathrm{K} \\
< PA_{standard} > &= 71°,
\end{aligned}
\tag{4.2}
$$

with the polarization angle given in the RA-DEC coordinate system.

Because of the intensity of the noise source, all integrations with the cal signal switched on are used only for the determination of the electronic gain and are excluded from further data processing. This means that the noise source injection reduces the effective observing time. Therefore a trade-off at the beginning of the observing run was made: 1.7% of the total observing time is used for system calibration.

4.1.4 Pre-Calibration

The polarimeter provides outputs that are proportional to the two auto- and cross-correlations of the R and L-signals: RR, LL, RL, and LR. The intention of the pre-calibration is to convert the arbitrary scale-unit of the polarimeter outputs (counts) into a temperature scale. The total power channels (RR, LL) are calibrated to approximate brightness temperature and the cross-correlations (RL, LR) are scaled

and rotated to roughly express Stokes U and Q measured in Kelvin. This step does not include any correction of instrumental errors such as instrumental cross-talk.

The polarimeter output channels form a 4-vector. Scaling and rotation of this vector is computed by multiplication with a 4×4-matrix, the pre-calibration matrix. The entries on the main diagonal of this matrix are mere scaling factors, whereas the 2×2-submatrix causes a rotation of RL and LR. The other entries are zero. The computation of the pre-calibration matrix is done in an intermediate step by iterative fitting.

Iterative Determination of the Pre-Calibration Matrix

The Stockert Survey (Stokes I) is calibrated in full-beam brightness temperature, which must be converted into main-beam brightness temperature, whereas the LDS gives Stokes U and Q brightness temperatures. The reference values for the computation of the pre-calibration matrix are given by:

$$
\begin{aligned}
\mathrm{RR}_{\mathrm{ref}} &= (0.5 \cdot 1.55\,(I_{\mathrm{Stockert}} - 2.8\,\mathrm{K})) + 2.8\,\mathrm{K} \\
\mathrm{LL}_{\mathrm{ref}} &= (0.5 \cdot 1.55\,(I_{\mathrm{Stockert}} - 2.8\,\mathrm{K})) + 2.8\,\mathrm{K} \\
\mathrm{RL}_{\mathrm{ref}} &= U_{\mathrm{LDS}} \\
\mathrm{LR}_{\mathrm{ref}} &= Q_{\mathrm{LDS}},
\end{aligned}
\tag{4.3}
$$

which includes the transformation of full-beam into main-beam brightness temperature of the Stockert Survey. Stokes V is assumed zero.

The fitting problem can be expressed as follows: Each pointing n that has been observed with all three telescopes – DRAO 26-m, Stockert and Dwingeloo – results in an equation according to:

$$
\mathcal{M_1}' \cdot
\begin{pmatrix} \mathrm{RR} \\ \mathrm{LL} \\ \mathrm{RL} \\ \mathrm{LR} \end{pmatrix}_{\mathrm{raw},n}
=
\begin{pmatrix} \mathrm{RR} \\ \mathrm{LL} \\ \mathrm{RL} \\ \mathrm{LR} \end{pmatrix}_{\mathrm{ref},n}
,
\tag{4.4}
$$

with "raw" referring to the uncalibrated DRAO 26-m data. Hence, if the total number of pointings is m, this results in a set of m equations with $n = 1, 2, \ldots, m - 1, m$. By fitting the matrix entries m'_{11}, m'_{22}, m'_{33}, m'_{44}, m'_{34} and m'_{43} of the matrix $\mathcal{M}'_1$ by minimization of the difference between corrected raw data and reference values, the best solution of the set of m equations is found.

Determination of the matrix entries must be done by iterative fitting and cannot be achieved by least-square fitting. This is because the raw data are not corrected for ground radiation and system temperature drifts at this point. A least-square fit[1] is therefore not possible because $\mathrm{RR}_{\mathrm{raw}}$, $\mathrm{LL}_{\mathrm{raw}}$, $\mathrm{RL}_{\mathrm{raw}}$, $\mathrm{LR}_{\mathrm{raw}}$ still contain time and declination dependend offsets. These offsets must be approximated during fitting as done in the following algorithm (see Fig. 4.1 on the right):

1. The DRAO 26-m raw data of congruent pointings are corrected for electronic gain.

2. The initial matrix $\mathcal{M}'_1$ is set to be the unit matrix.

3. The DRAO 26-m raw data are corrected my multiplication with $\mathcal{M}'_1$ according to Equation 4.8.

---

[1]e.g. in this case applied to the following set of equations in order to obtain the coefficients m':

$$
\begin{aligned}
\mathrm{RR}_{\mathrm{ref},\{1\ldots n\}} &= m'_{11}\,\mathrm{RR}_{\mathrm{raw},\{1\ldots n\}} \\
\mathrm{LL}_{\mathrm{ref},\{1\ldots n\}} &= m'_{22}\,\mathrm{LL}_{\mathrm{raw},\{1\ldots n\}} \\
\mathrm{RL}_{\mathrm{ref},\{1\ldots n\}} &= m'_{33}\,\mathrm{RL}_{\mathrm{raw},\{1\ldots n\}} + m'_{34}\,\mathrm{LR}_{\mathrm{raw},\{1\ldots n\}} \\
\mathrm{LR}_{\mathrm{ref},\{1\ldots n\}} &= m'_{43}\,\mathrm{RL}_{\mathrm{raw},\{1\ldots n\}} + m'_{44}\,\mathrm{LR}_{\mathrm{raw},\{1\ldots n\}}
\end{aligned}
$$

4. Ground radiation and system temperature drifts are approximately removed by subtracting a linear baseline fitted through all congruent pointings lying on the same declination.

5. The fit-error is given as the sum of the squared differences between corrected DRAO 26-m data and the reference values.

6. Matrix entries of $\mathcal{M}_1'$ are either randomly altered and the iteration continues at point three or the iteration is stopped if the minimization of the fit-error is achieved.

Pre-calibration matrices are computed individually for each observing month. About $m = 100$ to 140 pointings with congruity of the pointing centres of $\leq 21'$ in all three surveys could be extracted for each observing month. The number of matches is mainly limited by the sparse number of data points from the LDS. Throughout the observing term a total of 860 matches was obtained. No time-dependence of the pre-calibration matrix was found.

Pre-Calibration of Raw Data

To account for an IF-filter change in November 2003, two different pre-calibration matrices were determined. The following matrices are used for the pre-calibration of the data:

$$\text{Nov 2003}: \quad \mathcal{M}_1' = \begin{pmatrix} 11.0 & 0 & 0 & 0 \\ 0 & 12.0 & 0 & 0 \\ 0 & 0 & -16.35 & 50.19 \\ 0 & 0 & 54.16 & 18.04 \end{pmatrix} \tag{4.5}$$

and

$$\text{Dec 2003} - \text{May 2004}: \quad \mathcal{M}_1' = \begin{pmatrix} 9.08 & 0 & 0 & 0 \\ 0 & 8.55 & 0 & 0 \\ 0 & 0 & -16.35 & 50.19 \\ 0 & 0 & 54.16 & 18.04 \end{pmatrix}, \tag{4.6}$$

with errors of the matrix entries as follows:

$$\text{Errors}: \quad \Delta\mathcal{M}_{1,2}' = \begin{pmatrix} 0.4 & 0 & 0 & 0 \\ 0 & 0.3 & 0 & 0 \\ 0 & 0 & 3.9 & 3.5 \\ 0 & 0 & 3.0 & 3.1 \end{pmatrix}. \tag{4.7}$$

The matrices show only small differences in the scaling factors of the total power channels for the two pairs of IF filters.

These matrices are applied to the raw data by computing the following matrix multiplication for each integration:

$$\begin{pmatrix} \text{RR} \\ \text{LL} \\ \text{RL} \\ \text{LL} \end{pmatrix}_{\text{corr}} = \mathcal{M}_1' \cdot \begin{pmatrix} \text{RR} \\ \text{LL} \\ \text{RL} \\ \text{LL} \end{pmatrix}_{\text{raw}}. \tag{4.8}$$

The pre-calibration is the first iteration step of an iterative determination of the instrumental Müller matrix. The second iteration step follows in Section 4.1.10.

4.1.5 Ground Radiation

Elevation scans were made periodically during the observing term. Like the survey raw-data, elevation scans are corrected for electronic gain and converted into brightness temperature. Ground radiation profiles for each channel are determined on the basis of elevation scans. Using the derived profiles the survey data are then corrected for ground radiation.

Determination of Ground Radiation Profiles

Four elevation scans are of high enough quality to be used for the determination of ground radiation profiles. Other elevation scans are either corrupted by gain jumps or showed strong sky contribution. The selected scans are first stacked, supposing that the averaged profiles in Stokes U and Q and the lower envelope in the total power channels roughly represent pure ground radiation. This is justified as the scans were taken at different sidereal times. The stacked profiles are then averaged along the elevation axis in bins of 7°.5 and fitted by a "spline"-function which should further minimize remaining sky emission. Although the scans used cover a bright polarized region, the averaged scans represent useful ground profiles.

Figure 4.3 shows the derived ground radiation profiles. The offset of the total power profiles is about 161 K at the minimum, which gives the system temperature without sky emission. The mean offsets of about 3.5 K in the Stokes-U-profile and -3.7 K in the Q-profile may indicate:

1. remaining phase and gain mismatches in the pre-hybrid part,

2. correlated receiver noise caused by cross-talk or backcoupling,

3. polarized backlobes of the telescope, picking up ground radiation.

The first can be excluded from the system check; more likely are the second and third. Also interesting is the north-south asymmetry about 90° elevation of the U and Q profiles, which may be due to the multipole structure of a telescope's response pattern to unpolarized radiation. The bump in the total power profiles at about 90° elevation may be spillover noise, which should be highest for the telescope pointing towards the Zenith.

Subtraction of Ground Radiation

Subtraction of ground radiation is straightforward. The ground offsets for each declination and channel are taken from the profiles. These offsets are then subtracted from the drift scans. This way, the declination-dependend component is removed and only the time-variable component of ground radiation and system temperature is left, which is corrected later in Section 4.1.8

The LDS provides absolutely calibrated reference points only for declinations above 0°, at which, in principle, the 26-m Survey could be calibrated without ground radiation profiles[2]. Below 0°, profiles are essential to set correct zero-levels in Stokes U and Q.

4.1.6 Gridding

Integrations are averaged and binned into a grid of equatorial coordinates with 15′ cell size, which is somewhat less then the telescope's HPBW/2 required for full Nyquist sampling. No particular weighting scheme is used; integrations are uniformly weighted and averaged across the cell. The gridding significantly reduces the amount of data.

---

[2]which has not been tested though
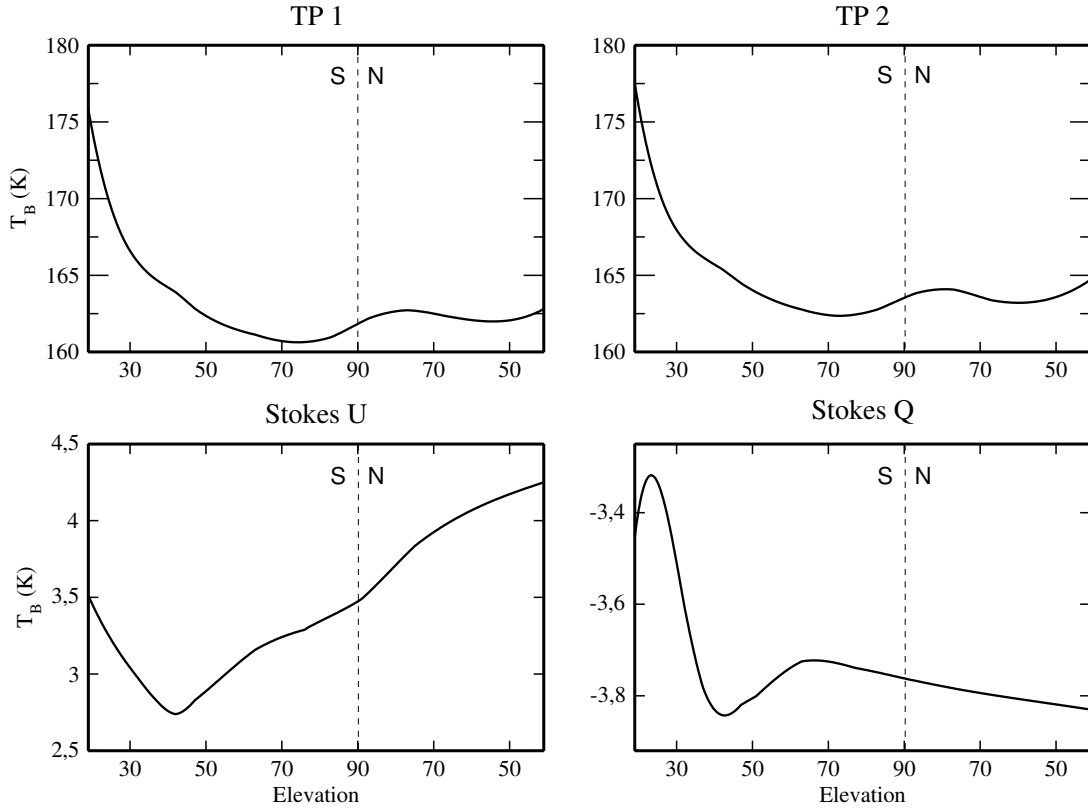
Figure 4.3: Ground radiation profiles determined on the basis of elevation scans, shown for total power (upper panels) and polarization (bottom panels). An explanation for the north-south asymmetry is given in the text.

4.1.7 Solar Interference and Ionospheric Faraday Rotation

Aside from automatic RFI flagging, which is done in the first step (Section 4.1.1), the data are now visually inspected for solar interference and ionospheric Faraday rotation. A graphical program was written to display and manually flag corrupted data. Whenever day-time data were used, drift scans were cross-checked with neighboring scans to recognize high levels of ionospheric Faraday rotation or solar interference. Only some of the day-time data show apparent solar interference and needed to be flagged. No indication was found for ionospheric Faraday rotation at night.

4.1.8 System Temperature Fluctuations

The correction of fluctuations of the system temperature turns out to be a crucial step in the data calibration. These fluctuations are possibly caused by variations of the ground radiation offsets during the observation. In the final map these fluctuations show up as stripes in total power and polarization and must be removed for calibration. Existing de-striping programs (e.g. NOD2 reduction package of the Effelsberg 100-m telescope) are not suitable and appropriate correction software thus needed to be written.

While the receiver-noise temperature is determined by ohmic losses in the receiving system and should therefore be rather constant, a gradual time-variability of the ground-noise temperature is ex-
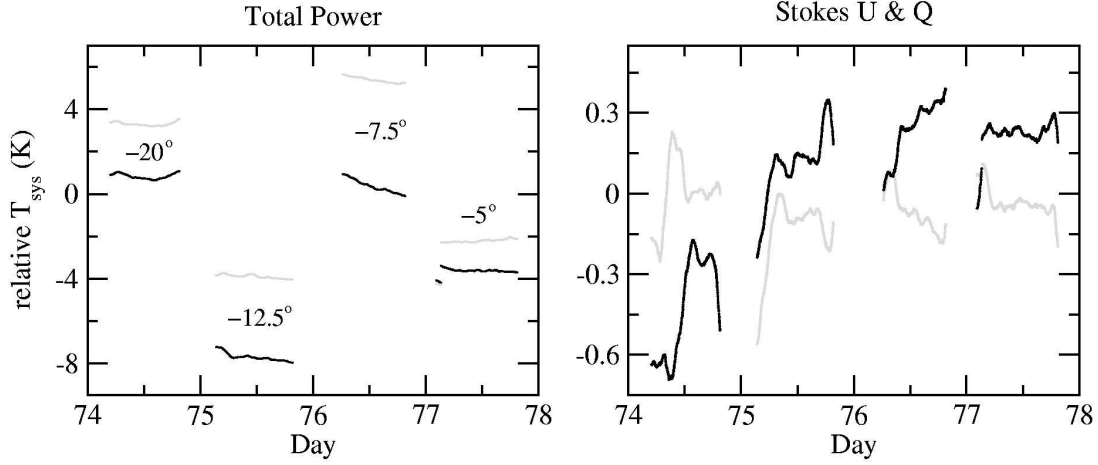
Figure 4.4: Example of system temperature drifts occurring during four observing nights in total power (left panel) and polarization (right panel) at different declinations. Ground radiation has been subtracted for these plots. The labels indicate declination.

pected as its level depends to a certain degree on environmental parameters and sidereal time. These effects should lead to a more or less systematic variation of the system temperature. However, the system temperature fluctuations found in the data seem only partly systematic and evidently have a random component (see Figure 4.4). The exact origin for the system temperature drifts remains unknown.

The amplitude of system temperature fluctuations is of the order of 100 mK at night, in total power and polarization. Over periods of weeks the amplitude of these fluctuations is $\lesssim 1$ K and the system temperature in total power can differ by several Kelvin in subsequent observing nights (after subtraction of ground radiation). The time-scale of these fluctuations ranges from hours to months. No correlation of fluctuations in total power with polarization is found in the survey data. To demonstrate the necessity of a correction the uncorrected polarized intensity map is shown in Figure 4.5.

The system temperature fluctuations must be corrected while large-scale sky emission in the data should be preserved to obtain absolutely calibrated maps. But variations of the system temperature cannot easily be distinguished from real sky emission. The following algorithm is therefore only a compromise solution in trying to preserve sky emission on all scales and correcting the system temperature fluctuations. The algorithm compares each drift scan pairwise with its neighboring scans. The basic assumption is made that system temperature fluctuation are random on time-scales of weeks, which means that fluctuations observed at the same declination but weeks apart are assumed to be uncorrelated. Furthermore, if two neighboring drift scans with slightly different declinations are compared, and if both were observed weeks apart, the system temperature fluctuations might differ, but not the large-scale structure contained in these scans. The declination range from which neighboring scans are selected is adjustable in the program as described in the following.

The following algorithm makes an iterative separation of random and systematic structures in the drift scans. Let m be an index numbering all observed drift scans. The following loop is applied until m has reached the total number of scans:

1. To the drift scan with index m all neighboring scans n within $\pm\delta°$ in declination are assorted. For δ values between 3 and 40 were found to be useful.

2. Each pair of drift scans (m,n) is convolved with a Gaussian. The width of the Gaussian is σ times the separation in declination $\Delta d_{m,n} = |d_m - d_n|$ of the two drift scans. This removes spatial
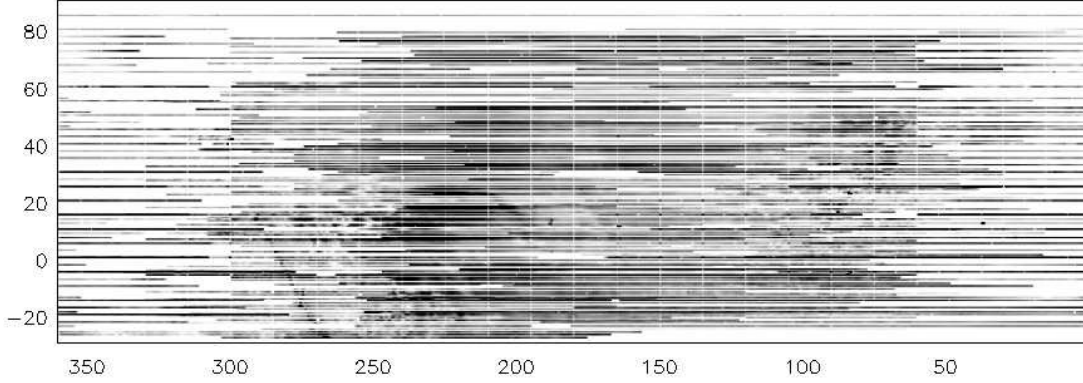
Figure 4.5: Uncleaned map of polarized intensity on a rectangular RA–DEC grid.

structures smaller than $\sigma \cdot \Delta d_{m,n}$. Values for σ between 4 and 100 are useful here.

3. The weight $w_{m,n} = |\delta - \Delta d_{m,n}|$ is introduced.

4. The difference of each pair of drift scans $\Delta T_{m,n}$ is calculated. The sum of these differences multiplied with the weight $w_{m,n}$ is then subtracted from the m-th drift scan: $T'_m = T_m - \sum_n w_{m,n} \cdot \Delta T_{m,n}$ with T denoting brightness temperature.

5. Index m is increased by one and the loop restarted until m reaches the number of scans.

This algorithm is applied 11 times with different parameters as listed in Table 4.1 until a satisfying separation of sky emission and system temperature is achieved.

The algorithm correctly preserves small-scale structures but some problems must be noted for large-scale emission, especially if these structures are elongated along right ascension. Moreover, if the coverage is low and neighboring drift scans are several degrees apart, as it is the case around 0^h right ascension, effectiveness of the algorithm is limited. Both problems can be reduced when more drift scans become available.

4.1.9 Interpolation

Most parts of the sky at right ascension between 4^h and 20^h have been observed in steps of $1°$ to $2°$ in declination. Parts of the sky around 0^h R.A. could only be observed in steps of $5°$. This requires an interpolation of scans. But in contrast to "uniform" undersampling, the 26-m Survey is fully sampled along the R.A.-axis and undersampled only in declination. Considering this specific sampling problem an interpolation routine was written that works in the Fourier domain as follows.

Table 4.1: Parameters used for the correction of system temperature fluctuations.

Loop	δ	σ
1 - 4	40	100
5	10	15
6 - 9	6	8
10 - 11	3	4

The drifts scans are Fourier transformed, using the DFT[3]-algorithm of AIPS++. Unobserved declinations are filled by linear interpolation of the Fourier transformed drift scans. The interpolated scans are then reverse transformed into the image plane. This algorithm does not affect observed scans so that it is possible to extract the original observations from the interpolated map.

In a second interpolation step, a few remaining pixels at the map edges, which could not be interpolated in the Fourier domain, are interpolated in the image plane. These pixels are replaced by the mean of neighboring pixels, weighted with the inverse of the distance.

For test purposes the data have also been interpolated employing a number of available programs (e.g. NOD2 routines, GILDAS software), which interpolate in the image plane. These algorithms often calculate means of pixel values using more or less sophisticated weighting schemes. It was found that the Fourier interpolation preserves the large-scale structure better than an interpolation in the image plane. However, each kind of analysis should imply a proper way of doing the interpolation, if required for the scientific purpose at all. Therefore it is planned to make the 26-m Survey publicly available in form of Fourier interpolated maps as well as individual drift scans.

4.1.10 Second Calibration

Up to this reduction step the data are not corrected for instrumental cross-talk. This, and a more accurate scaling and rotation of the RL and LR scales, is computed in the following. Similar as for the pre-calibration, a correction matrix is applied to the 4-vector formed from the four polarimeter channels. No further corrections of the total power data are made as the intention is the measurement of polarization. Instead of iterative fitting, least-square fitting can now be applied because the raw data are already corrected for electronic gain and ground radiation. The reference points are again taken from the Leiden-Dwingeloo polarization survey.

A single calibration matrix is determined for the whole data set. The following correction matrix $\mathcal{M}_2'$ is found:

$$\mathcal{M}_2' = \begin{pmatrix} 1 & 0 & 0 & 0 \\ 0 & 1 & 0 & 0 \\ 0.025 & -0.023 & 1.12 & 0.05 \\ 0.014 & -0.041 & 0.05 & 1.03 \end{pmatrix}, \tag{4.9}$$

with errors of ± 0.01 of the matrix entries. Raw data are corrected according to Equation 4.8. The scaling correction caused by the second calibration is small – scaling factors are around unity. Cross-talk values of 0.2% in Stokes U (RL) and -2.7% in Q (LR) are found.

4.1.11 Final Editing

A manual editing of the final Stokes U and Q maps is unavoidable. This editing involves the following steps:

1. The program that corrects system temperature fluctuations (Section 4.1.8) works in a rectangular grid of equatorial coordinates. This program assumes that drift scans run from 0^h to 24^h in right ascension. After subtraction of system temperature, discontinuities at 0 hour are left. These jumps are of the order $\lesssim 30$ mK and corrected by baseline adjustment within a 2^h right ascension interval between 23^h and 1^h.

2. Although the automated flagging routine (Section 4.1.1) flagged most of the RFI correctly, a few spikes in the data must be edited by hand. By utilizing available software packages, the Stokes U

---

[3]Discrete Fourier Transformation

and Q maps are displayed (using *kview*[4]) and a bad pixel mask created. Bad pixels are replaced by interpolated pixel values (*iraf*[5], task: *fixpix*).

3. The final Stokes U and Q maps are smoothed with a Gaussian beam to remove sub-beam structures. The FWHM of the Gaussian is $36'$. If the smoothing is done within a rectangular grid of equatorial coordinates, the FWHM beam must be adapted to the declination (FWHM = $36'/\cos\delta$).

4.2 Refinement of Temperature Scale

A comparison of the 26-m Survey with polarization data taken from the EMLS reveals a mismatch of both brightness temperature scales. Temperatures from the 26-m Survey are systematically too high by a factor of 1.18 ± 0.03 compared with the EMLS. An overestimation of the Dwingeloo main-beam temperature scale must be assumed, because the calibration scheme ties the 26-m Survey to the Dwingeloo survey. A possible reason for the inaccuracy is that the LDS itself was calibrated merely against two calibration points, of which polarized intensities were known only to some precision.

The data used for the comparison of brightness temperatures are taken from two regions: a $35°\times 35°$ large map towards Cassiopeia-A and a $40°\times 16°$ large map toward the Taurus-Auriga-Perseus molecular clouds. These are preliminary maps from the EMLS, which are covered by 28 drift scans from the 26-m Survey.

As the EMLS lacks large-scale emission (see Chapter 1) a direct comparison with the 26-m Survey is therefore not meaningful. As a solution, missing large-scale structures in the EMLS are approximated by polynomials of first to third order. The coefficients of these polynomials and the scaling factor of the 26-m temperature scale are then fitted to the Effelsberg data, with the difference between EMLS and 26-m Survey to be minimized. Figure 4.6 shows two example scans used for this comparison.

It is certain that the main-beam temperature scale of the EMLS is determined more accurately than that of the LDS. Because of the higher sensitivity of the Effelsberg 100-m telescope, standard calibration sources with well known fluxes can be used for calibration. This is almost impossible with small-diameter telescopes and uncooled receivers. Therefore, the temperature scale of the 26-m Survey is re-calibrated against the EMLS temperature scale which, in turn, is determined on the basis of standard calibrators. Hence, temperatures quoted in the 26-m Survey conform to the Effelsberg main-beam brightness temperatures scale.

4.3 Error Analysis

Several error sources contribute to the error budget of the 26-m Survey. The relevance of the following errors and their influence on the final Stokes U and Q maps must be discussed:

1. Errors of the entries in the system Müller matrix cause systematic errors in the data. Considering pre-calibration and second matrix the error is estimated to be $\sim 6\%$.

2. Non-circular response of the receiver to polarized signals.

3. Uncorrected instrumental polarization caused by sources received through the side lobes.

4. Errors in the LDS.

---

[4]kview is part of the karma toolkit (http://www.atnf.csiro.au/computing/software/karma/)
[5]iraf: Image Reduction and Analysis Facility (http://iraf.noao.edu/)
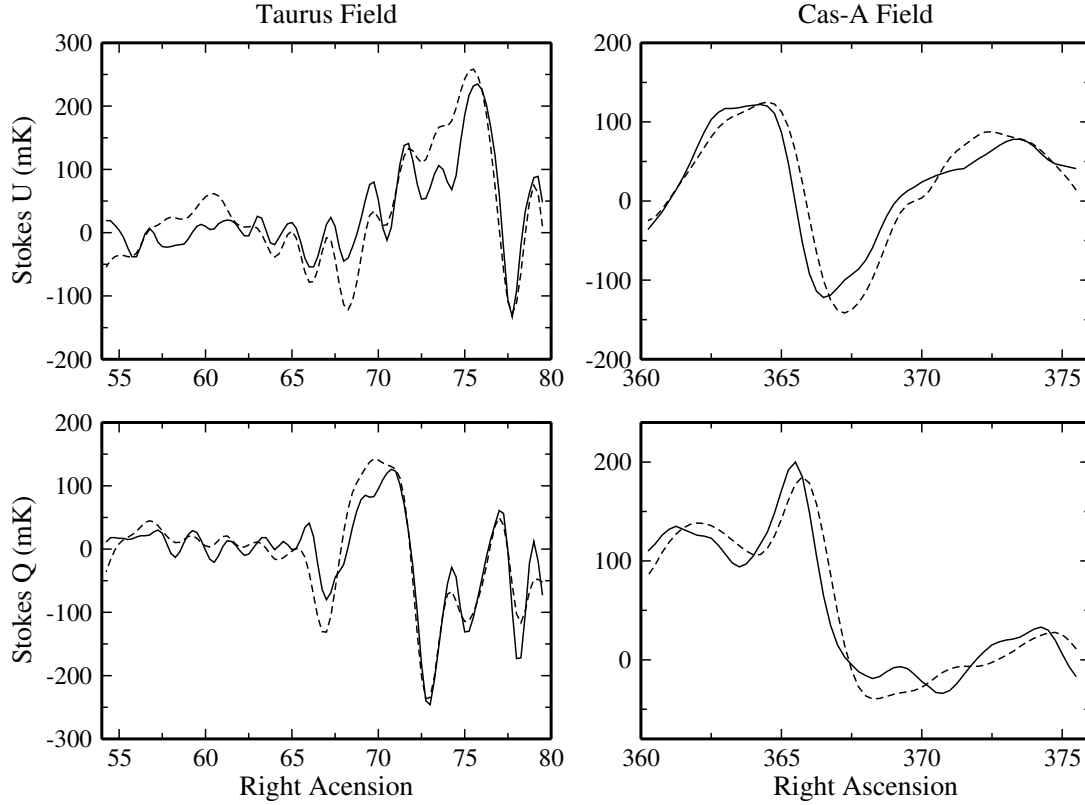
Figure 4.6: Two example scans through the Taurus complex (left panels) and Cassiopeia-A (right panels). The dashed lines show EMLS data and the solid lines 26-m Survey data. The missing large-scale emission in the EMLS data is approximated by polynomials. The DRAO 26-m data are divided by 1.18.

5. Sudden changes of environmental parameters such as humidity, ambient temperature, etc. affect the system temperature and telescope gain. Affected data must be flagged. If the effects in Stokes U and Q are smaller then 10 mK, they are unlikely to be detected in view of the noise level and increase the error.

6. System temperature fluctuations are corrected by a program (Section 4.1.8). To a certain degree this program confuses structures elongated along right ascension with system temperature fluctuations. This may cause errors of about $\lesssim$ 30 mK as derived from simulations.

7. Below $0°$, errors in the ground radiation profiles causes incorrect zero-levels in U and Q. Because of the averaging and fitting of several elevation scans, these errors are certainly below 50 mK.

4.3.1 The System Müller Matrix

To investigate the system properties a Müller matrix for the telescope is calculated. Only the second calibration matrix (Equation 4.9) is considered, because the pre-calibration matrix does a scaling and rotation. Moreover, as for the calibration the basis consisting of RR, LL, RL, and LR is used, the second calibration matrix must be transformed into a Müller matrix to be applicable to Stokes parameters.
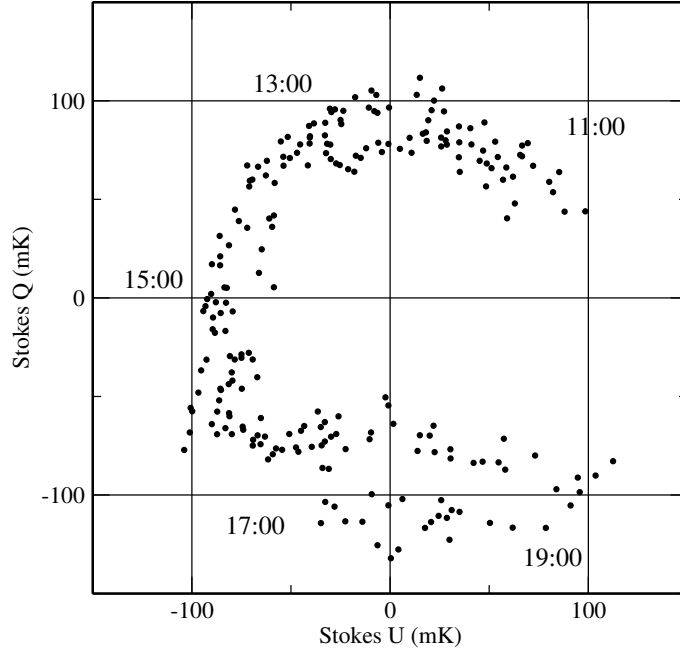
Figure 4.7: An 8 hour night-time observation of the northern celestial pole, obtained on May 14, 2003. Indicated are sidereal time of observation.

Hence, the system Müller matrix $\mathcal{M}_{\text{sys}}$ is:

$$\mathcal{M}_{\text{sys}} = \mathcal{T}^{-1} \mathcal{M}_2'^{-1} \mathcal{T} = \begin{pmatrix} 1 & 0 & 0 & 0 \\ 0.013 & 0.973 & -0.043 & -0.026 \\ -0.001 & -0.043 & 0.895 & -0.020 \\ 0 & 0 & 0 & 1 \end{pmatrix} \tag{4.10}$$

and reflects the modification of the initial signal vector (I, Q, U, V) of the source on its way through the receiving system before entering the polarimeter.

The system Müller matrix can be expressed using the parameterized form of Equation 3.45. The corresponding parameters for the feed are:

$$\begin{aligned} \epsilon_1 &= 21.3 \\ \epsilon_2 &= -21.3 \\ \phi_1 &= 89.8° \\ \phi_2 &= 90.3°. \end{aligned} \tag{4.11}$$

And for the hybrid these are:

$$\begin{aligned} g_{ya} &= -0.16 \\ g_{xb} &= -0.16 \\ \phi_{ya} &= -5.7° \\ \phi_{xb} &= -5.7°. \end{aligned} \tag{4.12}$$

These parameters indicate good gain and phase matching in the pre-hybrid part of the receiver.
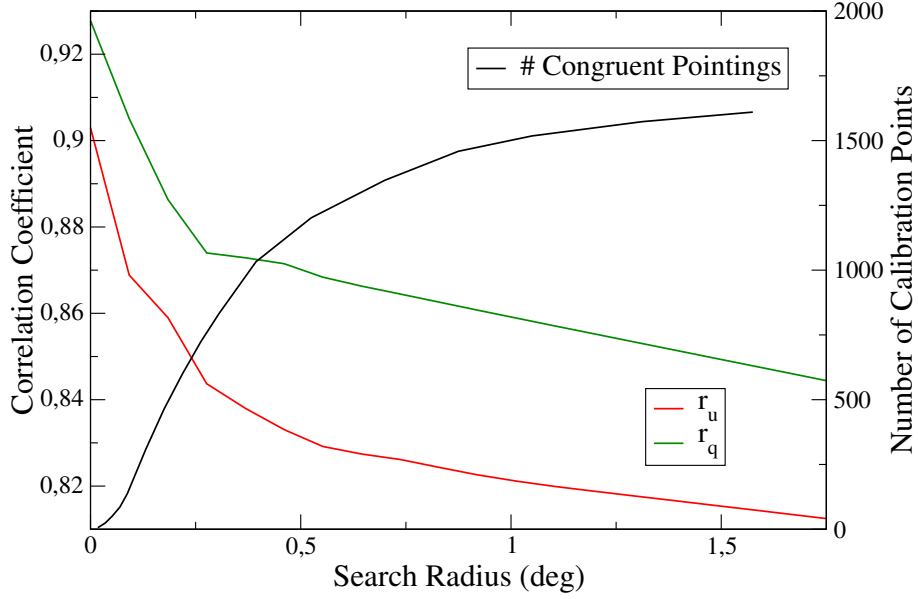
Figure 4.8: Correlation coefficients of Stokes U and Q and number of matches plotted versus the congruence radius.

4.3.2 Response

The circularity of the response after calibration can be checked using the NCP measurements. Figure 4.7 displays a fully calibrated 8 hour observation of the NCP. At the end of the scan ($U \gtrsim 0$ mK, $Q \lesssim 0$ mK) solar interference and ionospheric Faraday rotation probably disturbed the observation. This measurement confirms the circularity of the system response.

The polarized intensity of the NCP could be determined to be 85 mK. Within the errors this is in agreement with the temperature derived with the Leiden telescope of 60 mK at 1.4 GHz (see Figure 1.3). NCP scans must be used with care because of a 1.35 Jy bright point source 25′ from the pole (NVSS J001327+893528). Observed with the DRAO 26-m telescope the brightness temperature of this source is 100 mK, resulting in a side lobe instrumental polarization of $\lesssim 10$ mK.

If the response is circular the deviation from a perfect cycle gives the resulting noise. Excluding the disturbed periods at the end of the NCP-measurement, the noise is 12 mK rms in Stokes U and Q for an integration time of 60 s.

4.3.3 Side Lobe Polarization

Instrumental polarization caused by side lobes cannot be neglected in the presence of strong, compact sources within a radius of 2° around the main beam. This is the case, for example, toward the Galactic plane in the first quadrant where total power emission is intense. There, side lobe polarization is visible as polarized stripes at $b \approx \pm 1°$ and $l \lesssim 50°$, running parallel to the Galactic plane. However, only compact emission with brightness temperatures of ~ 2 K or higher in total power may cause errors of ~ 40 mK or more, depending on the source position relative to the main beam. The error caused by diffuse total power emission is mostly negligible.
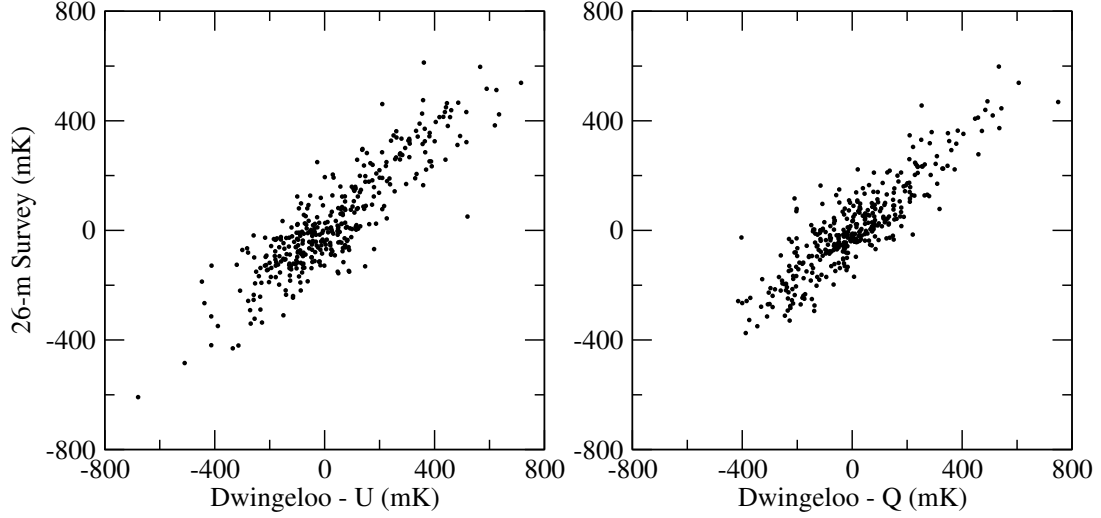
Figure 4.9: Correlation of Stokes *U* (left panel) and *Q* (right panel) intensities from the DRAO 26-m
Survey with the Dwingeloo survey before adjusting the temperatures to the Effelsberg scale.

4.3.4 Noisy Reference Values and Congruence Radius

The average error of the reference points from the LDS is quoted as 60 mK. Numerical simulations show that errors in the reference values propagate through the calibration matrix into the calibrated raw data and cause systematic errors. In case of 100 congruent pointings per month, the errors in the Dwingeloo data cause errors around 6 mK in the calibrated data. Taking the whole set of congruent pointings, an error of 3 mK in the final data results, which is solely due to errors in the reference values.

Pointings are called congruent if their pointing centres match within a certain search radius. If a small radius is chosen, the correlation coefficient between final data and reference values rises because data are more comparable, but the total number of congruent pointings falls. On the other hand, if the radius is large, the number of matching pointings increases but data become less comparable. In Figure 4.8 the correlation coefficients and the number of matches versus the search radius are plotted. A search radius of $\leq 0°\!\!.35$ appears to be a reasonable trade-off.

Figure 4.9 shows the correlation of the final data with the reference values. The correlation co-efficients are $r_U = 0.88$ and $r_Q = 0.87$. Using the above mentioned simulation, these correlation coefficients can be converted into an error. Assuming 60 mK error in the Dwingeloo data, an error of about 30 mK in the 26-m Survey data is required to reproduce the correlation coefficients of the T-T plots. This error includes systematic and random errors and can be considered as the final average error.

4.3.5 Repeatability of Drift Scans

Some drift scans are observed twice to check repeatability. Figure 4.10 displays four repeated and calibrated scans that were observed two months apart. The standard deviation of the difference of repeated scans is around 25 mK with a maximum of 41 mK, confirming the error derived on the basis of the correlation coefficients.
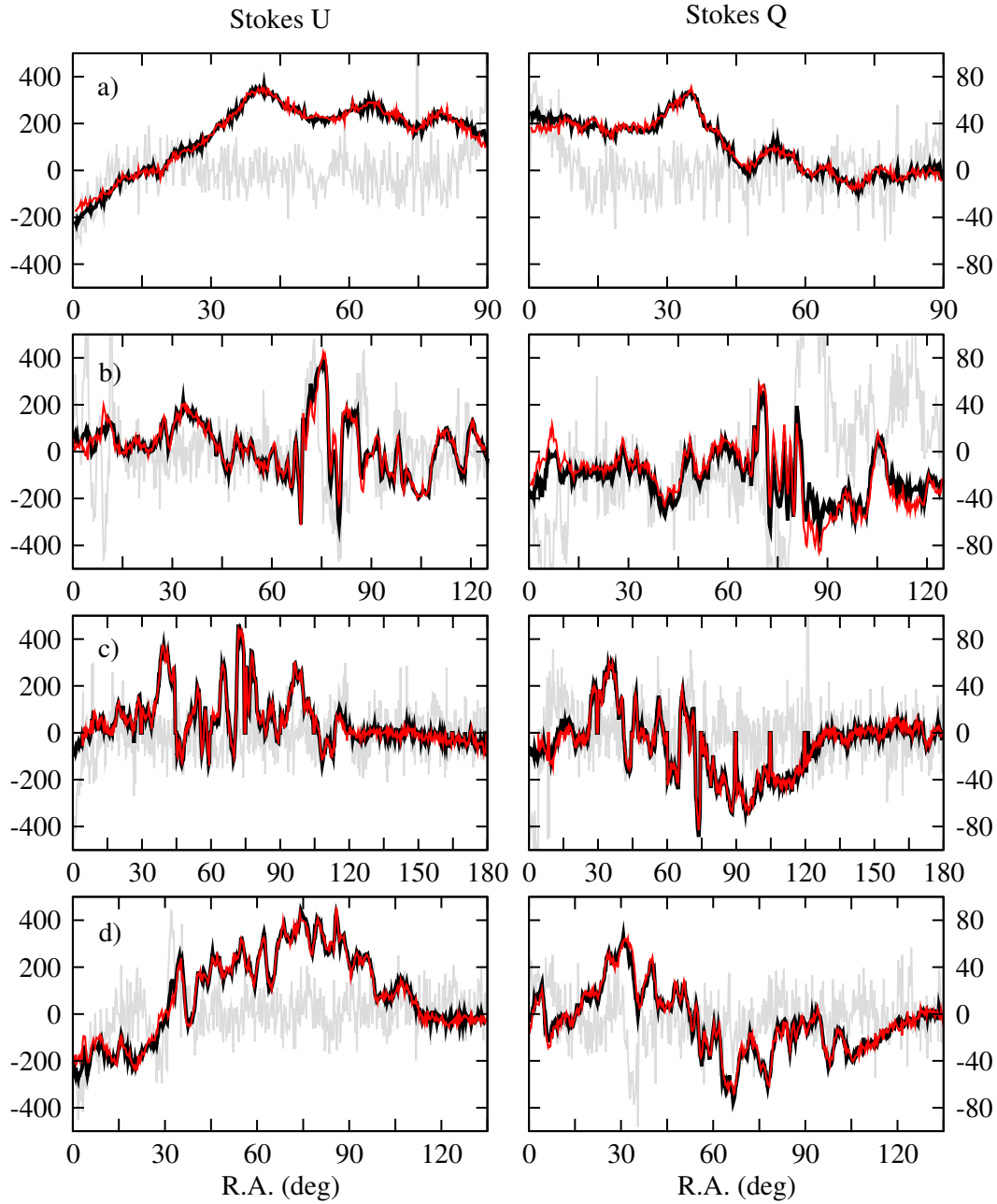
Figure 4.10: Plot shows Stokes *U* (left) and *Q* (right) of repeated scans. Repetitions are plotted in red and the difference of both in grey. The left scale shows *U*, *Q* brightness temperatures, the right applies to the difference. The declinations are: 75° (a), 30° (b), 40° (c) and 50° (d). The standard deviation of the differences are: a) 20 mK, 22 mK, b) 28 mK, 41 mK, c) 19 mK, 23 mK, and d) 23 mK, 22 mK.

Table 4.2: Error budget of the 26-m Survey.

Contribution	Error ΔT	Comment
System Matrix	$\sim 6\%$	
Response	0 mK	response is circular
Side Lobe Polarization	$\lesssim 40$ mK	only for compact sources
Reference Values	3 mK	
Weather	$\lesssim 10$ mK	if undetected
T_{sys}-Correction	$\lesssim 30$ mK	up to ~ 100 mK (see text)
Ground Radiation Profiles	$\lesssim 50$ mK	below $0°$ declination
Rms-Noise	12 mK	from NCP scan

4.3.6 Final Error

Summing up the above mentioned error contributions, an error budget (Table 4.2) can be stated. A direct measurement of the rms-noise of 12 mK per 60 s integration was derived from the NCP measurement (Figure 4.7). Based on the correlation coefficients and the repeated drift scans, the final average error in Stokes U and Q of the 26-m Survey amounts to 30 mK. The error may be as high as 100 mK in case of intense polarized structures, elongated along the R.A.-axis.

When more data become available the system Müller matrix can be determined more precisely using more congruent pointings. Also the system temperature correction can be done more accurately because drift scans can then be compared with a larger number of neighbouring scans. These two error contributions are expected to decrease in the data intended for publication.

5 Survey Maps

In J2000 coordinates on a rectangular grid are shown:

Page 68: This map shows the sky coverage. Black lines indicate observed drift scans.

Page 69: This map shows Stokes U. Contours run from -400 mK to 400 mK in steps of 100 mK.

Page 70: This map shows Stokes Q. Colour cuts and contours are the same as for Stokes U.

Page 71: This map shows polarized intensity. Contours run from 100 mK to 500 mK in steps of 100 mK.

In Galactic coordinates on a rectangular grid are shown:

Page 72: This map shows the sky coverage. Black lines indicate drift scans.

Page 73: This map shows Stokes U. Colour cuts and contours are the same as for Stokes U in J2000 coordinates.

Page 74: This map shows Stokes Q. Colour cuts and contours are the same as for Stokes U in J2000 coordinates.

Page 75: This map shows polarized intensity. Colour cuts and contours are the same as for polarized intensity in J2000 coordinates.

Page 76: This map shows the large-scale polarized emission. Colour cuts and contours are the same as for polarized intensity.

Page 77: This map shows the small-scale polarized emission. Colour cuts and contours are the same as for polarized intensity.

Page 78: This map shows the percentage polarization. Contours run from 10% to 70% in steps of 20%. The map is calculated using the total power survey of Reich (1982) and Reich & Reich (1986) and subtracting a background level of 3200 mK from this map.

Large-scale and small-scale emission has been separated by convolution of the Stokes U and Q maps with a Gaussian of 7.°5 FWHM. The convolved map represents the large-scale emission, whereas the small-scale emission is represented by the difference between original and convolved map.

J2000 Right Ascension

J2000 Declination

68

Stokes U

J2000 Right Ascension

J2000 Declination

mK

69

70

Pol. Int. + E-Vectors

J2000 Right Ascension

J2000 Declination

71

72

73

Stokes Q

74

75

Pol. Int. + E-Vectors (Large Scale)

76

Pol. Int. + E−Vectors (Small Scale)

77

78
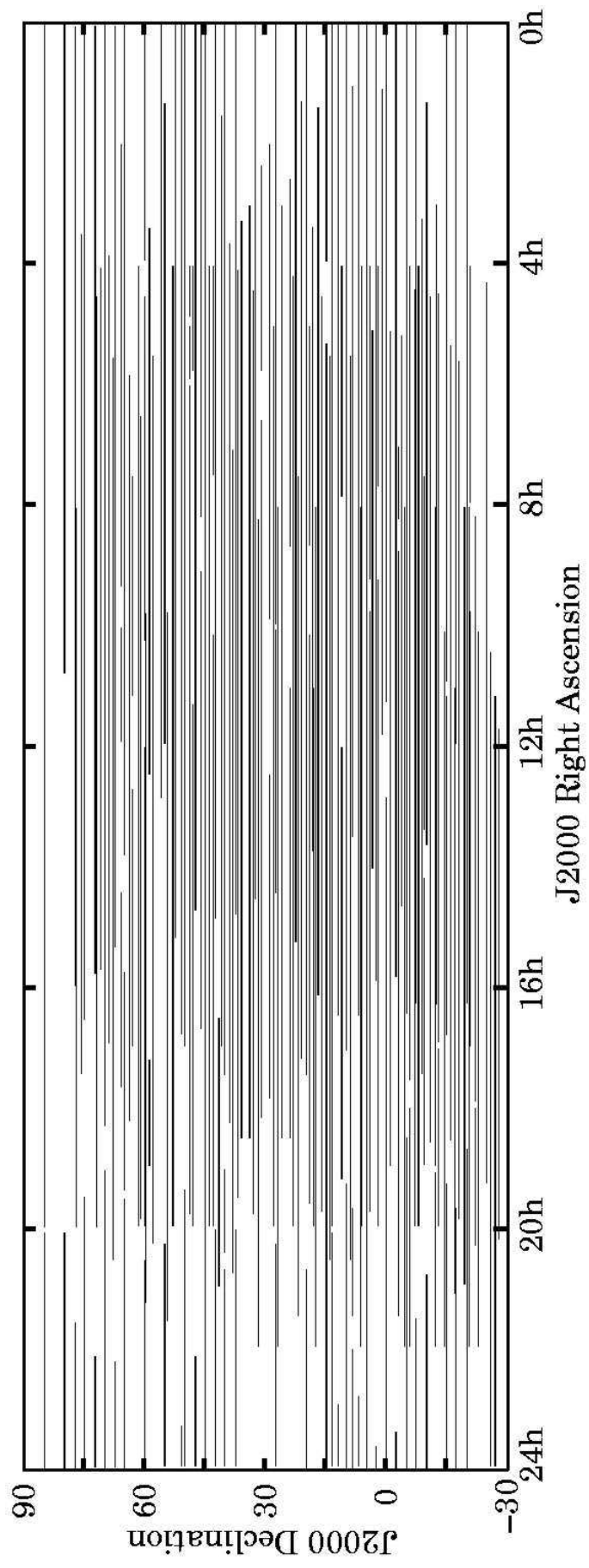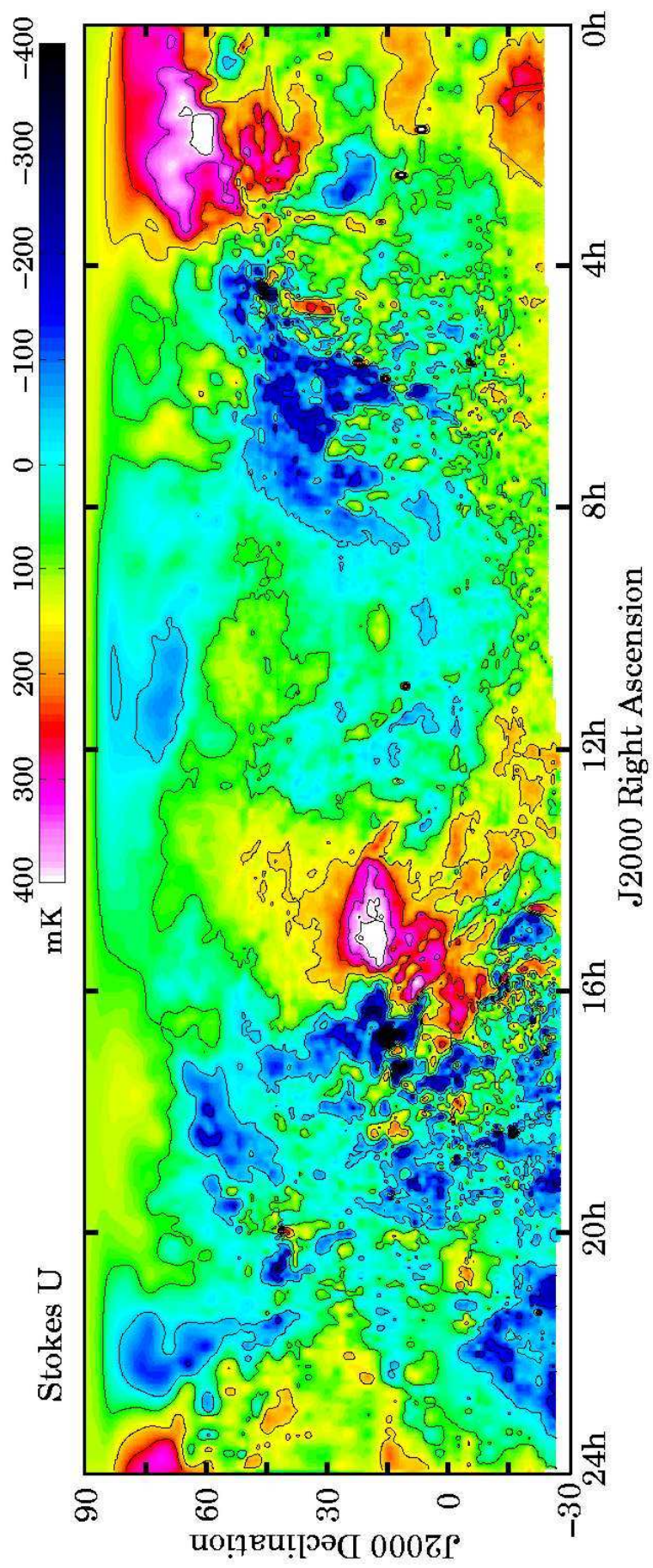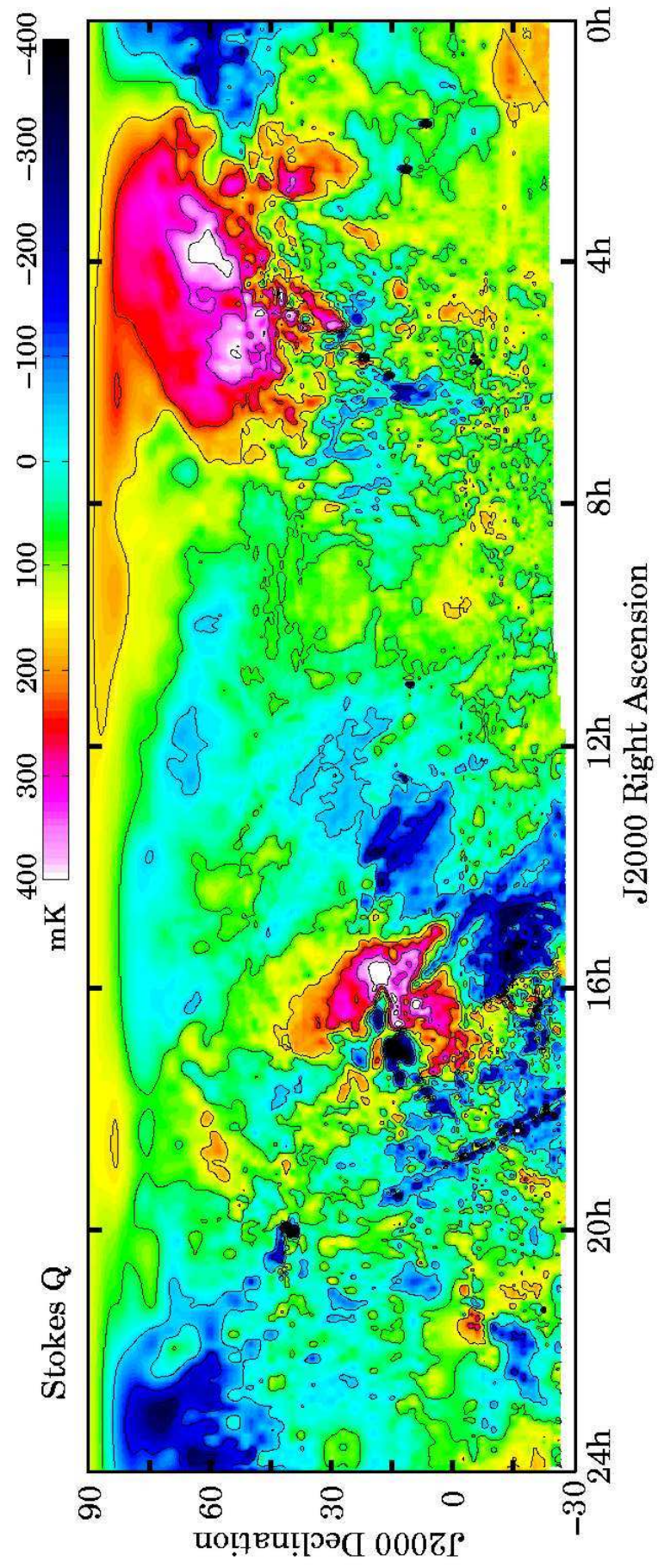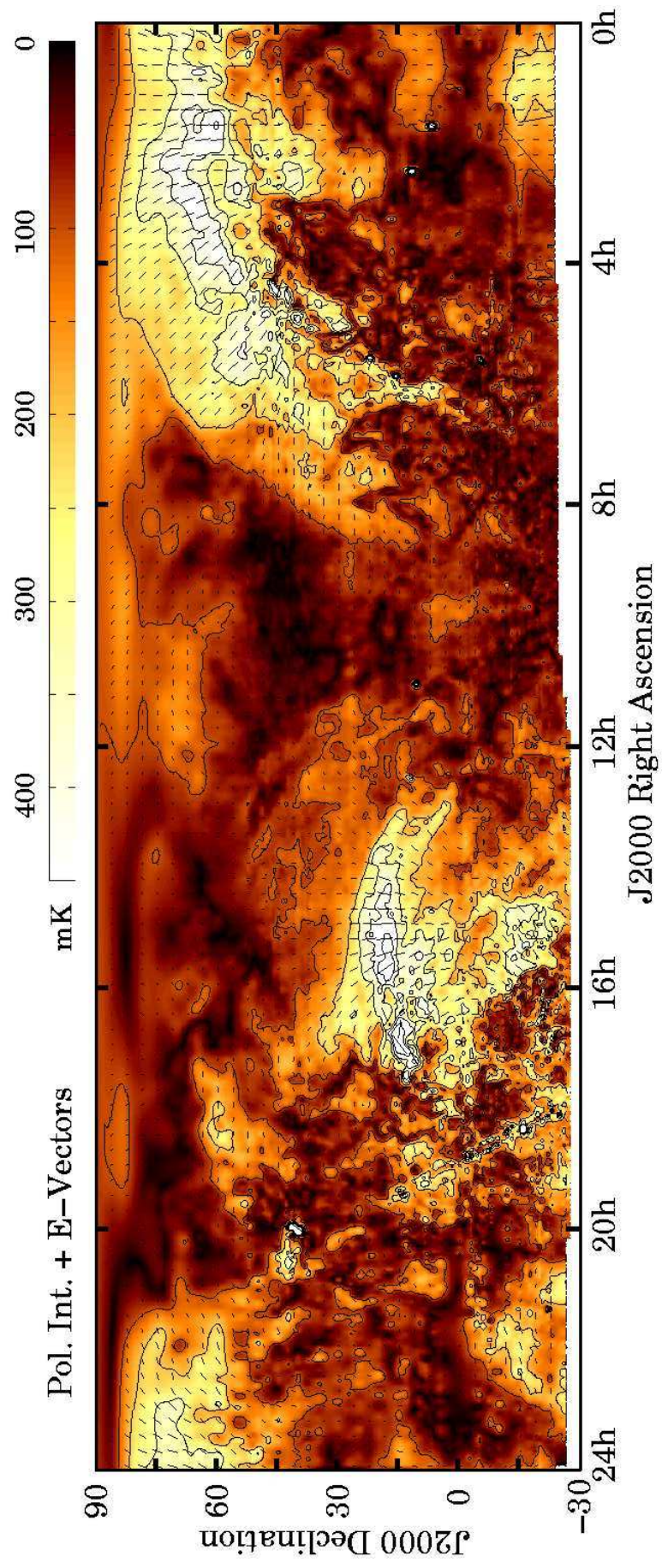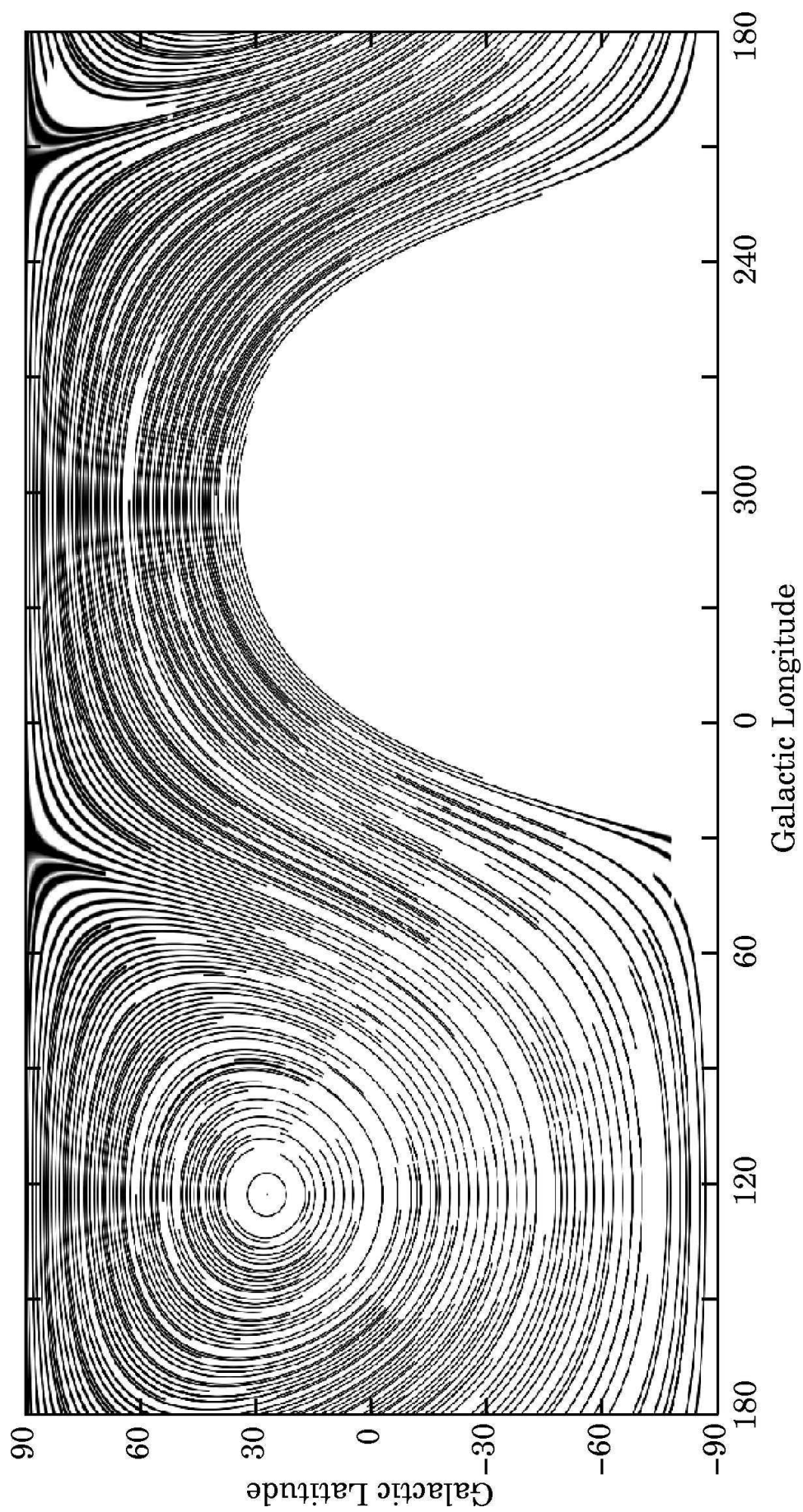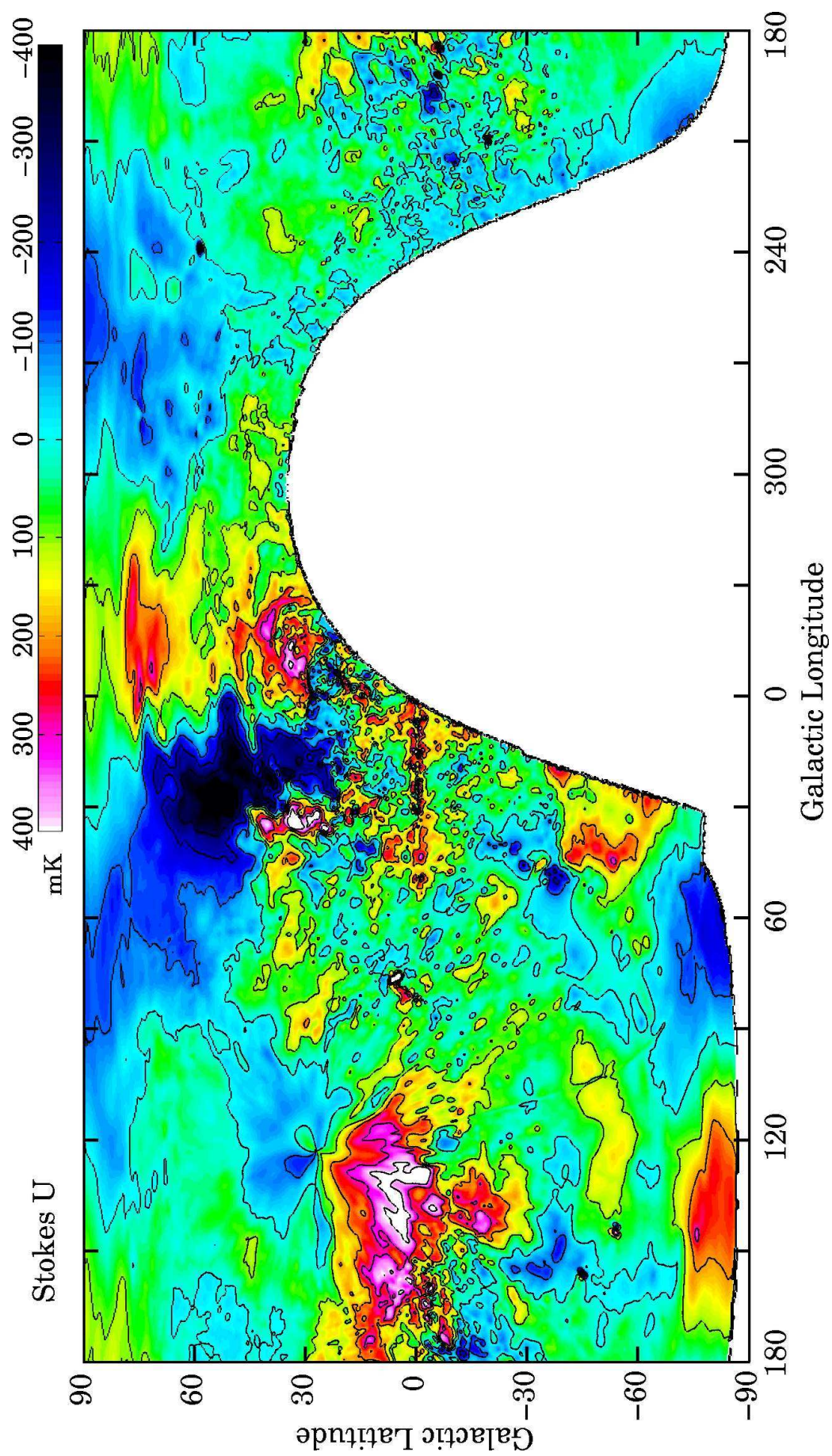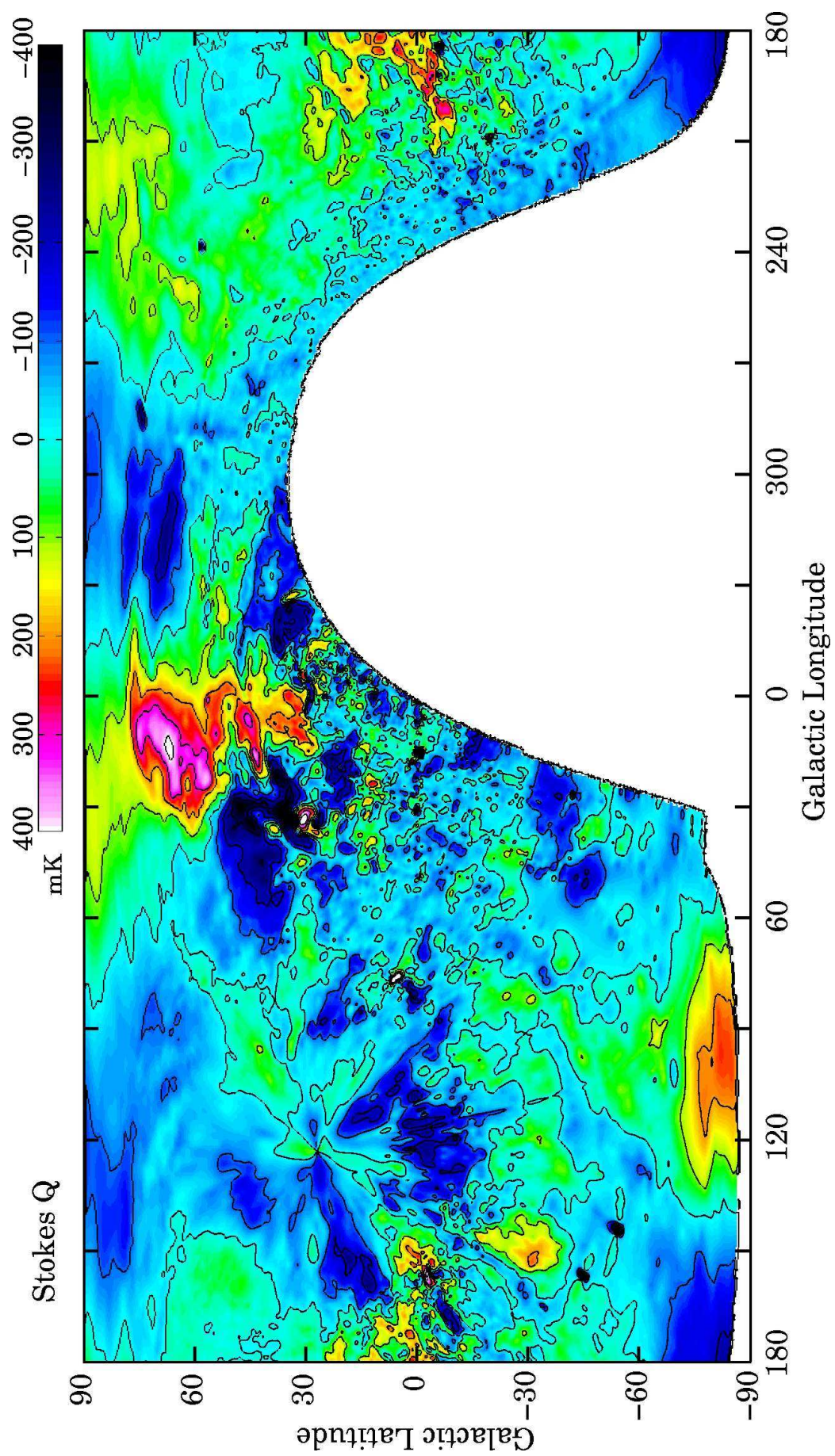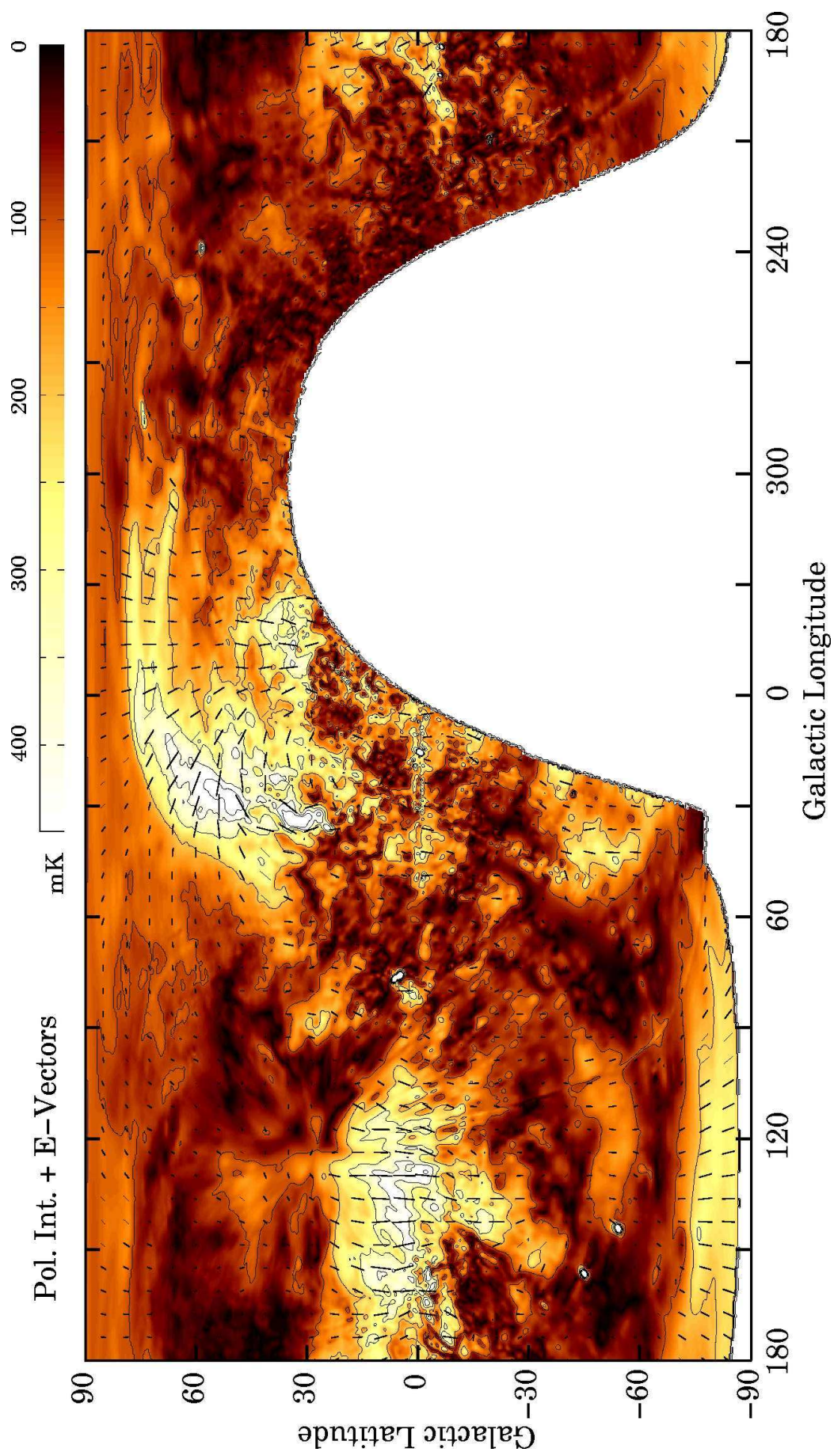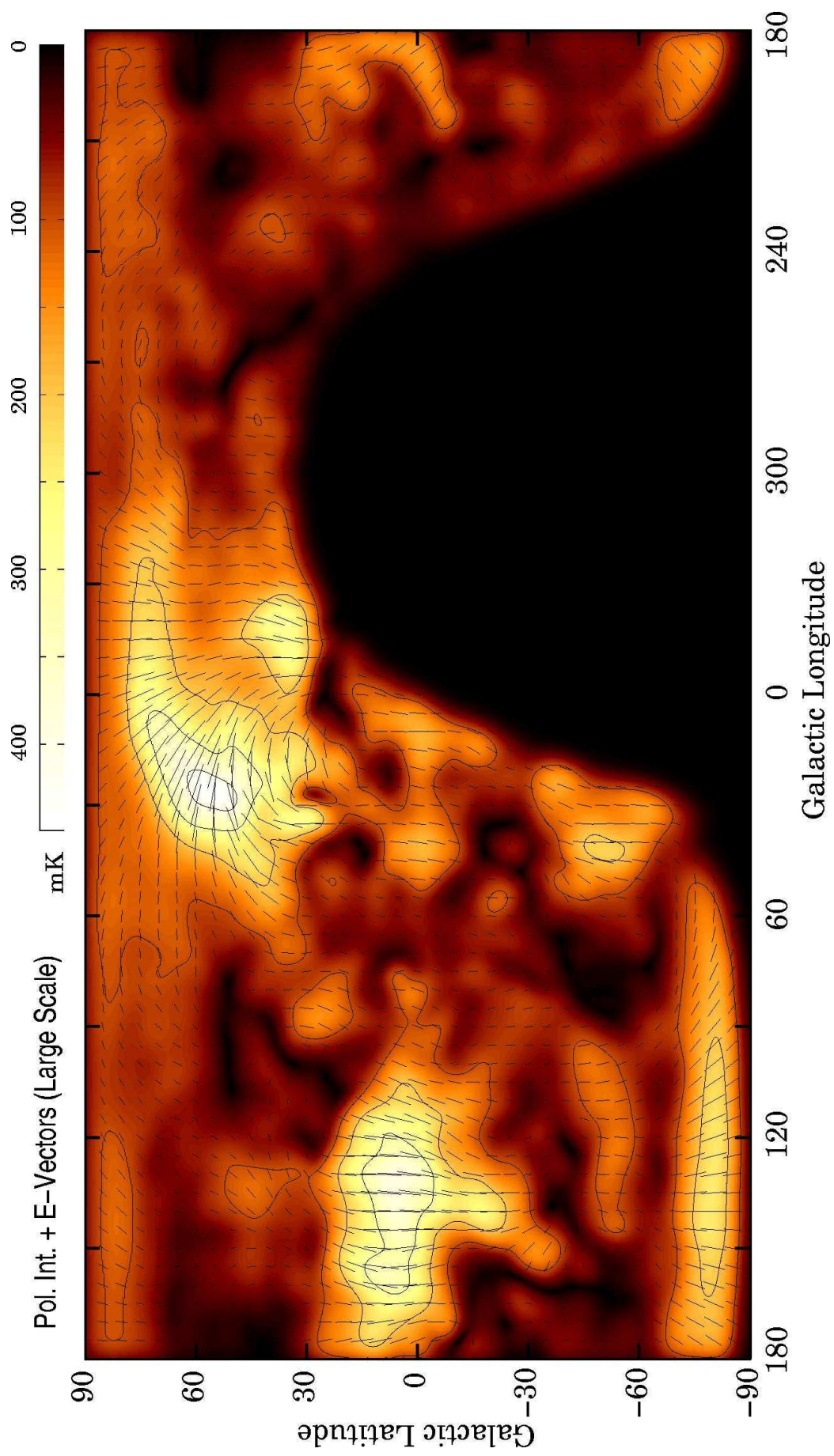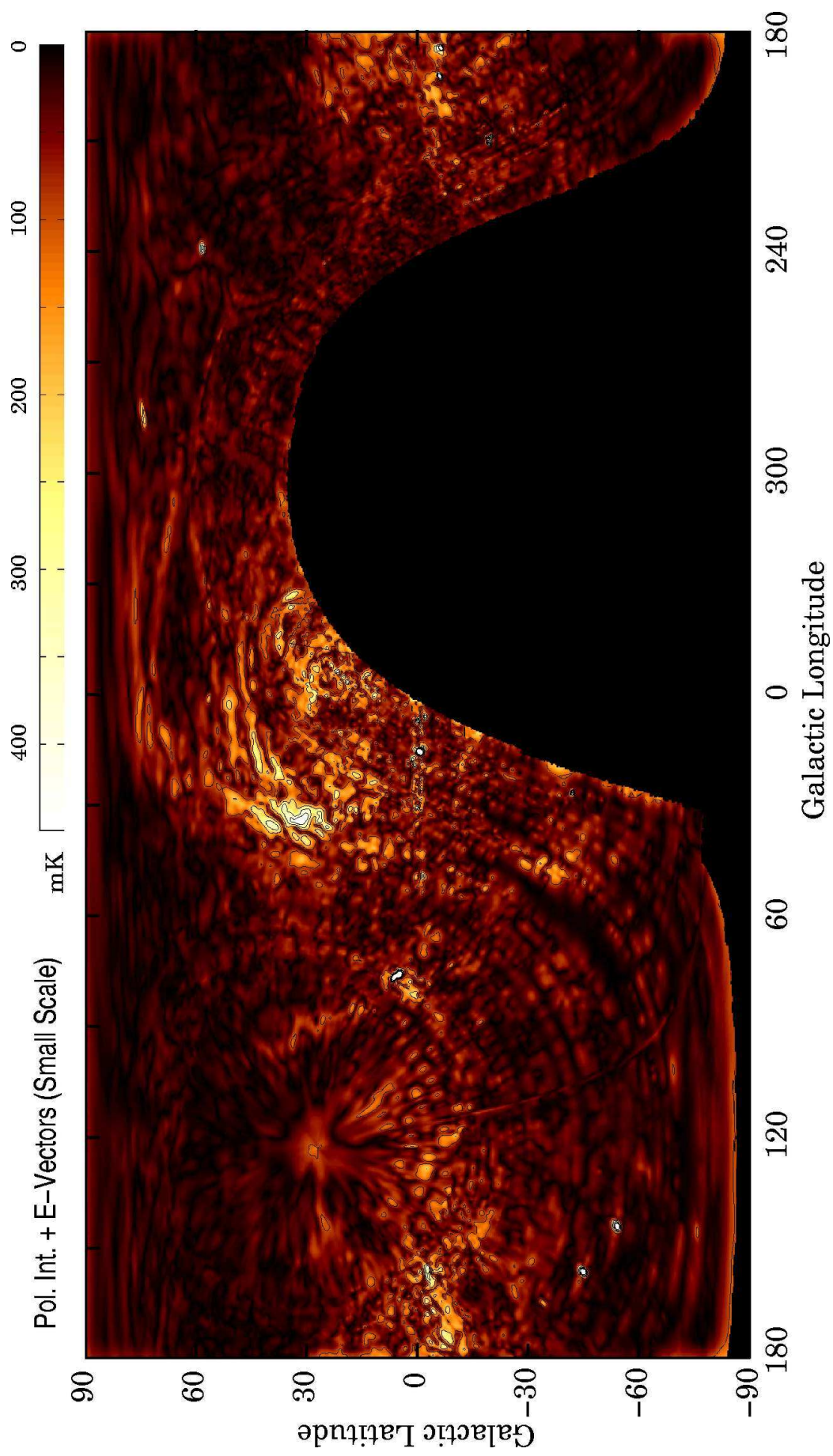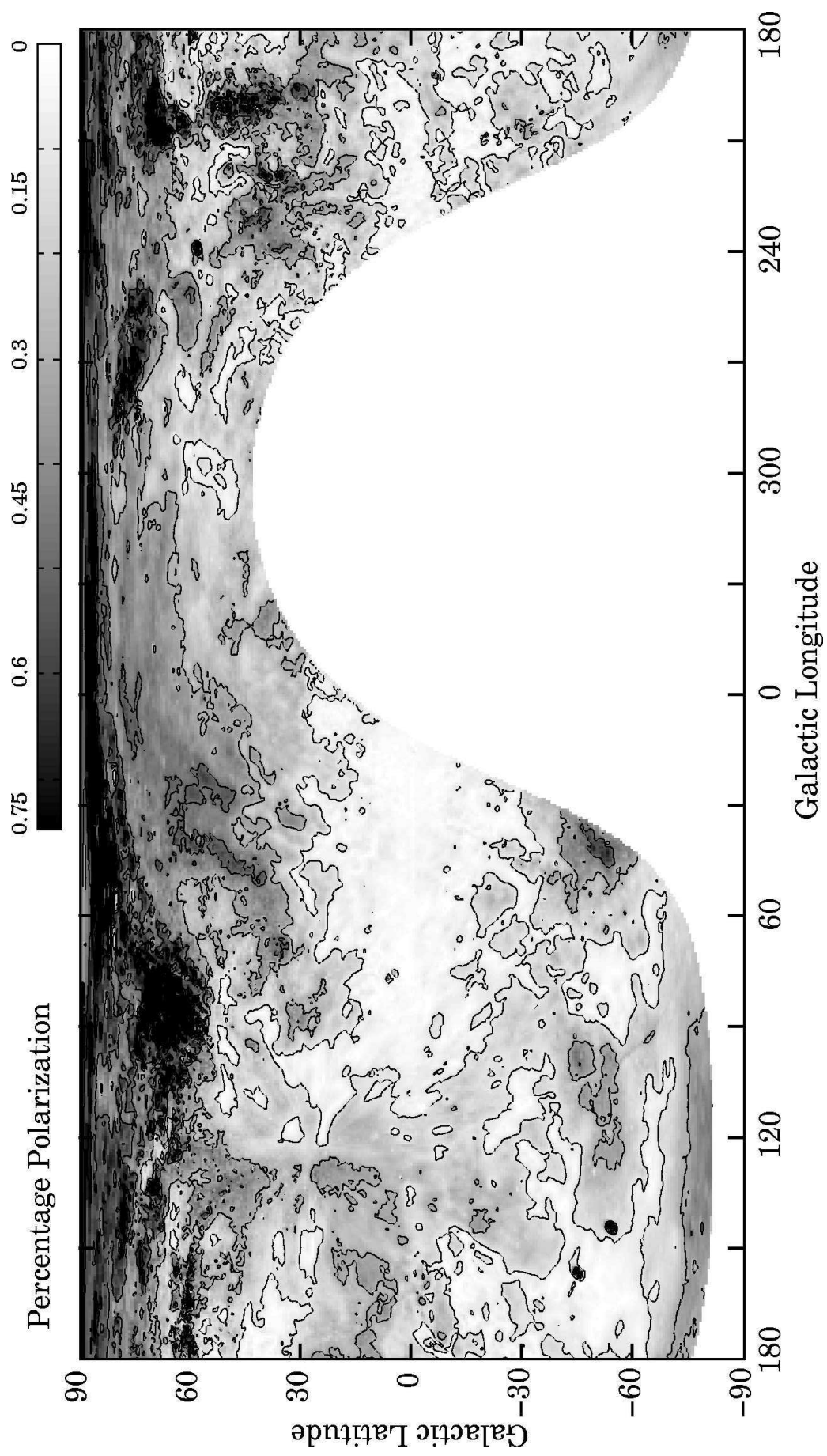
6 Improved Calibration of Effelsberg Medium Latitude Survey

In this chapter a preliminary map from the EMLS is absolutely calibrated using the 26-m Survey as well as data from the LDS. The gain in resolution of the new survey compared to the LDS allows a more accurate recovery of large-scale structures. This improves the quality of the calibration of the EMLS. In particular, high-resolution maps of polarized intensity and polarization angle show significant differences for different low-resolution data bases used for the absolute calibration.

6.1 Introduction

So far, the high-resolution polarimetric observations of the EMLS have been absolutely calibrated using the low-resolution LDS. Missing offsets due to large-scale structure were determined by comparing Stokes U and Q intensities of both surveys. In some areas surveyed by the EMLS it is possible to add missing structures by computing difference maps between EMLS and LDS, which requires interpolation of the Dwingeloo data and smoothing of the EMLS maps. In some areas, however, the coarse sampling of the LDS does not allow an accurate interpolation. Here, only a tentative calibration by adjusting offset levels in U and Q maps could be achieved.

As discussed in Section 1.2 an adequate calibration of diffuse polarized emission is necessary for the analysis. In the following the usability of the 26-m Survey for the absolute calibration of the EMLS is demonstrated using polarization maps of the Taurus, Auriga, and Perseus molecular cloud complex. The size of these maps is $40° \times 16°$ in $l \times b$. The final data are compared with tentatively calibrated maps, which are corrected on the basis of only a few data points available from the LDS.

6.2 Method

For the absolute calibration of the EMLS a calibration scheme has been developed as described in Reich et al. (1990). This algorithm compares data of different angular resolution and corrects the large-scale emission in the high-resolution data. The following steps of this method are most relevant here:

1. Convolution of the high-resolution map I_{highres} (EMLS: 9.4′ beam size) to the angular resolution of the low-resolution data I_{lowres} (Stockert, LDS: 36′ beam size):

$$I'_{\text{highres}} = I_{\text{highres}} \otimes \text{Gauss}(36' \text{ FWHM}). \tag{6.1}$$

   In case of total intensity maps, a removal of strong point sources may be necessary prior to convolution. Both surveys must be converted to the same temperature scale, e.g. main beam brightness temperature.

2. The difference map of the two data sets is added to the original high-resolution data:

$$I''_{\text{highres}} = I_{\text{lowres}} - I'_{\text{highres}} + I_{\text{highres}} \tag{6.2}$$

Thus, the extended emission in the I''_{highres} map is absolutely calibrated.

3. If point sources were subtracted they must be added now.

In a somewhat modified version of this procedure an additional background filter can be applied to both data sets to separate large-scale and small-scale components and perform the correction on the extended emission component only.

The EMLS map used for the comparison made here has been calibrated twice using the LDS and 26-m Survey. For the tentative calibration based on the LDS the above mentioned method could not be applied to the polarization data. Here, only the base level in the Q-map from the EMLS could be adjusted by adding an offset of 138 mK (Wolleben, 2001). The same maps were also calibrated using the 26-m Survey. Because of the improved sampling, the above described calibration method could be applied with the only difference that the convolving beam was 5° FWHM and that both, high-resolution and low-resolution data, were convolved.

6.3 Discussion

The 26-m Survey provides about 40 drift scans through this area in contrast to only 16 pointings from the LDS. The better sampling allows a much more accurate recovery of large-scale structures in the EMLS. Figure 6.1 and 6.2 show the EMLS maps, calibrated on the basis of the LDS and 26-m Survey, and the difference of both. Obviously, extended structures with brightness temperatures of up to 200 mK cannot be recovered by using the Dwingeloo data. This has a noticeable impact on structures in the map of polarized intensity and polarization angle, as visible in Figure 6.3.

Already a visual analysis of the absolutely calibrated polarization maps (Figures 6.1, 6.2, and 6.3) reveals significant differences of the morphological information contained.

- The absolute levels in Stokes U differ from −140 mK to 200 mK, depending on the low-resolution data used for the absolute calibration.

- In Stokes Q these differences reach values of −80 mK to 180 mK.

- The background level of polarized intensity changes from about 150 mK in the LDS based calibration to less than 100 mK in the 26-m Survey based calibration.

- The position and shape of some of the canal-like depressions in the polarized intensity map changes. Obviously, this type of objects is very sensitive to the calibration.

- Also, the extent and shape of the patch of increased polarized emission at $l = 170°$ and $b = −8°$ depends on the low-resolution data used for the calibration.

The morphological information in the final calibrated polarization maps of the EMLS obviously depends on the data set used for its absolute calibration. Clearly the appearance of some of the structures in polarized intensity and polarization angle changes, which may affect their interpretation. In this example, polarized intensities in the EMLS are generally lower if calibrated on the basis of the 26-m Survey. Also, some structures change from emission-like objects into objects of depressed polarized intensity and vice versa. Examples for this can be seen in Figure 6.3 towards:

$l = 176°$, $b = −16°$: The 26-m Survey based map shows a ring-like enhancement of polarized intensity with a diameter of ∼ 4°. The same feature in the LDS based map appears as a ring of depressed polarized intensity.

$l = 184°5, b = -15°$: The LDS based map shows a polarized feature with a diameter of $\sim 2°$. This feature almost completely vanishes in the 26-m Survey based map.

$l = 177°, b = -12°$: Pronounced canals of several degrees lengths are visible in the LDS based map. These canals disappear in the 26-m Survey based calibration.

These examples illustrate the importance of an accurate calibration of polarization data.
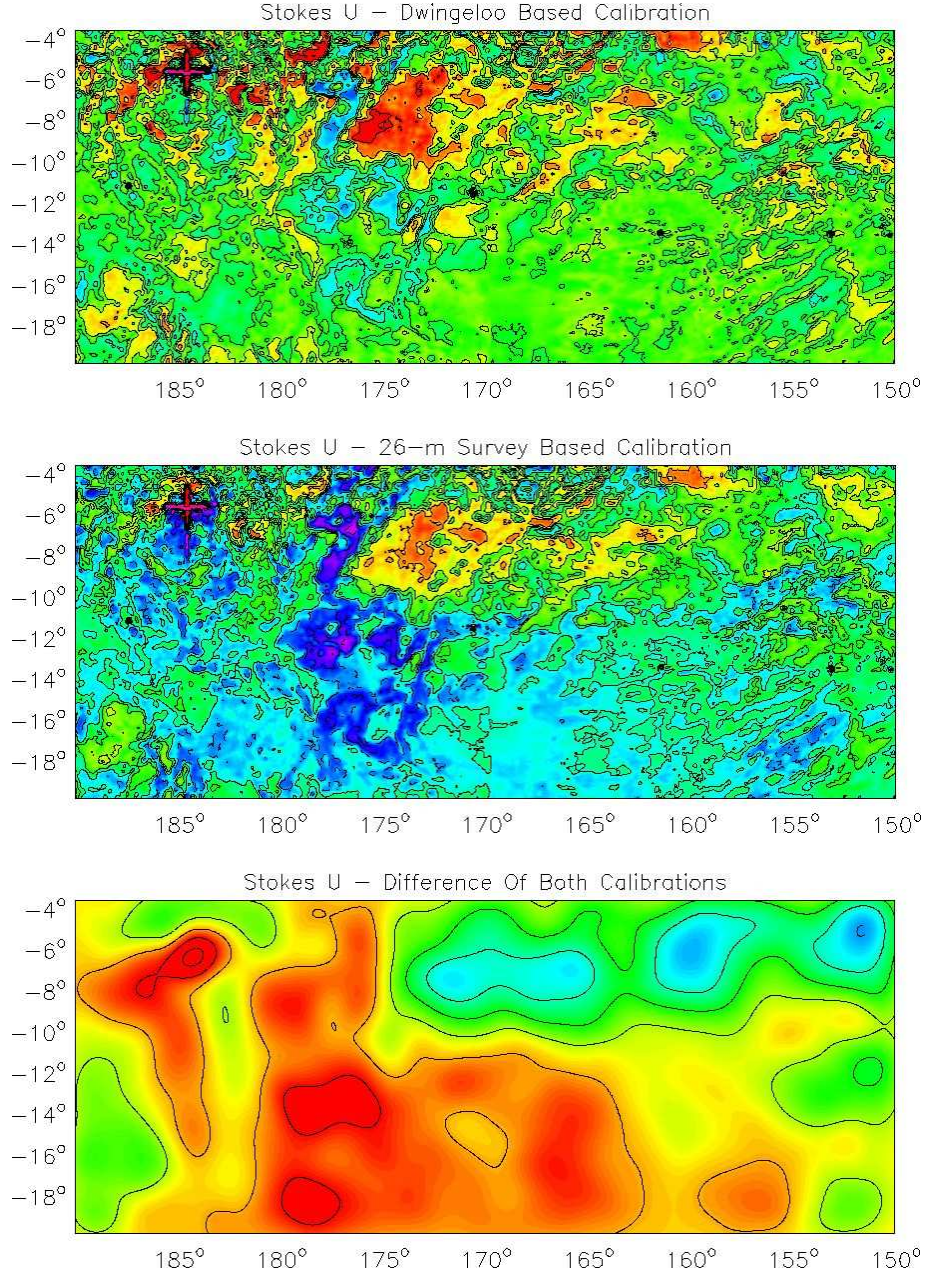
Figure 6.1: Stokes *U*: contours run in steps of 100 mK for the two upper images and in steps of 50 mK for the bottom image. Colour cuts are the same for the two upper images.
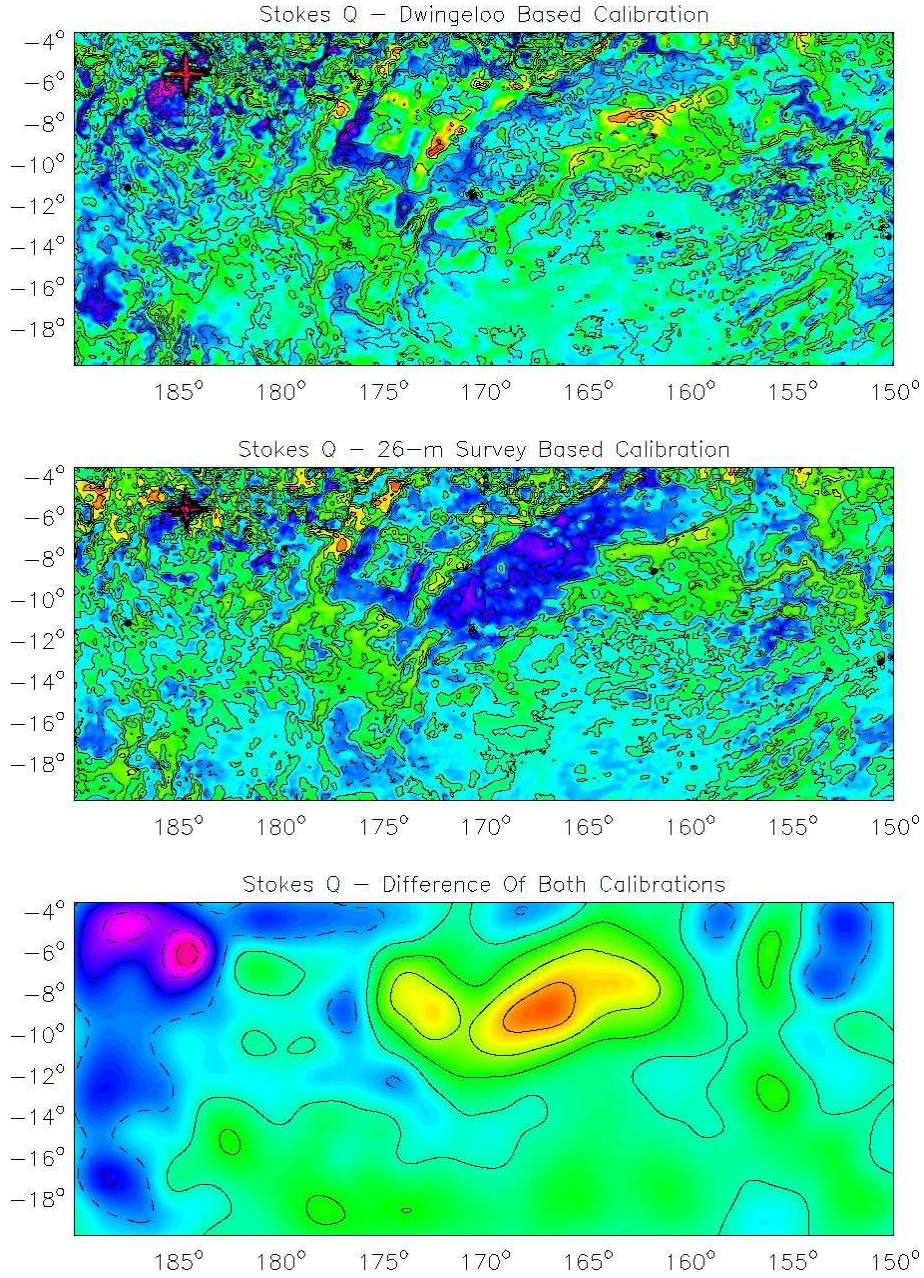
Figure 6.2: Stokes *Q*: contours run in steps of 100 mK for the two upper images and in steps of 50 mK for the bottom image. Colour cuts are the same for the two upper images. Dashed contours indicate negative *Q* values.
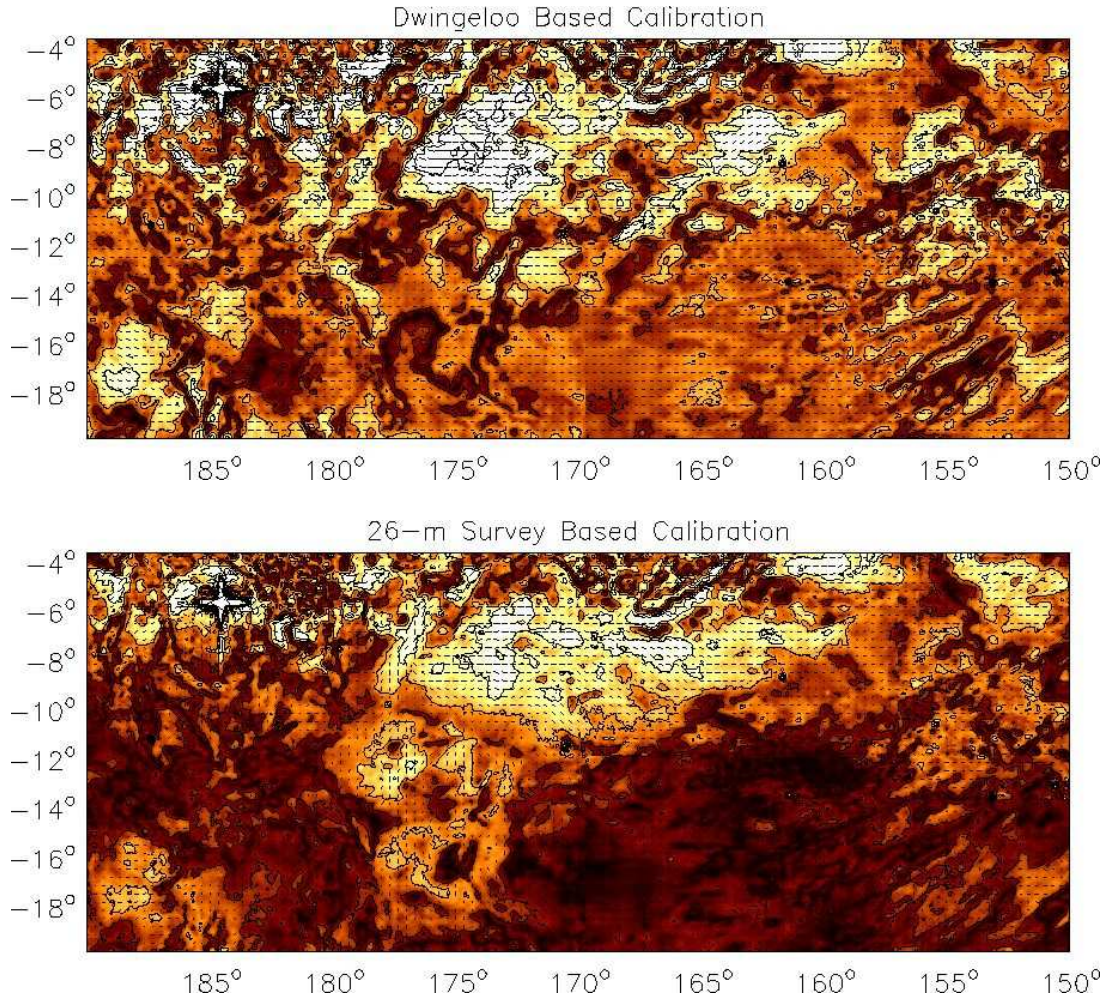
Figure 6.3: Polarized intensity maps of the Taurus, Auriga, and Perseus molecular cloud complex. Contours run from zero in steps of 100 mK. Colour cuts are the same for the two images.

7 Initial Data Analysis

An initial analysis of the 26-m Survey is presented. The map of polarized intensity shows many features and objects. The most pronounced of these are discussed below. Previously unknown features of polarized emission are identified for the first time and interpreted. This study provides new distance estimates to a prominent region of polarized emission, the fan-region, whose origin has been a puzzle since its first detection in the 1960's. An apparent lack of polarized emission towards the first Galactic quadrant is interpreted as due to depolarization. The analysis also reveals a possible new component of the local interstellar medium causing regular polarized emission at high Galactic latitudes.

7.1 Introduction

Polarized radio emission originates from Galactic synchrotron emission. But the observed intensity of the polarized emission often does not correlate with total intensity. Differential Faraday rotation affects the polarization angle and thus lowers the degree of polarization. Although detecting the same radiation, surveys of the polarized sky reveal a completely different picture of the Galaxy than in total intensity. It is this difference that attracts attention, because it allows the study of the magneto-ionic properties of the local interstellar environment. A high degree of correlation between polarized and total intensity is also interesting, because then, polarization vectors can be assumed to trace the Galactic magnetic field.

If, for a given line-of-sight, the physical rotation measure is zero no Faraday rotation takes place. In this case, the B-vector of the polarized emission is parallel to the projected direction of the magnetic field that gives rise to synchrotron emission. If the synchrotron emission is generated by different "layers" of tangled magnetic fields, the observed integral of polarized emission is reduced, because the superposition of differently oriented polarization vectors leads to a degree of polarization smaller than the theoretical maximum of about 72%.

If Faraday rotation takes place along the line-of-sight, different depolarization mechanism may reduce polarized intensity. In the following, depolarization is defined as DP $= p/p_i$, where p and p_i are observed and intrinsic degree of polarization, respectively, so that low values of DP mean strong depolarization. Basically, the depolarization mechanism can be generalized into two cases:

1. "Beam depolarization" occurs if the polarization angle fluctuates across the telescope beam. These fluctuations may be intrinsic to a turbulent magnetic field generating the synchrotron emission, or due to stochastic Faraday rotation within the ionized medium. If N is the number of coherent regions or cells observed by the beam, according to Burn (1966) the degree of depolarization is:

$$\mathrm{DP} = \frac{1}{\sqrt{N}}. \tag{7.1}$$

2. "Internal Faraday dispersion" occurs if Faraday rotation and synchrotron emission takes place within the same volume. Then, polarization vectors originating from the far side of this volume are rotated more than emission from the near side, and the superposition results in a decreased
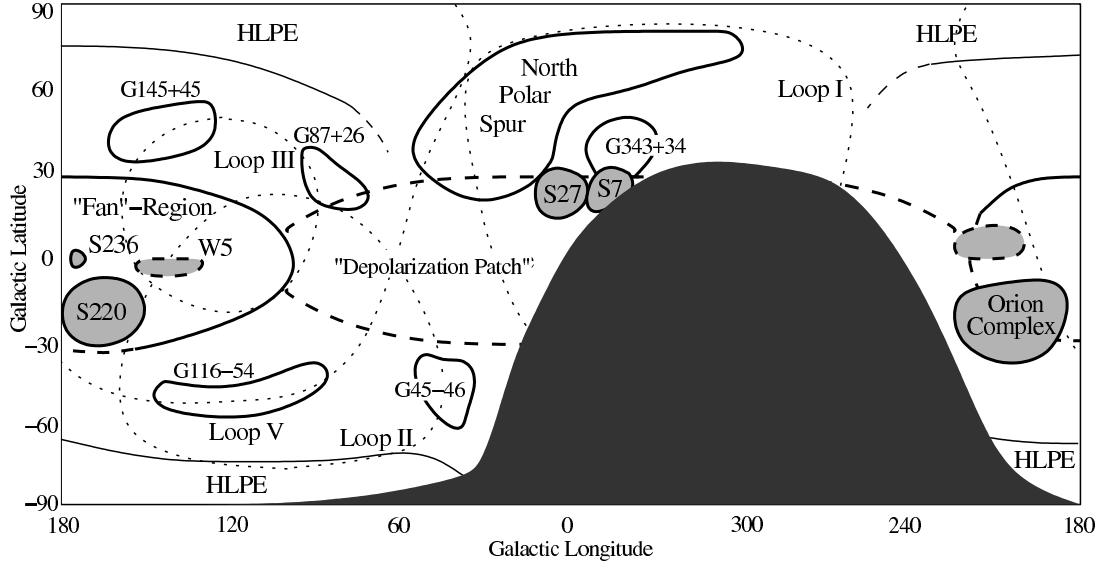
Figure 7.1: The sketch outlines prominent features in the polarized intensity map. In grey H II-regions that cause depolarization are displayed. Thick contours indicate bright features in polarized intensity. Thin lines indicate contours of the HLPE. The Depolarization Patch is indicated by thick dashed lines. The circles of the radio loops (Loop I, II, III and V) are drawn with dotted lines. Parameters of these loops are those computed by Milogradov-Turin & Urosevic (1997).

degree of polarization. Burn found:

$$\langle \mathrm{DP} \rangle = \left(1 - \exp\left(-S \right) \right) / S, \tag{7.2}$$

with $S = \sigma_{\mathrm{RM}}^2 \lambda^4$; σ_{RM} is the dispersion in rotation measure. This mechanism is also called depth depolarization.

This listing neglects bandwidth depolarization, which is only important in case of extreme high values of several hundreds of $\mathrm{rad}\,\mathrm{m}^{-2}$ of interstellar RM at 1.4 GHz. Such high RMs are not observed in the Dwingeloo surveys so that bandwidth depolarization can be neglected here. A more detailed description of depolarization mechanisms is given in Burns paper.

7.1.1 Large-Scale Morphology of Polarized Emission

Looking at the polarized intensity map obtained with the 26-m Survey numerous features in the polarized sky can be identified. These features appear as enhancements or depressions of polarized intensity. Some of them have counterparts in total intensity and some do not. In the following the most pronounced features are classified and discussed.

Enhanced Polarized Emission

A number of bright patches of polarized emission with intensities between 100 mK and 700 mK, exceeding the general "background" level[1] of $\sim$ 60 mK, are visible in the polarized intensity map. The size of these features ranges from less than one degree up to several tens of degrees. Some can be associated with known Galactic objects. At high Galactic latitudes, a previously unknown general increase of diffuse polarized intensity is noted: the so called "High Latitude Polarized Emission" (HLPE hereafter). The most pronounced objects, which are also outlined in Figure 7.1, are:

(a) The North-Polar Spur

A bright and spatially extended arc of polarized emission can be seen from $l = 305°$ to $l = 50°$, and $b = 30°$ to $b = 80°$. Good correlation between polarized and total intensity is found. The new data reveal a previously unseen filamentary structure in its polarized emission. The North-Polar Spur emission can be associated with Loop I. Its percentage polarization is about 47% to 57%. See Section 7.2.1 for futher discussion.

(b) G343+34

This circular patch, about 15° in diameter, is located within the projected circle of Loop I. The average polarized intensity of this feature is about 300 mK with maximum intensities of about 450 mK. This structure may be associated with the North-Polar Spur as its polarization angles follow the circular pattern of Loop I. To the south, the emission seems to be depolarized by the two H II-regions S7 and S27. See Section 7.2.1 for futher discussion.

(c) The Fan-Region

The spatially extended polarized region of roughly $80° \times 50°$ extent, centred at about $l = 150°$ and $b = 0°$ is commonly referred to as the "fan"-region. The percentage polarization towards this region reaches values of 40%. The average polarization is about 26%. See Section 7.2.2 for futher discussion.

(d) High Latitude Polarized Emission

The 26-m Survey reveals an increase of polarized intensity towards the Galactic poles at latitudes $|b| \gtrsim 70°$. Polarized intensities rise from values of around 50 mK ($60° < |b| < 70°$) to values of 110 mK ($b > 70°$), and 230 mK ($b < -70°$), respectively. The percentage polarization is $\sim$ 65% for the northern component and 40% for the southern counterpart of the HLPE. See Section 7.3.3 for futher discussion.

(e) G45-46

Because of its positional coincidence and reasonable agreement of the B-vectors with the circle of Loop II, the polarized intensity enhancement of about 200 mK over a region of about 15° in diameter, centred at $l = 45$ and $b = -46°$, may be related to polarized emission from Loop II.

(f) G87+26

The feature at $l = 87°$ and $b = 26°$ with mean polarized intensity of about 160 mK seems to be part of Loop III. The B-vectors of the polarized emission follow the corresponding circle.

---

[1]The background level of polarized intensity is determined at medium Galactic latitudes ($40° \lesssim b \lesssim 70°$ and $-70° \lesssim b \lesssim -40°$, respectively), excluding emission from bright polarized features.

(g) G116-54

The intensity and angle of polarized emission of this elongated feature at $l = 116°$ and $b = -54°$ are well aligned with Loop V. The polarized intensity of this object is about 130 mK.

(h) G145+45

Because of the present incomplete sampling of the 26-m Survey at high declinations ($\gtrsim 80°$) the polarized feature at $l = 145°$ and $b = 45°$ seems to be distorted in the map. The polarized intensity is about 110 mK and may be associated with Loop III.

Decreased Polarized Emission

Depressions in polarized intensity are observed toward a number of H ɪɪ-regions. The most obvious anticorrelations between Hα emission and polarized intensity are listed below, a more complete list is given in Table 7.1. The pronounced area of general low percentage polarization towards the first quadrant of the Galaxy will be denoted as the "Depolarization Patch".

(a) The Depolarization Patch

Very low percentage polarization around 3% over an elongated area towards the first quadrant of the Galaxy is observed in the 26-m Survey. The limits of the Depolarization Patch in Galactic latitude are remarkebly clear. At longitudes around $l \approx 0°$ the northern and southern boundaries of which are quite symmetric at about $|b| \approx 30°$. At longitudes from $\sim 60°$ to $\sim 90°$ the latitude extent of the patch is less confined within $|b| \lesssim 25°$. The limits in longitude are not as obvious. The patch seems to extend to longitude $\sim 100°$, covering an area of roughly 4000 square degrees on the northern sky. At around $l \approx 220°$, low percentage polarization at $|b| \lesssim 20°$ suggests continuation of the Depolarization Patch into the fourth quadrant. Although previous polarization surveys cover the region specified here, its appearance as a coherent lack of polarization has never been noted.

(b) Sh2-7

The exciting star of the H ɪɪ-region S7 is δ Sco, which belongs to the Upper Scorpius association, the youngest subgroup of the Scorpio-Centaurus OB association. The distance to this complex is 125 pc (de Geus & Burton, 1991). The average polarized intensity is 20 mK toward this object, while it is ~ 300 mK in its surrounding.

(c) Sh2-27

S27 is the H ɪɪ-region around the early-type star ζ Oph at a distance of about 170 pc (Fich et al., 1989). The average polarized intensity toward S27 is 30 mK and ~ 250 mK in its surrounding.

(d) Sh2-199

This H ɪɪ-region is associated with W5. Although this object is covered by only one drift scan of the 26-m Survey the decrease of polarized emission is significant. This sets a lower limit to the distance of the fan region as discussed in Section 7.2.2.

(e) Sh2-220

The California Nebula (S220) is a relatively large and close (∼ 400 pc) H ɪɪ-region located in the local spiral arm. The polarized intensity toward S220 is 40 mK, compared to ∼ 220 mK to the east and north of this object.

(f) Sh2-236

The H ɪɪ-region S236 is covered by four drift scans of the 26-m Survey, which show an anticorrelation between Hα emission and polarized intensity for this object. This anticorrelation can also been seen in the EMLS (W. Reich, priv. comm.) strengthening evidence that this H ɪɪ-region is acting as a depolarizing Faraday screen. As for S199 this sets a lower limit to the distance of the fan region. Toward S236 the polarized intensity is 100 mK and it is ∼ 210 mK around it.

(g) Orion Complex

The Orion complex seems to act as a depolarizing screen, although it is not as obvious as for the other H ɪɪ-regions. The brightest objects of the Orion complex, such as M42, M43, Barnard's Loop, and the Horsehead Nebula region, seemingly leave imprints in the background polarization structure. Additionally, some of the filamentary structure of the Orion complex up to $b \approx 0°$ obviously depolarizes background emission.

7.1.2 Local Interstellar Medium

Most of the objects visible in polarized intensity are strongly organized features of large angular extent suggesting a rather local origin. Because of depolarization and Faraday rotation the diffuse polarized emission is affected by the local ionized medium.

The region around the Sun within a radius of 150 to 200 pc is generally termed as the local interstellar medium (LISM). The environment of the LISM is shaped by the influence of local objects such as Loop I or the close SCO-CEN stellar association ($l = 330°$, $b = +15°$, at 170 pc distance, Bertiau, 1958). Part of the LISM is the Local Bubble, an elongated cavity, largely devoid of H ɪ with an average radius of 100 pc. Because of the observation of an ultrasoft X-ray background, the local cavity is believed to be filled with hot plasma (e.g. Freyberg & Breitschwerdt, 2001). The Sun is embedded at the inner edge of the Local Interstellar Cloud, a single entity within the Local Bubble.

The origin and evolution of the Local Bubble is still being discussed. Possible explanations propose a supernova remnant that has expanded to about 100 pc, or a recently heated superbubble produced by an already dissolved stellar association (see e.g. Cox & Reynolds, 1987).

Because of the spatial coincidence of the Local Bubble and Loop I, it is very likely that the two have undergone some kind of interaction. Hydrodynamical computations show that a collision or merging of the two bubbles would leave a signature in the neutral hydrogen density. And, in fact, such an H ɪ-ring located roughly in the direction of the Galactic centre has been identified (Egger & Aschenbach, 1995). The distance to this ring and thus to the possible interaction region is 70 pc.

A number of radio spurs that can be joined into large circles on the sky are revealed by total intensity surveys. A set of spurs belonging to the same hypothetical structure is named a "loop". Four major radio loops are generally recognized. These are Loop I (Large et al., 1962; Haslam et al., 1964), which has an intriguing filament called the North-Polar Spur, Loop II or Cetus arc (Large et al., 1962), Loop III or North-Celestial Pole Loop (Quigley & Haslam, 1965) and Loop IV (Large et al., 1966). The geometrical parameters of these loops were published by Berkhuijsen et al. (1971). Later, Milogradov-Turin & Urosevic (1997), who also proposed Loop V, used the continuum survey at 1420 MHz (Reich, 1982; Reich & Reich, 1986) for a re-computation of the parameters. Their results agree well with the
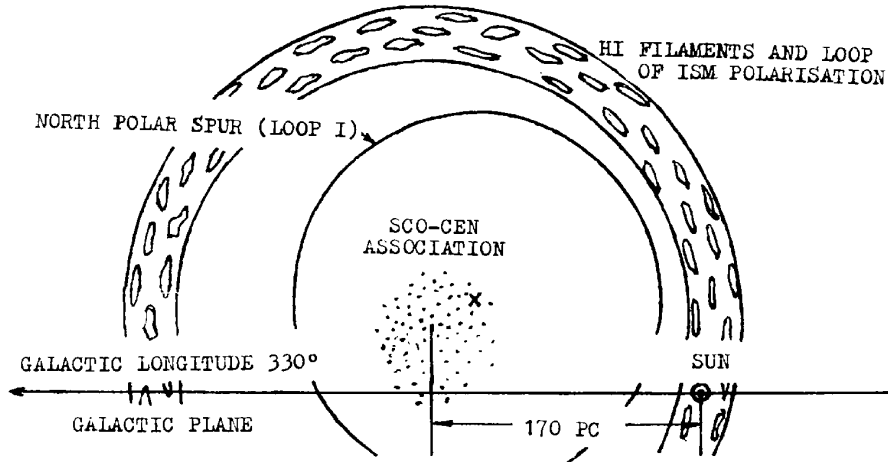
Figure 7.2: Structure of the LISM according to Weaver (1979). The Galactic plane is perpendicular to the page. This figure is taken from Bochkarev (1987, Fig. 1).

parameters computed on the basis of the lower frequencies, confirming that the centres of the loops are independent of frequency.

The continuum emission of some of the spurs was found to be associated with neutral hydrogen and X-ray emission. In particular, filaments or features of Loop I have been found to closely coincide with similar H I features. The velocities at which continuum spurs of Loop I correlate with H I are less than 30 km/s at low latitudes and between -10 and -30 km/s at high latitudes, suggesting a large velocity dispersion. X-ray emission in the energy band between 100 eV and 1.6 keV has been found to correlate with Loop I (Salter, 1983). Also for Loop III and Loop IV possible H I counterparts were reported (Heiles, 1967). No H I associated with Loop II has been noted so far.

Several proposals on the nature of the loops were made. The two widely accepted ones are:

1. Based on the evidence for neutral hydrogen associated with the loops, Berkhuijsen et al. (1971) hypothesized that the loops are supernova remnants (SNR). The spurs would thus be the brightest segments of SNR shells. Criticism for this hypothesis involve the high degree of circularity of the loops, which seems unlikely when the supernova shell expands into a gas density gradient resulting in a distortion of the spherical symmetry. Another point of criticism is the statistical unlikeliness for such events to occur so frequently in the solar neighbourhood. This problem can only be solved if the loops were old, slowly expanding SNRs.

2. In a different and less accepted approach Kafatos & Morrison (1973) proposed that the loops are fossil Strömgren spheres induced by radiation from a supernova event, rather than being formed by supernova ejecta. In their model, Alfven waves or a shock generated by the shell expansion compresses the adjacent magnetic field enhancing the local synchrotron emission. In their theory, however, the X-ray emission would be produced by the synchrotron process. This seems incompatible with the observed spectrum of the X-rays of the North-Polar Spur, which seems to be quite consistent with that expected from a thermal plasma and not with the power-law expected from synchrotron radiation.

According to the model of Weaver (1979), the local Galactic environment towards $l = 330°$ is formed by interstellar material left-over from the formation of the SCO-CEN association. Strong stellar winds inflated a large bubble of gas and dust concentric with the SCO-CEN stellar group. Hence, observed

arcs in H I and dust emission are located on the surface of the expanding bubble, which has a diameter of approximately 300 pc (see Figure 7.2).

In this bubble model, Loop I is a supernova shell produced by the explosion of one of the members of the SCO-CEN association. This supernova shell expands inside the bubble and encounters the H I at the surface. The interaction zones produce filaments of the Loop I, whereas observed arcs of H I and dust are not associated with the SNR but are rather parts of the bubble itself.

More detailed papers about models of the LISM have been frequently published by several authors. Extensive reviews on the LISM are published by e.g.: Cox & Reynolds (1987); Bochkarev (1987); Egger et al. (1996); Ferlet (1999).

7.2 Most Pronounced Objects in Polarization

In the northern sky the two most pronounced objects in polarized intensity are the North-Polar Spur and the fan-region. These were clearly detected already in the early polarization surveys. The 26-m Survey allows a more detailed view.

7.2.1 North-Polar Spur and Loop I

The North-Polar Spur is the brightest continuum ridge of Loop I. Its filamentary and arc-like structure is known since the first radio continuum surveys of total intensity emission were made. The centre of Loop I is at $l = 328.3°$ and $b = 17.6°$, and its radius is $r = 59°$, determined with an accuracy of $\pm 2°$ (Milogradov-Turin & Urosevic, 1997). The distance to the continuum emission of the North-Polar Spur is 100 pc (Willingale et al., 2003). A detailed review about the North-Polar Spur is published by Salter (1983).

So far, the most detailed view of the North-Polar Spur in polarization has been provided by the Leiden-Dwingeloo polarization surveys. These data, because of their coarse sampling, could only confirm the high degree of polarization of the North-Polar Spur, but did not allow detailed studies of its structure. Studies of its percentage polarization were made by e.g. Berkhuijsen (1971) and Spoelstra (1971). Basically, the 26-m Survey confirms the high percantage polarization found in these investigations.

The 26-m Survey reveals a large number of previously unseen filaments and arcs in polarization most likely associated with the North-Polar Spur. These are displayed in Figure 7.3. Most of these filaments have counterparts in total intensity. It is noted that not all of these filaments can be joined into circles with equal centre. Especially the two large arcs at $b \approx 70°$ and $b \approx 78°$ give different centres if fitted by large circles. This may indicate the presence of multiple loops with small differences of their centres.

The newly discovered bright emission patch G343+34 is at low declinations and therefore not covered by the Leiden-Dwingeloo surveys. The B-vectors of its polarized emission roughly follow the circle of Loop I, suggesting that this feature is another spur of Loop I. The obvious depolarization of its polarized emission due to the two H II regions S7 and S27 places this object at a distance larger than 125 pc (S7), and 170 pc (S27), respectively.

Assuming that G343+34 is part of Loop I and according to the model of Weaver, its emission would then originate from the far side of the Loop I shell, behind the two H II-regions. Consequently, the polarized emission observed towards the H II-regions must be generated at the near side of Loop I. The polarized intensity toward S7 and S27 is 20 to 30 mK, which is about ten times less than that of G343+34. This may indicate that less polarized emission is received from the near side of Loop I than from its far side.
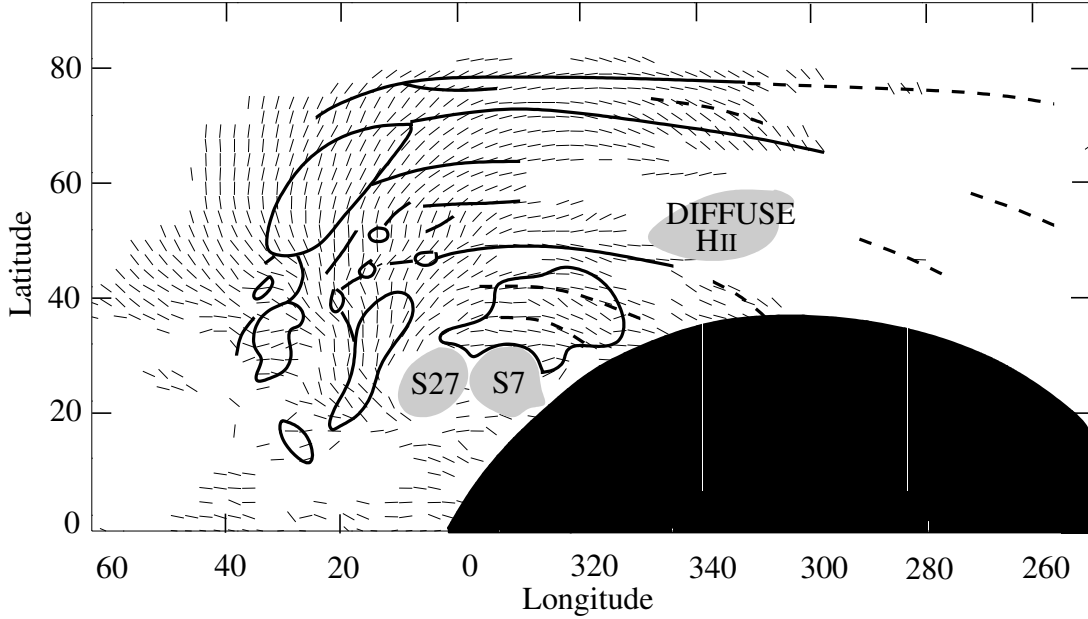
Figure 7.3: Sketch highlighting the filaments of the North-Polar Spur with B-vectors of polarized emission at 1.4 GHz overlayed. The shadowed areas are regions of enhanced Hα emission. Vectors of equal length are shown for PI $\geq$ 140 mK. Solid lines mark contours of filaments in the polarized intensity map, whereas dashed lines indicate less confined filaments.

7.2.2 The Fan-Region

The fan-region is an extended area with strong polarized intensity and high percentage polarization. Its centre is commonly quoted at $l = 140°$ and $b = 5°$. The increase in sensitivity and sampling of the 26-m Survey, however, reveals a larger extent of the fan-region then previously believed. Therefore, a revised size and position is claimed. If the centre of the whole structure is taken, instead of the location of the maximum of polarized intensity, the centre is roughly at $l = 150°$ and $b = 0°$. The spatial extent is several tens of degrees in diameter, covering an area of about 4000 square degrees.

The high degree of polarization towards the fan-region was noted by Westerhout et al. (1962) and Brouw et al. (1962) who used the Dwingeloo-telescope at 408 MHz. Measurements of Wielebinski et al. (1962), made at Cambridge at the same frequency, and Razin et al. (1968)) at Staryi Pustyn at 437 MHz, 510 MHz, and 735 MHz comfirmed these results. The 26-m Survey also clearly shows that, at 1410 MHz, the fan-region is one of the two brightest polarized patches in the northern sky with polarized intensities of up to 500 mK.

The E-vectors of the polarized emission of the fan-region are highly ordered and perpendicular to the Galactic plane, indicating a magnetic field parallel to the plane. A comparison of radio polarization data with optical data confirms that the strong polarized emission may be due to a magnetic field parallel to the Galactic plane and perpendicular to the line-of-sight towards $l = 140°$ (Berkhuijsen et al., 1964; Bingham & Shakeshaft, 1967). This is in agreement with low Faraday rotation observed in this area (Spoelstra, 1984).

A constraint for the distance to the fan-region on the basis of starlight polarization was suggested by Spoelstra (1984). He concluded that the polarized emission must come from distances within about 450 pc and thus traces very local synchrotron radiation.
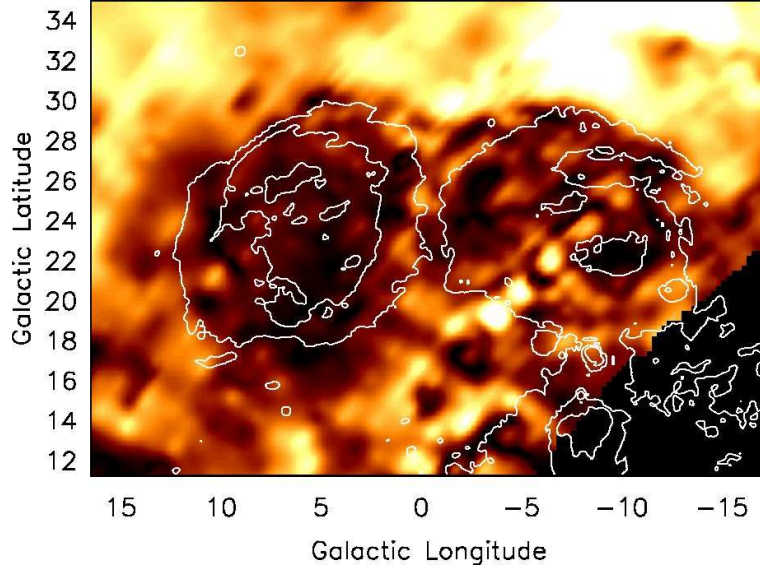
Figure 7.4: Depolarization at the southern edge of the emission feature G343+34 caused by the two H II-regions S27 (left) and S7 (right). The map shows polarized intensity (26m-Survey) with contours of Hα emission (Finkbeiner, 2003) overlayed.

Morphological studies of the fan region have been fairly limited because of the sparse sampling of the early polarization surveys. Reasonably sampled data of the fan region at 408 MHz were analyzed by Verschuur (1968) and Wilkinson & Smith (1974) who studied the depolarizing effects of H II-regions located towards the fan-region.

Verschuur found a ring-like structure of low polarized intensity at 408 MHz towards $l = 137°\!.4$ and $b = 7°\!.1$, which he interpreted as due to depolarization or Faraday rotation. He suggested that enhanced RM is caused by a magneto-ionized medium associated with the Strömgren sphere around the B2 star HD 20336 and causing depolarization. Its position, in fact, coincides with the centre of the depolarization ring. The distance to HD 20336 is 140 to 200 pc (see references in Verschuur, 1968). Rubin et al. (1962) give a distance of 400 pc to this star. Verschuur concluded that most polarized radiation must originate from distances larger than that of HD 20336.

Wilkinson and Smith looked at a number of H II-regions that should show similar effects like the B2 star HD 20336. They did not find such effects towards the H II-regions S202, S185, S205 and S216. From the absence of depolarization they concluded that most polarized radiation towards the fan region originates within a distance of about 500 pc (±200 pc).

These two studies and the investigation of RMs made by Spoelstra suggested a distance to the fan-region of less then 500 pc and more then about 200 pc. According to these results the fan-region is a layer of enhanced polarized emission, which could be due to enhanced synchrotron emissivity and a particular regular magnetic field perpendicular to the line-of-sight causing only little depolarization compared with other directions. Based on the new data from the 26-m Survey the distance to the fan-region can be revised, because depolarization observable towards a number of H II-regions reveals a larger distance to this object. This is discussed in the following.

Table 7.1: List of H II regions visible in polarization.

name	alt. name	l (deg)	b (deg)	dist. (kpc)	anti-corr.
Sh2-117	North America Nebula	85.6	−0.9	0.8 ± 0.3 [2]	moderate[1]
Sh2-119	LBN 087.23-03.80	87.6	−3.9	0.7 ± 0.25 [2]	moderate[1]
Sh2-124	LBN 094.79-01.77	94.4	−1.6	2.6 ± 0.6 [2]	weak
Sh2-137	LBN 105.48+07.80	105.8	7.8	0.6 ± 0.2 [2]	weak[1]
Sh2-160	LBN 112.52+03.75	112	4	0.9 ± 0.3 [3]	weak[1]
Sh2-190	IC 1805	134.8	0.8	2.1 ± 0.2 [2]	moderate
Sh2-199	IC 1848	137.5	1	2.1 ± 0.2 [2]	moderate
Sh2-203	LBN 143.37-02.20	143.5	−1.8		moderate
Sh2-220	California Nebula	160.1	−12.1	0.4 ± 0.04 [2]	strong
Sh2-229	DA 167	172	−2.3	0.51 ± 0.15 [3]	weak
Sh2-236		173.5	−1.8	3.2 ± 0.3 [2]	moderate
Sh2-248	SNR 189.1+03.0	189	3		moderate[1]
Sh2-249	LBN 841	189	4	1.6 ± 0.5 [2]	moderate[1]
	Orion Complex	210	−15	0.4-0.8	moderate

[1] Object is part of a larger complex which shows an anticorrelation with polarized intensity.

[2] Fich et al. (1989)

[3] Fich & Blitz (1984)

7.3 Newly Detected Polarization Features

The 26-m Survey reveals some previously unknown features in the polarized sky at 1.4 GHz. In particular these are: a number of depolarizing H II-regions, a lack of polarized emission probably caused by strong depolarization in the first Galactic quadrant, and polarized emission at high Galactic latitudes.

7.3.1 Depolarizing H II-Regions

H II-regions are believed to act as depolarizing Faraday screens. The high electron density within these regions of ionized hydrogen, along with low volume filling factors, results in strong and stochastic Faraday rotation of the polarized emission passing through the screen and thus to beam depolarization. If polarized emission originates behind local H II-regions the depolarization should leave a visible signature in polarization. It is still uncertain, however, to which level H II-regions cause depolarization and whether all H II-regions show this effect. Moreover, it is not clear how magnetic fields evolve and remain inside H II-regions.

A simple visual comparison of polarized intensity and the H-alpha map of Finkbeiner (2003) revealed a number of H II-regions acting as depolarizing Faraday screens. Table 7.1 gives a list of objects found as depressions of polarized intensity. Figure 7.5 shows polarized intensity and Hα emission of scans through these objects. The most striking anti-correlations were found for Sh2-220 (Figure 7.6), Sh2-229, Sh2-236 (Figure 7.7), and the Orion Complex (Figure 7.7).

The depolarizing H II-regions can be used to derive lower distance limits to the polarized background emission. For most of the H II-regions, spectroscopic distances are known. About half of them can be placed in the local arm. However, some H II-regions have distances of 2 kpc and more. These are clearly Perseus arm objects. As depolarizing Faraday screens can only cause effects on synchrotron radiation originating behind the screen, some of the polarized emission making up the fan region must originate in or beyond the Perseus spiral arm.

As some of these H II-regions are strong sources of continuum emission at 1.4 GHz (~ 4 K towards
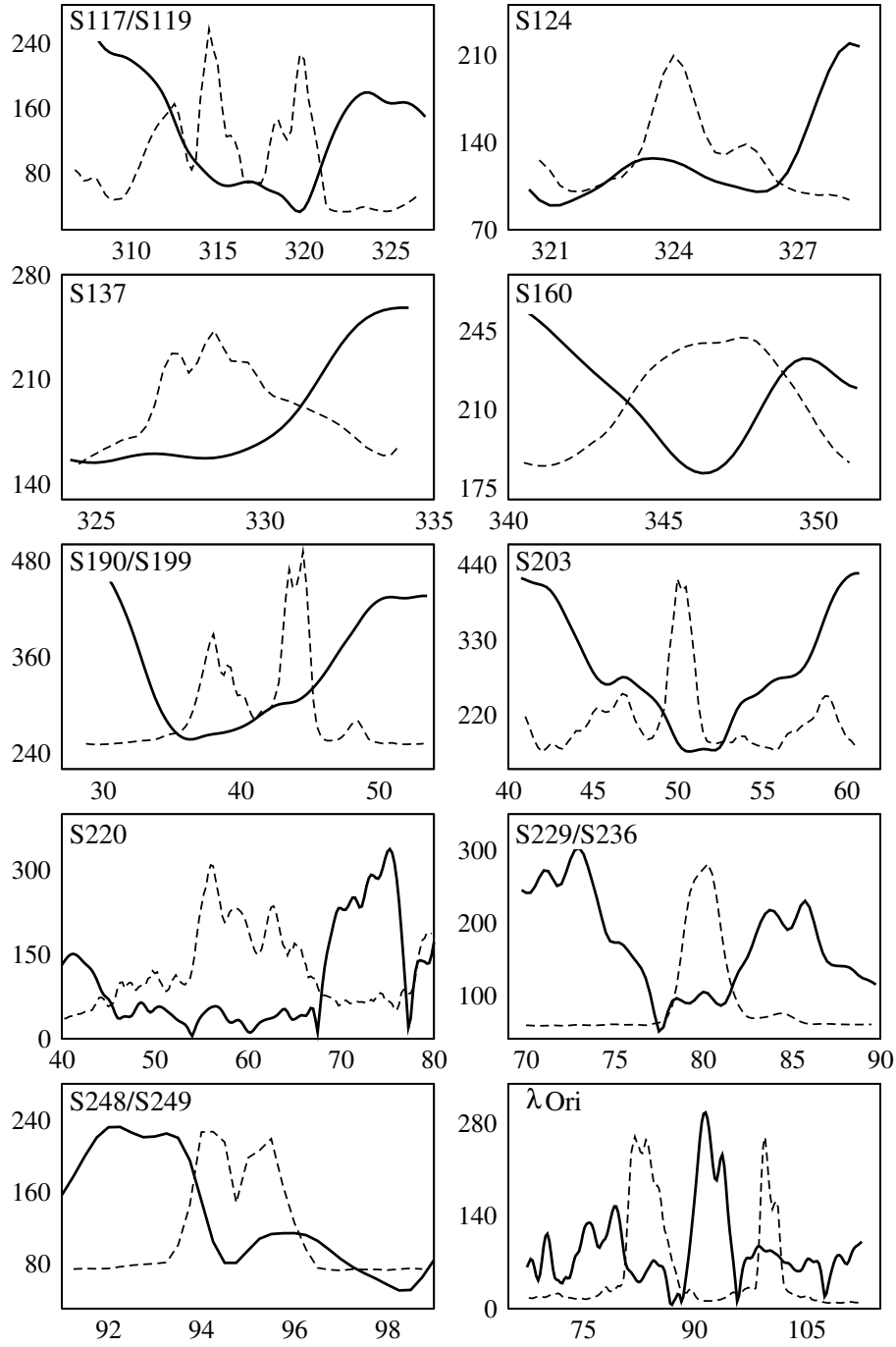
Figure 7.5: Drift scans through H II regions located towards the fan region. Plotted is polarized intensity (thick line) and Hα emission taken from the map of Finkbeiner (dashed line). Axes are right ascension (abscissa) in degree and polarized intensity (ordinate) in mK. The data have been convolved to match the same angular resolution.
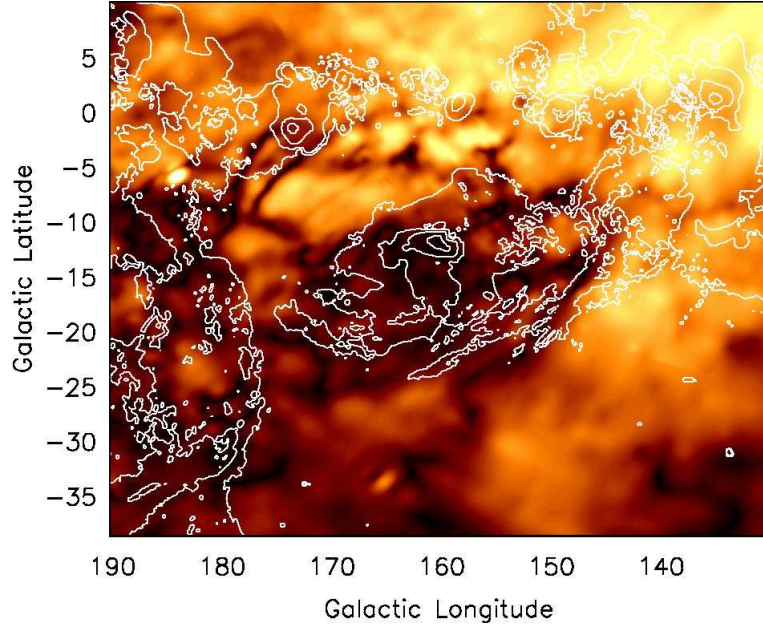
Figure 7.6: Polarized intensity towards the California nebula (SH2-220). Contours show Hα emission.

S117, ~ 2.1 K towards S248, ~ 2.7 K towards S190, and ~ 1.3 K towards S199) it is important to consider remaining instrumental polarization as cause for the depressions of polarized intensity. However, 9 of the H II-regions discussed here are relatively weak radio emitters ($\lesssim$ 0.8 K) at that frequency so that instrumental polarization can be ruled out for these. Four of these weak objects (~ 0.8 K towards S236, ~ 0.7 K towards 249, ~ 0.4 K towards S124, and ~ 0.1 K towards S160) are at distances of 0.9 kpc and more.

Also, 7 candidates for O-stars whose Strömgren spheres are possibly visible as depressions in polarization can be found towards the fan-region. The effects, however, are less obvious than for the H II-regions and the anti-correlations are therefore rather uncertain (Figure 7.8). Ring-like depression in the polarized intensity map around HD 36483 (O9.1V, 1.13 kpc) and HD 34656 (O7.1, 2.75 kpc) are found. Although the resolution toward the group of three stars HD 256035 (O9V, 1.5 kpc), HD 255055 (O9Vp, 2.48 kpc), and HD 254755 (O9V, 1.23 kpc), and the single stars HD 37366 (O9.5V, 1.32 kpc) and HD 219286 (O9, 1.06 kpc) is too low to reveal rings in the polarized intensity map, close depressions may indicate ongoing depolarization. Additionally, in the first quadrant, a depression of polarized intensity is found toward HD 175514 (O8V, 1.2 kpc). The here quoted distances for these stars are those determined by Cruz-Gonzalez et al. (1974).

7.3.2 The Depolarization Patch

The Depolarization Patch is a region of low polarized emission and percentage polarization, characterized by small, chaotic structures in the map of polarized intensity and polarization angle. The observation of such low polarized intensities is surprising as the line-of-sights toward this patch run through the inner Galactic plane resulting in intense total power emission in the first and fourth quadrant.

The low degree of polarization suggests that strong depolarization destroys the intrinsic polarization. Otherwise the Galactic magnetic field must be tangled, which would be in contrast to studies proposing
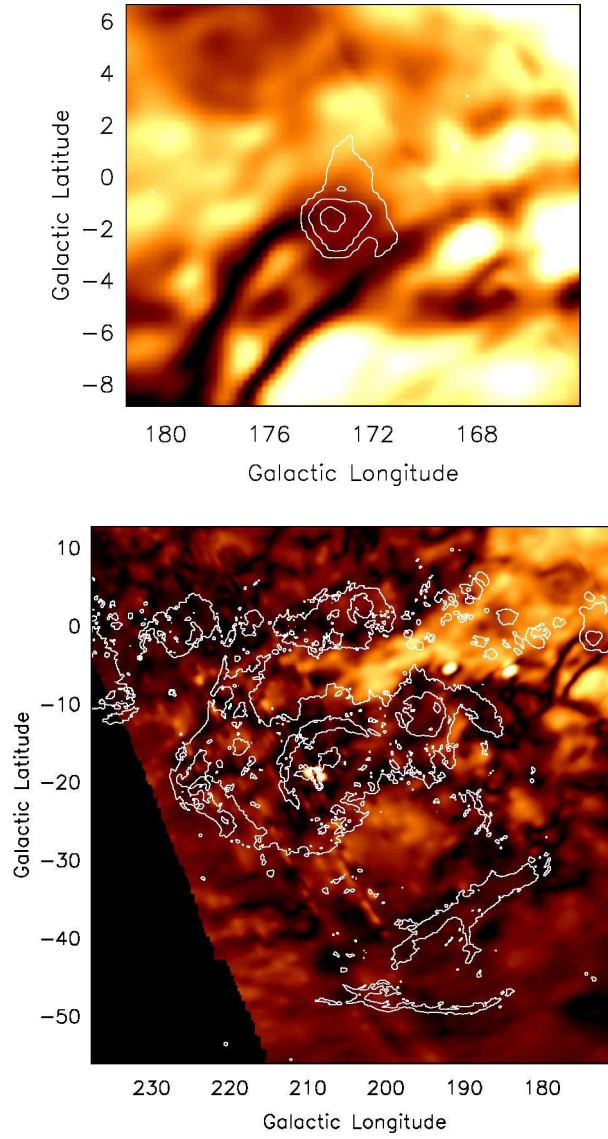
Figure 7.7: Left panel shows polarized intensity towards Sh2-229 and Sh2-236. Right panel shows polarized intensity towards the Orion complex. Both images have Hα contour lines.
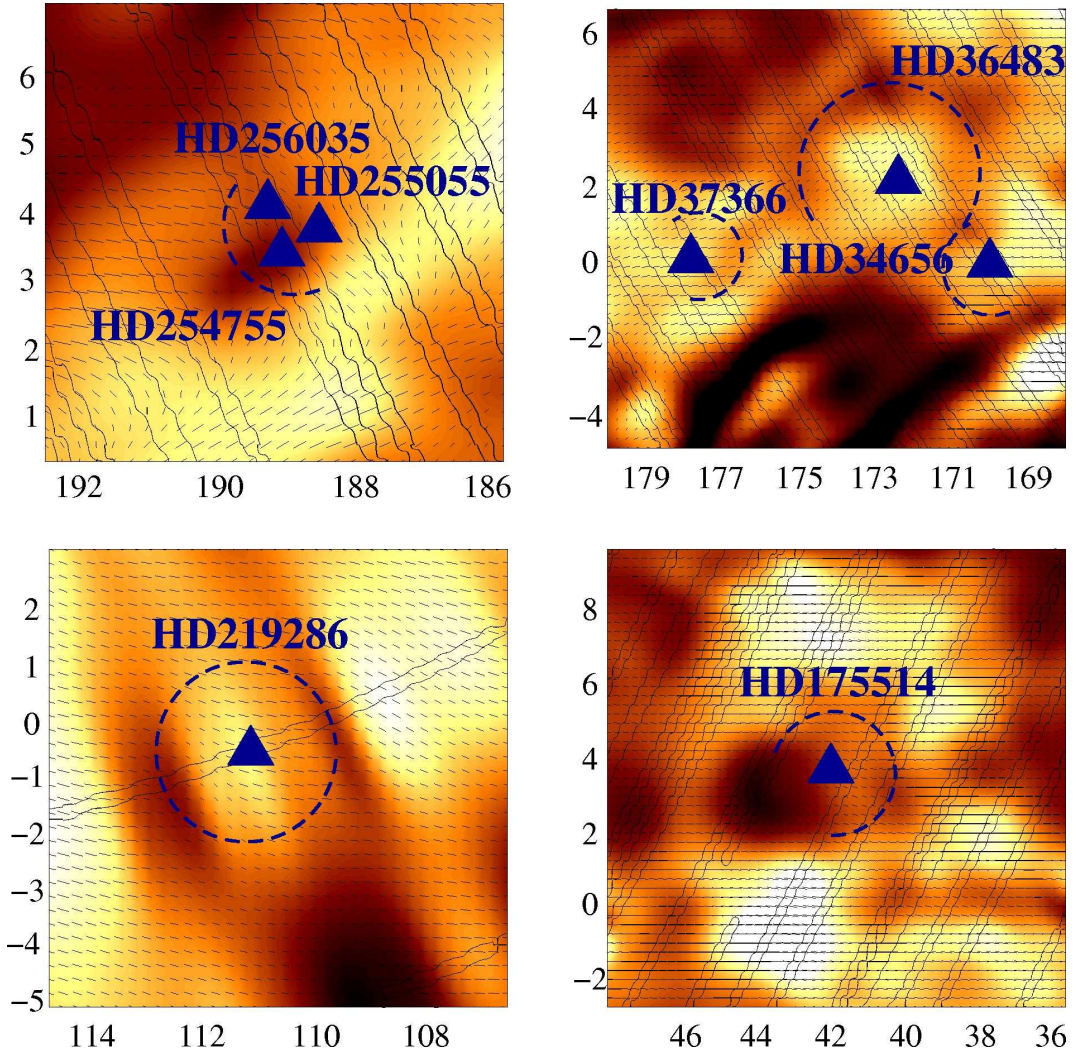
Figure 7.8: O-stars whose Strömgren spheres possibly depolarize background emission. Thin lines indicate drift scans, blue lines the proposed location of depolarization rings. Overlayed are B-vectors of the polarized emission.
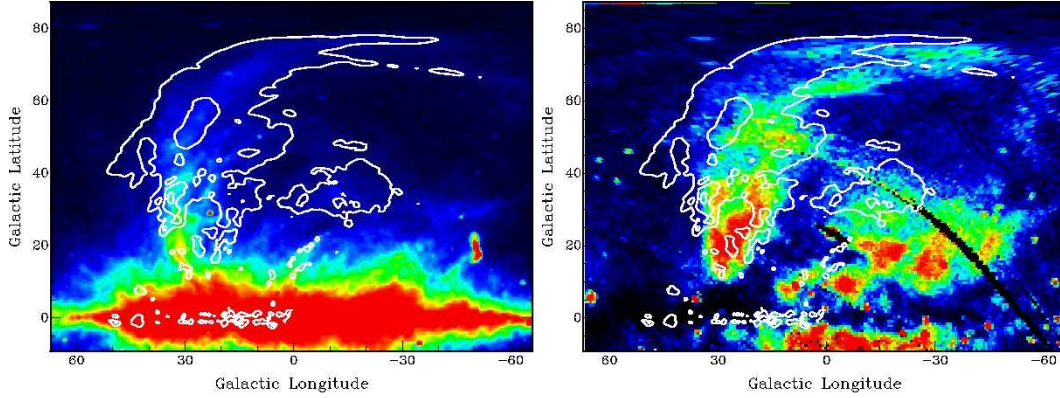
Figure 7.9: Maps of the North-Polar Spur at 408 MHz (left, Haslam et al., 1982) and soft X-ray emission in the 3/4 keV band (right, Snowden et al., 1995). Contours of polarized intensity run from 250 mK in steps of 200 mK. Colours correspond to 10 K (black) and 120 K (red) in the 408 MHz map, and 0 counts/s (black) and $6 \cdot 10^{-4}$ counts/s (red) in the X-ray map.

that the Galaxy possesses a regular magnetic field component parallel to the Galactic plane (e.g. Beck, 2001). A number of effects may cause depolarization. Basically, two different scenarios must be considered:

1. A foreground Faraday screen that depolarizes diffuse background emission. For this to work RM fluctuations must occur on scales smaller than the beam, which then leads to beam depolarization. Burn (1966) described this scenario as external Faraday dispersion in a foreground Faraday screen. He found that

$$\langle DP \rangle = \exp\left(-2\sigma_{RM}^2 \lambda^4\right). \tag{7.3}$$

Assuming a uniformly polarized background and an observed percentage polarization of 3%, which corresponds to DP $\approx$ 0.1 if the percentage polarization of the background is 30%, the dispersion in RM must be $\sigma_{RM} \approx 25$ rad m^{-2} at 1.4 GHz.

2. Internal Faraday dispersion occurs if synchrotron emitting and Faraday rotating regions are mixed. This effect must take place over a large fraction of the sightline in order to reduce the percentage polarization. According to Burn (Equation 7.2), the RM-dispersion over several kpc through the Galaxy must be $\sigma_{RM} \approx 70$ rad m^{-2} to result in DP = 0.1.

Looking at the total intensity maps at other wavelengths a foreground Faraday screen must be considered as a possible explanation. Maps of X-ray emission at 0.75 and 1.5 keV suggest that Loop I and the North-Polar Spur cross the Galactic plane along the longitude interval from approximately 315° to 45° (Figure 7.9 right). In continuum radio maps at 408 MHz (Haslam et al., 1982), 1.4 GHz (Reich, 1982; Reich & Reich, 1986) and 2.8 GHz (W. Reich, priv. comm.), ridges of total power emission clearly associated with the North-Polar Spur can be traced down to latitudes of less than 5° (Figure 7.9 left). At 820 MHz the main ridge of the North-Polar Spur is seen to extent down to $b = 6°$ (Berkhuijsen, 1971). Yet *polarized* emission from that spur is predominately observable at latitudes $|b| \gtrsim 30°$.

The continuum ridge of Loop III can be identified from $b \approx 40°$ down to $b \approx 10°$ at 408 MHz and 1408 MHz, before confusion with total power emission from the Galactic plane sets in. And, again, polarized emission of Loop III is only observable at latitudes above $\sim 20°$ (G87+26). The same holds for the two continuum arcs possibly associated with Loop II and V, which show only polarization at latitudes below $\sim -20°$ (G116-54 and G145+45), although not as clear as for Loop III.

Assuming that the radio loops are intrinsically polarized even at low Galactic latitudes and that their polarization is observable with the 26-m Telescope, strong depolarization must occur between the Sun and Loop I, II, III, and V, in the area of the Depolarization Patch. The distances to these radio loops are commonly assumed between 100 pc (Loop I) and a few hundred parsecs (Loop III and V). Based on the observation that these radio loops are unpolarized within ±20° to ±30° latitude, the existence of a nearby depolarizing Faraday screen seems possible. This Faraday screen must depolarize the Galactic synchrotron emission of the entire first and possibly fourth quadrant in the 26-m Survey.

Such a Faraday screen causes significant depolarization only if the distribution of Faraday rotation induced by the cells is wide enough. A plausible number for the width of the RM distribution is $\sigma_{RM} \approx$ 35 rad m^{-2}, which causes Faraday rotation of about ±90° at 1.4 GHz and hence high depolarization of a uniformly polarized background for a cell number $N > 1$.

Limits on the electron density of the proposed Faraday screen can be derived from the full-sky H-alpha map of Finkbeiner (2003). A comparison of this map with polarized intensity shows that the 2 Rayleigh contour line of Hα emission borders well the Depolarization Patch to Galactic north and south. Taking this as an upper limit for the thermal emissivity of the screen, the lower limit of the electron density calculates to:

$$n_e(\text{screen}) = \sqrt{\frac{\text{EM}}{L}} \approx \sqrt{\frac{1\,\text{Rayleigh}}{L}}, \qquad (7.4)$$

with 1 Rayleigh corresponding to an emission measure of EM = 2 pc cm^{-6}. To produce RMs of 35 rad m^{-2}, a magnetic field of $B_\parallel \approx 40\,\mu$G for a thickness of 1 pc, $B_\parallel \approx 13\,\mu$G for a thickness of 10 pc, or $B_\parallel \approx 9\,\mu$G for a thickness of 20 pc of the screen is required. Then, the electron densities within the screen must be: 1.1 cm^{-3}, 0.3 cm^{-3}, or 0.2 cm^{-3}, respectively.

Against this model speaks the high symmetry of the Depolarization Patch about the Galactic plane, which may indicate a relation to the Galactic electron distribution rather than a local origin. The depolarization would then be caused by depth depolarization with the sharp boundaries reflecting the *z*-distribution of the magneto-ionic medium causing depolarization. In this scenario, the observed synchrotron emission of the loops must be depolarized by other effects than a foreground Faraday screen.

Alternative explanations for the obvious lack of polarized emission from Loop I, III, and possibly II and IV can be summarized as follows: 1) Depolarization within the loops reduces the *intrinsic* degree of polarization. This may be caused by a turbulent magnetic field inside the loop raising beam and depth depolarization, or a radial magnetic field component of the loop causing only depth depolarization. 2) Superposition of polarized emission from the loops with polarized background emission may reduce the observed degree of polarization. These are discussed in the following.

If depolarization within the loops is caused by a turbulent magnetic field inside the shell, this turbulence must be a function of *z* to explain the latitude boundaries of the Depolarization Patch. Any regular magnetic field causing depolarization must have a component parallel to the line-of-sight to result in Faraday rotation. A possible radial B-field of the loops may result in the latitude boundaries observed, because the viewing angle of this radial field would depend on Galactic latitude.

Superposition with polarized background emission would lead to depolarization of loop emission if the intensities of both were about equal and the polarization angles differ by $\sim 90°$. This, however, would only lead to depolarization towards synchrotron emission from the loops, resulting in a "negative imprint" in an otherwise highly polarized background. This seems not compatible with the observation of a coherent patch of depolarization.
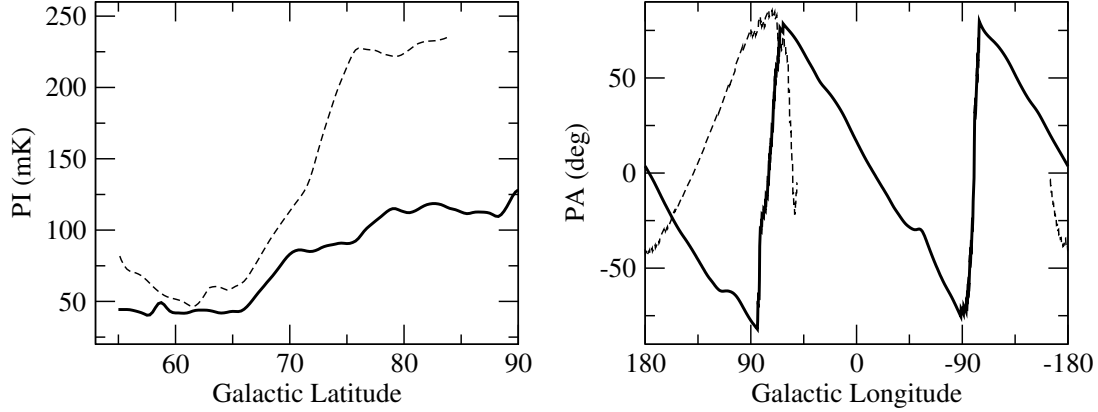
Figure 7.10: The left panel shows the observed increase of polarized intensity toward the northern (thick line) and southern (dashed line) Galactic poles. To avoid confusion the North-Polar Spur was excluded in this plot. The right panel shows the polarization angle (E-vectors) along two Galactic longitude cuts for $b \geq 80°$ (thick line) and $b \leq -80°$ (dashed line).

7.3.3 High-Latitude Polarized Emission

The HLPE is visible in the new 26-m Survey as a gradual and significant increase of polarized intensity and percentage polarization toward high Galactic latitudes, while the polarization angle systematically changes with Galactic longitude. This gradient in polarized intensity at $|b| \approx 70°$ as well as a linear dependence of the polarization angle on Galactic longitude at $|b| \geq 80°$ is displayed in Figure 7.10.

Synchrotron emission of the HLPE is also detectable in total power. At 408 MHz (Haslam et al., 1982) excess emission at high Galactic latitudes of ~ 4 K (northern pole) and ~ 5 K (southern pole) is visible, similar in shape to the emission observed in the 26-m Survey. In the total intensity map at 1.4 GHz (Reich, 1982; Reich & Reich, 1986) a faint excess of ~ 60 mK towards the northern pole, and ~ 200 mK towards the southern pole is noticeable. This results in a temperature spectral index of $\beta \approx -3.4$ and $\beta \approx -2.6$, for the northern and southern HLPE, respectively.

It is noted that the HLPE may be associated with neutral hydrogen that is found in the Galactic pole regions at $|b| > 80°$ by Dieter (1964). This author found evidence for two components of gas velocities at the north Galactic pole, one at velocities around zero, and the other with velocities between -20 and -55 km/s. At the southern pole velocities of mainly -10 km/s can be seen. In addition, the presence of faint dust filaments associated with the HLPE component is noted here.

A simple model of a shell-like magnetic field is developed and provides a possible explanation for the enhanced polarized and total intensity emission at high Galactic latitudes. In this model the magnetic shell is of spherical shape. Inside the shell the magnetic field orientation is longitudinal and of equal strength (see Figure 7.11). For an observer inside the shell the intensity of the received synchrotron emission depends on the strength of the magnetic field component perpendicular to the line-of-sight and is thus proportional to $B_\perp^{(\gamma+1)/2}$. An energy spectral index of $\gamma \approx 2.6$ for the relativistic electrons is assumed. No Faraday rotation is considered in this model.

Certainly, the magnetic field configuration used for this simple model is not physical. However, the deviation from a realistic magnetic field geometry is small, which justifies this approach. In nature, such magnetic shells exist around evolved SNRs with field lines tangential to the shock front. Superbubbles are also believed to possess magnetic fields comparable to the one used in the model.

A reasonable fit is achieved if the centre of this magnetic shell is placed at a distance of 150 pc toward $l = 350°$ and $b = 0°$, with a shell-thickness of 30 pc. The Sun is located within the shell between the
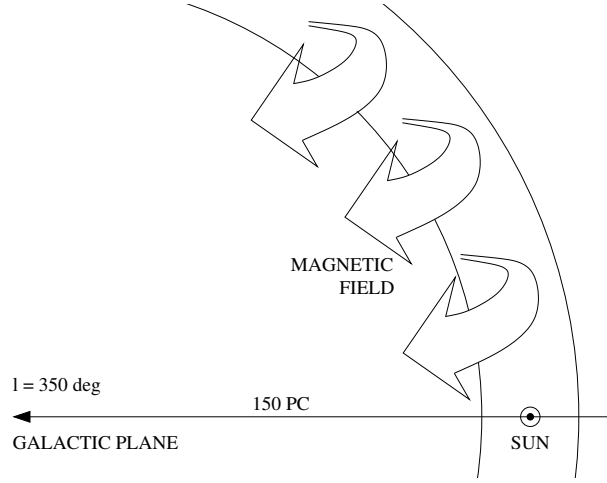
Figure 7.11: Illustration showing the configuration of the shell and the magnetic field associated with it. The centre of the shell is 150 pc away, towards $l = 350°$, $b = 0°$. The thickness of the shell is 30 pc. Magnetic field lines run along longitudes of the shell.

outer and inner edge. These parameters are found by rough fitting and the numbers quoted are therefore rather uncertain. Figure 7.12 shows the predicted polarized and total intensity emission for such a shell. They compare well with the observed gradient and distribution of polarized intensity and polarization angle as displayed in Figure 7.10.

Assuming that the HLPE is due to a compression of the interstellar magnetic field, the compression factor can be estimated. This is done by comparing the observed polarized intensities of two different sightlines. These sightlines run different ways through the shell: the first with a short lengths ($l = 175°$, $b = 60°$), and the second running northwards (southwards) through the shell ($b \approx |90°|$). The observed average polarized intensities are $PI_{short} = 15$ mK ($50° \leq b \leq 70°$, $170° \leq l \leq 180°$) and $PI_{long} = 102$ mK ($75° \leq b \leq 90°$ and $170° \leq l \leq 180°$). The ratio of both indicates a compression factor of 2.9 of the magnetic field inside the shell. The same estimate at the southern Galactic pole gives a factor of 2.4.

7.4 Results and Discussion

An investigation of H II-regions gives distances to the origin of polarized emission of the fan-region. In contrast to studies made by other authors, which suggested a rather local origin of the fan-region, is it found here that the emission of the fan-region originates at least partly in the Perseus arm.

Following these arguments, it is proposed that the fan-region is the result of a relatively long line-of-sight exhibiting less depolarization than in any other direction. If the high degree of polarization towards the fan-region is the consequence of a Galactic magnetic field oriented perpendicular to the line-of-sight, the distance to which this geometry holds must be much larger then previously assumed. This may also indicate that turbulence in the outer Galaxy is not as significant as in the inner Galaxy.

The fan-region extends to Galactic latitudes of $\sim \pm 20°$. At a distance of 2 kpc this corresponds to a height of 0.7 kpc above the plane. Its brightness temperature in total intensity is around 1 K at these latitudes. According to the model of Beuermann et al. (1985), 57% of the synchrotron emission toward $l = 140°$ and $b = \pm 20°$ is generated at distances < 2 kpc, whereas 43% originates at larger distances. In
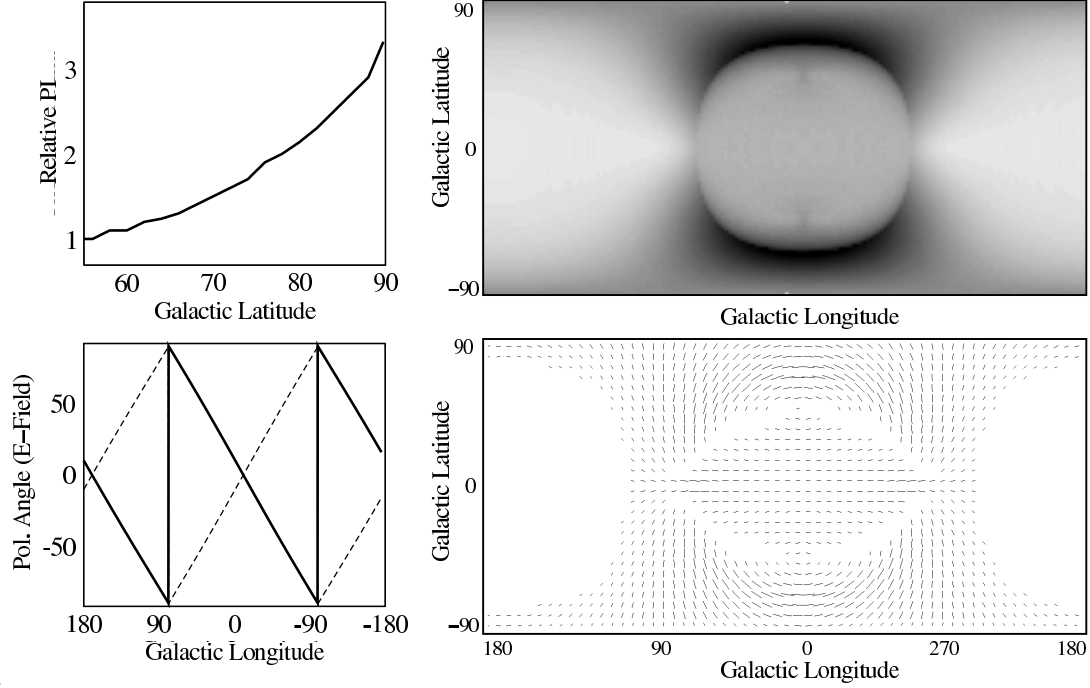
Figure 7.12: Top left: Modelled polarized intensity for a latitude cut at $l = 180°$. Top right: Total intensity synchrotron emission expected from the shell if the magnetic field is uniformly illuminated with cosmic-ray electrons (black: high intensity, white: low intensity). Bottom left: The modelled polarization angles for longitude cuts at $b = 85°$ (thick line) and $b = -85°$ (dashed line). Bottom right: The projected magnetic field of the shell in a rectangular grid of Galactic coordinates.

the outer region of the Galaxy only the thick disk[2] contributes to the observed synchrotron emission.

The obvious lack of polarization towards the first Galactic quadrant is interpreted as due to depolarization. Missing polarized emission from the radio loops suggests that the depolarization is caused by a nearby Faraday screen. DP of ~ 0.1 are required to explain the percentage polarization observed towards the Depolarization Patch. This results in a magnetic field strength between 40 μG and 9 μG and an electron density between 1.1 cm^{-3} and 0.2 cm^{-3} for a thickness of the Faraday screen between 1 pc and 20 pc. The high degree of symmetry about the Galactic plane, however, seems to indicate that the Depolarization Patch is caused by depth depolarization. The northern and southern boundaries may reflect the decrease of depolarization with z-height above the plane. The missing emission from the loops at latitudes below $b \lesssim 30°$ must than be explained by depolarizing effects within the loops.

It should be noted that a more speculative theory predicts the North-Polar Spur to be part of a bipolar hypershell originating from starburst activity in the Galactic centre (Sofue, 2000). Kuntz & Snowden (2001), however, note that there is significant emission in the direction of Loop I in front of the Ophiuchus dark clouds at ~ 150 pc, which is not seen in the foreground in other directions, indicating a local origin for Loop I.

This analysis of the Depolarization Patch is solely based on northern sky data not fully covering the

---

[2]Models of Galactic synchrotron emission are derived by assuming that emission originates from three different components of the Galaxy: a thick disk, a thin disk, and a structure of spiral arms (e.g. Beuermann et al., 1985).

fourth Galactic quadrant. An all-sky polarization map[3] will soon become available. This will allow the investigation of the properties of the Depolarization Patch more accurately and help understand its origin.

The polarized emission observed at high Galactic latitudes, the HLPE, can be modelled by assuming that the Sun is located within a magnetized shell. In this model the intensity and polarization angle of the observed synchrotron emission are given by the strength and direction of the magnetic field component perpendicular to the line-of-sight. A compression factor of the field inside the shell of ~ 3 relative to an ambient magnetic field can be derived. The centre and spatial extent of this shell correspond well to that of Loop I.

The agreement in centre and size of the HLPE with Loop I suggest a common origin. It is therefore proposed that the HLPE is a magnetic shell associated with Loop I: either a magnetic field around the H I bubble or the compressed field around an evolved SNR. This is supported by the previously mentioned association of H I and dust filaments with the HLPE.

These investigations can only provide the basis for deeper analysis. Improvement in sky coverage is required to strengthen arguments for the distance of the fan-region, given by the depolarization of H II-regions. A multi-wavelength analysis of the Depolarization Patch must follow, taking X-ray and dust emission into account. Finally, better sampled data may show correlations between the HLPE and filaments in dust and H I more clearly.

---

[3]achieved by combining the 26-m Survey and the Villa-Elisa Survey (Testori et al., 2004)

8 Summary and Conclusion

My research objective was to realize a polarization survey covering the northern sky, which would allow the absolute calibration of recent high-resolution polarization observations. During an observing time of 7 months, I was able to perform 168 fully calibrated drift scans, utilizing the 26-m Telescope of the DRAO. The resulting sky coverage and sensitivity exceeds that of the so far available data of the northern sky, observed in the 1960's and 70's with the Dwingeloo telescope. By comparing drift scans with data obtained with the Effelsberg 100-m telescope an accurate brightness temperature scale of the new survey could be established.

In areas where the sampling of the LDS is too sparse, the new 26-m Survey makes proper calibration of high-resolution data possible. I showed that a correct representation of large-scale emission in Stokes U and Q down to the lowest spatial frequencies is mandatory for the analysis of diffuse polarized emission, and that the 26-m Survey provides these data to correct for missing emission components in high-resolution data.

Aside from making absolutely calibrated data available for calibration purposes, the 26-m Survey is a valuable astronomical product in its own right, revealing unknown features and providing valuable information on the Galactic polarized foreground. By an initial analysis of the new data I was able to reach the following conclusions: 1) Depolarizing H ɪɪ-regions towards the highly polarized fan-region reveal a larger distance to the origin of polarized emission than previously believed. As a consequence turbulence of the magneto-ionic medium in the outer Galaxy towards the fan-region must be small to allow the relatively long line-of-sight in polarization; 2) An apparent lack of polarized emission towards the first Galactic quadrant is noted and is interpreted as due to depolarization. Based on the non-observation of polarized emission from the radio loops, the possibility of a local Faraday screen causing depolarization is discussed. Other arguments taking into account effects within the loops are considered; 3) Polarized emission at high Galactic latitudes is found and modelled assuming that the Sun is located within a magnetic shell that emits synchrotron emission.

8.1 Major Contributions

In summary, my research involved the further development of the receiving system of the DRAO 26-m telescope to make measurements of linear polarization possible. Moreover, applicable data processing routines needed to be developed to properly calibrate the raw data. This required the solution of problems such as the system temperature variations recognized during data reduction, and the development of a suitable interpolation routine. The major contributions of my exploration of the Galactic polarized emission are as follows:

- Realization and calibration of the Low-Resolution DRAO Survey of Polarized Emission at 1.4 GHz.

- Demonstration of the necessity of absolute calibrating diffuse polarized emission and the capability of the 26-m Survey in providing the spatial frequencies required for this calibration.

- Evidence that a significant amount of polarized emission from the fan-region originates in or beyond the Perseus spiral arm. Hence, the intense polarized emission is received from much larger

distances than in any other direction. This can be used to derive constraints on the properties of the magneto-ionic medium of the outer Galaxy.

- First description of a lack of polarized emission revealed by low percentage polarization towards the first Galactic quadrant.

- First observational evidence for polarized radio emission at 1.4 GHz at high Galactic latitudes.

8.2 Future Work

Observations for the 26-m Survey I have presented here are continuing. Currently (by March 2005), the coverage of the northern sky with drift scans has reached 43%. These data must be incorporated and will result in a considerable improvement of the 26-m Survey in terms of resolution, sensitivity, and error. It is planned to make the extended data public.

The incorporation of the latest data of the 26-m Survey will allow to substantiate arguments for the revised distance to the fan-region as described in this thesis. A larger number of well justified H ɪɪ-regions acting as depolarizing Faraday screens will provide data for the study of the local synchrotron emissivity.

The inclusion of data from the southern sky polarization survey (Testori et al., 2004) is required to confine boundaries of the Depolarization Patch more accurately. An improvement in sampling could also allow to investigate small-scale fluctuations towards the first quadrant, which could reveal its origin.

Another point concerns the observing scheme. Here, it is desirable to apply an independent calibration instead of relying on the LDS. This becomes even more important in view of the planned upgrade of the 26-m telescope to allow the simultaneous measurement of polarization at multiple frequencies. Also, an improved model for ground radiation should be developed, possibly taking time-variability into account.

Müller Matrix Elements

List of Müller matrix elements (from Theocaris & Gdoutos, 1979):

$$
\begin{aligned}
2m_{II} &= j_{11}^{\star}j_{11} + j_{21}^{\star}j_{21} + j_{12}^{\star}j_{12} + j_{22}^{\star}j_{22} \\
2m_{IQ} &= j_{11}^{\star}j_{11} + j_{21}^{\star}j_{21} - j_{12}^{\star}j_{12} - j_{22}^{\star}j_{22} \\
2m_{IU} &= j_{11}^{\star}j_{12} + j_{21}^{\star}j_{22} + j_{12}^{\star}j_{11} + j_{22}^{\star}j_{21} \\
2m_{IV} &= i\left(j_{11}^{\star}j_{12} + j_{21}^{\star}j_{22} - j_{12}^{\star}j_{11} - j_{22}^{\star}j_{21} \right) \\
2m_{QI} &= j_{11}^{\star}j_{11} + j_{12}^{\star}j_{12} - j_{21}^{\star}j_{21} - j_{22}^{\star}j_{22} \\
2m_{QQ} &= j_{11}^{\star}j_{11} + j_{22}^{\star}j_{22} - j_{21}^{\star}j_{21} - j_{12}^{\star}j_{12} \\
2m_{QU} &= j_{12}^{\star}j_{11} + j_{11}^{\star}j_{12} - j_{22}^{\star}j_{21} - j_{21}^{\star}j_{22} \\
2m_{QV} &= i\left(j_{11}^{\star}j_{12} + j_{22}^{\star}j_{21} - j_{21}^{\star}j_{22} - j_{12}^{\star}j_{11} \right) \\
2m_{UI} &= j_{11}^{\star}j_{21} + j_{21}^{\star}j_{11} + j_{12}^{\star}j_{22} + j_{22}^{\star}j_{12} \\
2m_{UQ} &= j_{11}^{\star}j_{21} + j_{21}^{\star}j_{11} - j_{12}^{\star}j_{22} - j_{22}^{\star}j_{12} \\
2m_{UU} &= j_{11}^{\star}j_{22} + j_{21}^{\star}j_{12} + j_{12}^{\star}j_{21} + j_{22}^{\star}j_{11} \\
2m_{UV} &= i\left(j_{11}^{\star}j_{22} + j_{21}^{\star}j_{12} - j_{12}^{\star}j_{21} - j_{22}^{\star}j_{11} \right) \\
2m_{VI} &= i\left(j_{21}^{\star}j_{11} + j_{22}^{\star}j_{12} - j_{11}^{\star}j_{21} - j_{12}^{\star}j_{22} \right) \\
2m_{VQ} &= i\left(j_{21}^{\star}j_{11} + j_{12}^{\star}j_{22} - j_{11}^{\star}j_{21} - j_{22}^{\star}j_{12} \right) \\
2m_{VU} &= i\left(j_{21}^{\star}j_{12} + j_{22}^{\star}j_{11} - j_{11}^{\star}j_{22} - j_{12}^{\star}j_{21} \right) \\
2m_{VV} &= j_{22}^{\star}j_{11} + j_{11}^{\star}j_{22} - j_{12}^{\star}j_{21} - j_{21}^{\star}j_{12}
\end{aligned}
\tag{.1}
$$

Bibliography

Altenhoff, W., Mezger, P. G., Strassl, H., Wendker, H., & Westerhout, G. 1960, Veröffentlichunnge der Universitäts-Sternwarte zu Bonn, 59

Beck, R. 2001, Space Science Reviews, 99, 243

Berkhuijsen, E. M. 1971, Astronomy and Astrophysics, 14, 359

—. 1975, Astronomy and Astrophysics, 40, 311

Berkhuijsen, E. M. & Brouw, W. N. 1963, Bull. Astron. Inst. Netherlands, 17, 185

Berkhuijsen, E. M., Brouw, W. N., Muller, C. A., & Tinbergen, J. 1964, Bull. Astron. Inst. Netherlands, 17, 465

Berkhuijsen, E. M., Haslam, C. G. T., & Salter, C. J. 1971, Astronomy and Astrophysics, 14, 252

Bernardi, G., Carretti, E., Fabbri, R., Sbarra, C., Poppi, S., & Cortiglioni, S. 2004, in The Magnetized Interstellar Medium, 207–212

Bertiau, F. C. 1958, Astrophysical Journal, 128, 533

Beuermann, K., Kanbach, G., & Berkhuijsen, E. M. 1985, Astronomy and Astrophysics, 153, 17

Bingham, R. G. 1966, Monthly Notices of the RAS, 134, 327

Bingham, R. G. & Shakeshaft, J. R. 1967, Monthly Notices of the RAS, 136, 347

Bochkarev, N. G. 1987, Astrophysics and Space Science, 138, 229

Born, M. & Wolf, E. 1965, Principles of optics. Electromagnetic theory of propagation, interference and diffraction of light (Oxford: Pergamon Press, |c1965, 3rd (revised) ed.)

Brouw, W. N., Muller, C. A., & Tinbergen, J. 1962, Bull. Astron. Inst. Netherlands, 16, 213

Brouw, W. N. & Spoelstra, T. A. T. 1976, Astronomy and Astrophysics, Supplement, 26, 129

Burn, B. J. 1966, Monthly Notices of the RAS, 133, 67

Campbell, R. M. 1999, New Astronomy Review, 43, 617

Conway, R. G. & Kronberg, P. P. 1969, Monthly Notices of the RAS, 142, 11

Cox, D. P. & Reynolds, R. J. 1987, Annual Review of Astron and Astrophys, 25, 303

Cruz-Gonzalez, C., Recillas-Cruz, E., Costero, R., Peimbert, M., & Torres-Peimbeert, S. 1974, Revista Mexicana de Astronomia y Astrofisica, 1, 211

de Geus, E. J. & Burton, W. B. 1991, Astronomy and Astrophysics, 246, 559

Dickey, J. M. 1997, Astrophysical Journal, 488, 258

Dickey, J. M., McClure-Griffiths, N., Gaensler, B., Green, A., Haynes, R., & Wieringa, M. 1999, in Astronomical Society of the Pacific Conference Series, 27–+

Dieter, N. H. 1964, Astronomical Journal, 69, 137

Duncan, A. R., Haynes, R. F., Jones, K. L., & Stewart, R. T. 1997, Monthly Notices of the RAS, 291, 279

Duncan, A. R., Haynes, R. F., Reich, W., Reich, P., & Gray, A. D. 1998, Monthly Notices of the RAS, 299, 942

Egger, R. J. & Aschenbach, B. 1995, Astronomy and Astrophysics, 294, L25

Egger, R. J., Freyberg, M. J., & Morfill, G. E. 1996, Space Science Reviews, 75, 511

Erickson, W. C., Perley, R. A., Flatters, C., & Kassim, N. E. 2001, Astronomy and Astrophysics, 366, 1071

Ferlet, R. 1999, Astronomy and Astrophysics Reviews, 9, 153

Fich, M. & Blitz, L. 1984, Astrophysical Journal, 279, 125

Fich, M., Blitz, L., & Stark, A. A. 1989, Astrophysical Journal, 342, 272

Finkbeiner, D. P. 2003, Astrophysical Journal, Supplement, 146, 407

Freyberg, M. J. & Breitschwerdt, D. 2001, in Astronomische Gesellschaft Meeting Abstracts, 104–+

Gaensler, B. M., Dickey, J. M., McClure-Griffiths, N. M., Green, A. J., Wieringa, M. H., & Haynes, R. F. 2001, Astrophysical Journal, 549, 959

Gray, A. D., Landecker, T. L., Dewdney, P. E., & Taylor, A. R. 1998, Nature, 393, 660

Gray, A. D., Landecker, T. L., Dewdney, P. E., Taylor, A. R., Willis, A. G., & Normandeau, M. 1999, Astrophysical Journal, 514, 221

Haslam, C. G. T., Large, M. I., & Quigley, M. J. S. 1964, Monthly Notices of the RAS, 127, 273

Haslam, C. G. T., Stoffel, H., Salter, C. J., & Wilson, W. E. 1982, Astronomy and Astrophysics, Supplement, 47, 1

Haverkorn, M., Gaensler, B. M., McClure-Griffiths, N. M., Dickey, J. M., & Green, A. J. 2004a, Astrophysical Journal, 609, 776

Haverkorn, M., Katgert, P., & de Bruyn, A. G. 2004b, Astronomy and Astrophysics, 427, 549

Heiles, C. 1967, Astrophysical Journal, Supplement, 15, 97

Heiles, C. 2002, in Astronomical Society of the Pacific Conference Series, 131–152

Heiles, C., Perillat, P., Nolan, M., Lorimer, D., Bhat, R., Ghosh, T., Howell, E., Lewis, M., O'Neil, K., Salter, C., & Stanimirovic, S. 2001, PASP, 113, 1247

Higgs, L. A. 1967, Bulletin of the Astronomical Institute of the Netherlands Supplement Series, 2, 59

Higgs, L. A. & Tapping, K. F. 2000, Astronomical Journal, 120, 2471

Howell, T. F. & Shakeshaft, J. R. 1966, Nature, 210, 1318

Jansky, K. G. 1933, Proc. I.R.E., 21, 1387

Jones, R. C. 1941, Journal of the Optical Society of America (1917-1983), 31, 488

Junkes, N. 1986, Mitteilungen der Astronomischen Gesellschaft Hamburg, 65, 224

Kafatos, M. C. & Morrison, P. 1973, Astronomy and Astrophysics, 26, 71

Kiepenheuer, K. O. 1950, Physical Review, 79, 738

Knee, L. B. G. 1997, DRAO Internal Report

Kothes, R., Landecker, T. L., & Wolleben, M. 2004a, Astrophysical Journal, 607, 855

Kothes, R., Landecker, T. L., Wolleben, M., Foster, T., & Reich, W. 2004b, DRAO News

Kraus, J. D. 1966, Radio astronomy (New York: McGraw-Hill, 1966)

Kuntz, K. D. & Snowden, S. L. 2001, Astrophysical Journal, 554, 684

Landecker, T. L., Uyaniker, B., & Kothes, R. 2002, in AIP Conf. Proc. 609: Astrophysical Polarized Backgrounds, 9–12

Large, M. I., Quigley, M. F. S., & Haslam, C. G. T. 1966, Monthly Notices of the RAS, 131, 335

Large, M. I., Quigley, M. J. S., & Haslam, C. G. T. 1962, Monthly Notices of the RAS, 124, 405

Mathewson, D. S., Broten, N. W., & Cole, D. J. 1965, Australian Journal of Physics, 18, 665

—. 1966, Australian Journal of Physics, 19, 93

McMullin, J. P., Golap, K., & Myers, S. T. 2004, in Astronomical Society of the Pacific Conference Series, 468–+

Milogradov-Turin, J. & Urosevic, D. 1997, Bulletin Astronomique de Belgrade, 155, 41

Mueller, H. 1948, J. Opt. Soc. Am., 38, 661

Muller, C. A., Berkhuijsen, E. M., Brouw, W. N., & Tinbergen, J. 1963, Nature, 200, 155

Pacholczyk, A. G. 1970, Radio astrophysics. Nonthermal processes in galactic and extragalactic sources (Series of Books in Astronomy and Astrophysics, San Francisco: Freeman, 1970)

Quigley, M. J. S. & Haslam, C. G. T. 1965, Nature, 208, 741

Razin, V. A., Khrulev, V. V., Fedorov, V. T., Volokhov, S. A., Melnikov, A. A., Paseka, A. M., & Pupysheva, L. V. 1968, Izvestiya VUZ. Radiofizika, 11, 1461

Reber, G. 1944, Astrophysical Journal, 100, 279

Reich, P. & Reich, W. 1986, Astronomy and Astrophysics, Supplement, 63, 205

Reich, W. 1982, Astronomy and Astrophysics, Supplement, 48, 219

Reich, W., Fürst, E., Reich, P., Uyaniker, B., Wielebinski, R., & Wolleben, R. 2004, in The Magnetized Interstellar Medium, 45–50

Reich, W., Reich, P., & Fuerst, E. 1990, Astronomy and Astrophysics, Supplement, 83, 539

Reich, W. & Wielebinski, R. 2000, Radio Polarization: a New Probe of the Galaxy, Proceedings of a Workshop held at Université de Mentréal

Rohlfs, K. & Wilson, T. L. 1996, Tools of Radio Astronomy (Tools of Radio Astronomy, XVI, 423 pp. 127 figs., 20 tabs.. Springer-Verlag Berlin Heidelberg New York. Also Astronomy and Astrophysics Library)

Rubin, V. C., Burtley, J., Kiasatpoor, A., Klock, B., Pease, G., Rutscheidt, E., & Smith, C. 1962, Astronomical Journal, 67, 491

Salter, C. J. 1983, Bulletin of the Astronomical Society of India, 11, 1

Schott, G. A. 1907, Ann. Physik

Siringo, G., Kreysa, E., Reichertz, L. A., & Menten, K. M. 2004, Astronomy and Astrophysics, 422, 751

Snowden, S. L., Freyberg, M. J., Plucinsky, P. P., Schmitt, J. H. M. M., Truemper, J., Voges, W., Edgar, R. J., McCammon, D., & Sanders, W. T. 1995, Astrophysical Journal, 454, 643

Sofue, Y. 2000, Astrophysical Journal, 540, 224

Spoelstra, T. A. T. 1971, Astronomy and Astrophysics, 13, 237

—. 1984, Astronomy and Astrophysics, 135, 238

Tauber, J. A. 2004, in The Magnetized Interstellar Medium, 191–199

Taylor, A. R., Gibson, S. J., Peracaula, M., Martin, P. G., Landecker, T. L., Brunt, C. M., Dewdney, P. E., Dougherty, S. M., Gray, A. D., Higgs, L. A., Kerton, C. R., Knee, L. B. G., Kothes, R., Purton, C. R., Uyaniker, B., Wallace, B. J., Willis, A. G., & Durand, D. 2003, Astronomical Journal, 125, 3145

Testori, J. C., Reich, P., & Reich, W. 2004, in The Magnetized Interstellar Medium, 57–62

Theocaris, P. S. & Gdoutos, E. E., eds. 1979, Matrix theory of photoelasticity

Tinbergen, J. 1996, Astronomical polarimetry (Cambridge, New York: Cambridge University Press, |c1996, ISBN 0521475317)

Uyaniker, B., Fürst, E., Reich, W., Reich, P., & Wielebinski, R. 1999, Astronomy and Astrophysics, Supplement, 138, 31

Uyaniker, B., Fuerst, E., Reich, W., Reich, P., & Wielebinski, R. 1998, Astronomy and Astrophysics, Supplement, 132, 401

Verschuur, G. L. 1968, The Observatory, 88, 15

von Hoensbroech, A. & Xilouris, K. M. 1997, Astronomy and Astrophysics, Supplement, 126, 121

Weaver, H. 1979, in IAU Symp. 84: The Large-Scale Characteristics of the Galaxy, 295–298

Westerhout, G., Seeger, C. L., Brouw, W. N., & Tinbergen, J. 1962, Bull. Astron. Inst. Netherlands, 16, 187

Westfold, K. C. 1959, Astrophysical Journal, 130, 241

Wielebinski, R. & Shakeshaft, F. R. 1964, Monthly Notices of the RAS, 128, 19

Wielebinski, R., Shakeshaft, J. R., & Pauliny-Toth, I. I. K. 1962, The Observatory, 82, 158

Wieringa, M. H., de Bruyn, A. G., Jansen, D., Brouw, W. N., & Katgert, P. 1993, Astronomy and Astrophysics, 268, 215

Wilkinson, A. & Smith, F. G. 1974, Monthly Notices of the RAS, 167, 593

Willingale, R., Hands, A. D. P., Warwick, R. S., Snowden, S. L., & Burrows, D. N. 2003, Monthly Notices of the RAS, 343, 995

Wolleben, M. 2001, Diplomarbeit, Universität Bonn

Wolleben, M. & Reich, W. 2004, Astronomy and Astrophysics, 427, 537

List of Tables

List of Figures

116